ADVANCED RADIOSENSITIZING NANOPLATFORMS FOR ENHANCED RADIATION THERAPY

by

FANGCHAO JIANG

(Under the Direction of Jin Xie)

ABSTRACT

As one of the major challenges worldwide, cancer has been a detrimental health issue for the mainstream public incurring disfunction of surrounding organs or death. Because of the severity of the disease, numerous therapeutic approaches have been proposed this century. And as a part of the treatment, radiation therapy is deemed one of the most powerful and commonly accessible tools. It is non-invasive and can be utilized for almost all types of malignant cancer cell lines and is also reported for treating benign cancers or other diseases such as Kimura and Keloid scars. However, current nanoplatforms for radiation therapy still default the need for tumor eradication, and there are potentially remaining drawbacks that adversely hinder the progress of radiation therapy. One major limitation of conventional radiation therapy is the total dose of radiation that must be taken to fulfill the therapeutic efficacies, and it is always intolerable for most patients receiving high doses of radiation. To overcome this, we tactfully designed and assembled several nanoplatforms that can be applied as radiosensitizing reagents. We evidenced that with the help of those nanoplatforms, we can significantly reduce the dosage for radiation while approaching similar therapeutic efficacies *in vitro* and *in vivo,* causing minimal cytotoxicity toward surrounding normal tissues and organs.

INDEX WORDS: radiation therapy, X-ray induced photodynamic therapy, photosensitizer, scintillating nanoparticles

ADVANCED RADIOSENSITIZING NANOPLATFORMS FOR ENHANCED RADIATION THERAPY

by

FANGCHAO JIANG
BS, Wuhan University, China, 2015
MS, Columbia University, 2016

A Dissertation Submitted to the Graduate Faculty of The University of Georgia in Partial Fulfillment of the Requirements for the Degree

DOCTOR OF PHILOSOPHY

ATHENS, GEORGIA

2022

ADVANCED RADIOSENSITIZING NANOPLATFORMS FOR ENHANCED RADIATION THERAPY

by

FANGCHAO JIANG

Major Professor:	Jin Xie
Committee:	Tina Salguero
	Sergiy Minko

Electronic Version Approved:

Ron Walcott
Vice Provost for Graduate Education and Dean of the Graduate School
The University of Georgia
December 2022

ACKNOWLEDGEMENTS

Being a graduate student at the University of Georgia under Dr. Jin Xie’s supervision is one of my most rewarding and memorable experiences. But not for this opportunity, I won’t be able to meet so many fantastic colleagues, friends, and experts and realize that my life is not merely a miniature of others but could be an impressive epic. I am not a nobody shackled by the rules of the established realm but somebody possessing the potential of breaking impossibility. Those people motivated me and made me realize that there are always new heights that I can achieve, and there are always novel ideas I should endeavor.

The most valuable experience I learned during this period is continually being cautious and fully prepared. That is not always easy, and I discovered that from endless failures. I still remember the first time I was preparing for my literature seminar. When my advisor asked me to give a rehearsal one week before the presentation, I optimistically thought I was fully prepared. However, it turned out to be an aftermath. Fortunately, I was able to remedy that within one week under my advisor and colleagues' guidance. And it was the first time I realized the importance of being fully prepared. Another rewarding merit I learned is always keeping critical thinking. And that is beneficial not only for my academic skills but my daily life as well.

The first and the foremost person I would love to thank you is my advisor, Dr. Jin Xie. Without his talented guides and incredible foresight, I won’t be able to achieve so many tremendous movements and stand here officially as a completed doctoral graduate.

I would also acknowledge the help from Wendy and Bryan. Since I was a student majoring in materials chemistry, I barely had any background concerning cancer cell lines and mice studies. It was them who systematically taught me, facilitated my work, and helped me out.

I also would love to thank you for the help from all my other lab mates, including Benjamin Cline, Anil Kumar, Shiyi Zhou, Zhengwei Cao, Ian Delahunty, Wei Yang, Chaebin Lee, Xueyuan Yang, Shuyue Zhan, Jianwen Li, and Zhi Liu. Without them, I won’t be able to complete my work and dissertation.

I would love to thank you for the help from Eric Formo from the UGA electron microscope center, Julie Nelson from the UGA cytometry lab, and Daphne Norton from general chemistry lab. Their intelligence and deep thoughts significantly promoted the progress of my research.

In addition, I would love to thank you for the help from Dr. Zibo Li, Dr. Tina Salguero, and Dr. Sergiy Minko. Their broad knowledge, extensive experience, and sharp insight into nanomedicine and materials science inspired me all the time.

I am also grateful for all those friends and experts from the University of Georgia, Georgia Tech, and Columbia University, who were always around when I needed help in my life.

Special acknowledgment goes to Xing Li, who supported me and encouraged me to pursue better scientific works. And finally, my parents and all family members who fostered and helped me pursue a better life.

TABLE OF CONTENTS

Page

CHAPTER

APPENDICES

LIST OF TABLES

LIST OF FIGURES

CHAPTER 1

INTRODUCTION AND LITERATURE REVIEW: RADIATION THERAPY AND X-RAY INDUCED PHOTODYNAMIC THERAPY

1.1 Introduction to radiation therapy

Photodynamic therapy (PDT) is an emerging anti-cancer therapeutic modality. PDT involves three essential components, which are photosensitizer, oxygen, and light, often in the form of a laser or light-emitting diode (LED). Many photosensitizers are physiologically inert in the absence of irradiation and only produce toxic reactive oxygen species (ROS) upon irradiation. Hence, PDT promises high selectivity and low systemic toxicities relative to chemo- or radio-therapy. However, PDT is intrinsically limited by a penetration barrier owing to shallow tissue penetration of light. Even with near-infrared (NIR) photosensitizers, the effective treatment depth of PDT is less than 1 cm of tissue. Due to this restriction, PDT has not yet gained general clinical acceptance.

Various approaches to PDT have been tested in light of this problem [1, 2]. In particular, X-rays, which afford great tissue penetration capacity, have been used to indirectly activate photosensitizers, a method referred to as X-ray-induced photodynamic therapy (X-PDT) or radiotherapy-radiodynamic therapy [3, 4]. X-PDT requires a nanoparticle scintillator and a photosensitizer whose emission matches the excitation of the scintillator. Under irradiation, the scintillator nanoparticle down-converts X-ray photons to visible or NIR photons, which activate the photosensitizer.

An alternative strategy, Cherenkov radiation induced photodynamic therapy, or CR-PDT, employs Cherenkov radiation to activate photosensitizers [4-6]. Cherenkov radiation refers to luminescence generated when a charged particle, for instance an electron or a positron, traverses a medium with a velocity exceeding the speed of light in that medium. A number of radionuclides such as ^{18}F, ^{64}Cu, ^{68}Ga, ^{89}Zr, ^{90}Y, ^{124}I, and ^{198}Au emit Cherenkov emission and have been investigated as light sources to activate photosensitizers [6-8]. Unlike X-PDT, where photosensitizers and scintillators are often integrated, the radionuclide can be administered separately from the photosensitizer in CR-PDT. For instance, it was demonstrated that ^{18}F-2-fluoro-2-deoxy-D-glucose (^{18}F-FDG), a small molecule positron emission tomography (PET) tracer, can be administered separately from photosensitizers such as quantum dots and TiO_2 nanoparticles to activate PDT [9, 10].

In this Chapter, we discuss the concept and underlying mechanisms of X-PDT and CR-PDT. We highlight recent progress in these related paradigms, with an emphasis on nanomaterials and nanoparticle engineering. Indeed, nanomaterials underpin advances in X-PDT and CR-PDT, serving as either scintillators or photosensitizers in these systems.

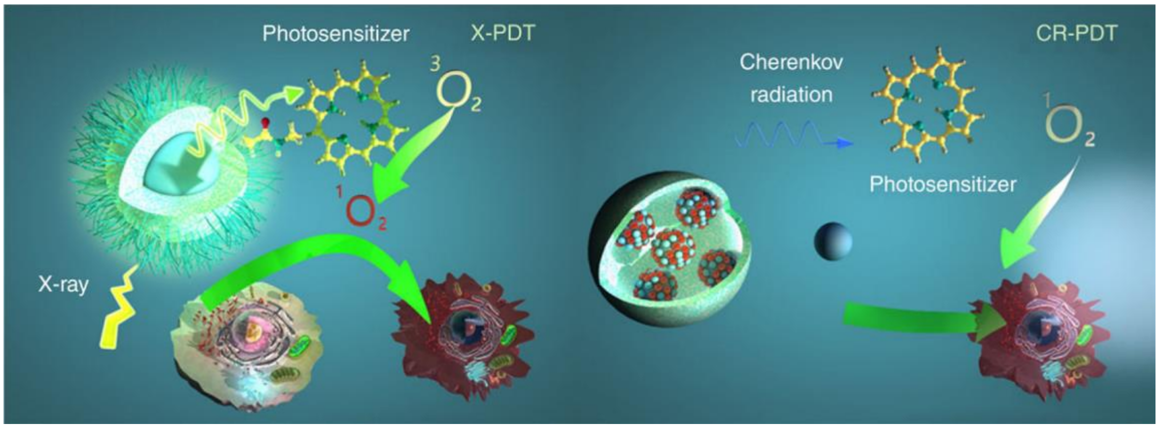

Figure 1.1 Schematic illustration for X-PDT and CR-PDT. Left: working mechanism for X-PDT. X-rays excite nanoscintillators, producing X-ray luminescence that in turn activates nearby photosensitizers to

produce cytotoxic ROS. Right: working mechanism for CR-PDT. Radioisotopes emit Cherenkov radiation that activates a photosensitizers and initiates PDT. [Reprinted with permission from Cline et al. (2019). Copyright 2015 John Wiley and Sons Publishers.]

1.2 Principal of X-ray induced photodynamic therapy

X-PDT often involves a composite nanoparticle containing a scintillator and a photosensitizer. Appropriate coating or conjugation chemistry strategies are required to combine or couple these two components, a concept first raised by Chen et al [11]. High-energy photons impinge the scintillator and thereby generate large quantities of electron−hole pairs in the scintillator's crystal lattice. This is followed by energy transfer among electron−hole pairs and the relaxation of excited ions to their ground states, with a concomitant luminescence [12]. It is hypothesized that nearby photosensitizers are transduced with this emitted energy and excited to their triplet states. The excited photosensitizers react with molecular oxygen ($^3O_2$), producing singlet oxygen ($^1O_2$) (i.e. the Type II reaction of PDT). Alternatively, the excited photosensitizer could directly react with surrounding water and biomolecules, generating ROS including hydrogen peroxide (H_2O_2), hydroxyl radicals ($\cdot OH$), and superoxide (O_2^-) (i.e. the Type I PDT reaction). To-date, data suggest that the Type II process is predominant in X-PDT [2, 13, 14].

The efficiency of X-PDT, in particular the number of $^1O_2$ produced during this multi-step process, depends on several variables. These include the concentration of the nanoparticle scintillator, the light yield of the scintillator material, the singlet oxygen quantum yield of the photosensitizer, and the efficiency of energy transfer. The following factors are often considered when designing an X-PDT nanoparticle.

First, the scintillator emission and photosensitizer excitation spectra should overlap to ensure efficient activation of the latter. Second, the two components must co-localize spatiotemporally for efficient energy transfer. This requirement is confounded in practice, wherein nanoparticles are exposed to a complex biological milieu containing lipids, nucleic acids, proteins, and interstitial fluids which may stifle luminescence [15]. This is why a composite nanoparticle containing both elements is often used. Third, the nanoparticle scintillators should reliably and intensely luminesce. In general, elements with more inner shell electrons (i.e. high-Z elements) capture high-energy photons more efficiently. Similarly, scintillator crystal structure modulates luminescence. For instance, pure cubic phase CsI particles exhibits weak X-ray luminescence relative to their thallium (Tl) doped counterparts [16, 17]. Despite the relevance of these properties, the impact of size on a scintillator's luminescence remains understudied. Reducing particle size increases surface-to-volume ratio and possibly increases the number of scintillation activator sites which may contribute to radiative transmission. For instance, YAG:Eu^{3+} nanoparticles show X-ray luminescence that is four times stronger than the bulk material [4]. In contrast, size reduction also increases surface defects which diminish luminescence intensity. This is evidenced in Gd_2O_3:Eu^{3+} nanoparticles, which show attenuated or no luminescence under high-energy beams [18, 19]. Some nanoscintillators may undergo phase transitions or melting during irradiation, which also lessen luminescence intensity [20, 21].

Like conventional PDT, X-PDT kills cancer cells by inducing apoptosis and necrosis [22-24]. ROS produced during X-PDT extensively damage nucleic acids and cellular lipids. Due to the transiency of ROS, $^1O_2$ in particular, damage is concentrated where photosensitizers are enriched. Hence, the spatial distribution of the scintillator-photosensitizer conjugates dictates the mechanistic specificity and efficacy of X-PDT. Our previous studies showed that relatively bulky

X-PDT nanoparticles (e.g. 400 nm in diameter) cause significant lipid peroxidation, probably due to their enrichment on the plasma membrane [25]. Lin et al. showed that nanoscale metal organic frameworks (nMOFs) bearing positive surface charges accumulate in mitochondria. Thus, X-PDT treatment caused depolarization of the mitochondrial membrane and apoptotic cell death [26]. Previous PDT and X-PDT studies note photosensitizer accumulation in and destruction of endosomes/lysosomes [23, 27]. While severe plasma membrane peroxidation may cause necrosis, damage to the mitochondria or endosomes/lysosomes often induces the intrinsic apoptosis pathway.

But the efficacy of X-PDT is not entirely decided by photosensitizer activation. This is because X-ray photons are not all converted to visible photons during X-PDT. Quite the opposite, most of the energy deposited in the tumor bed remains in the form of ionizing irradiation. Hence, X-PDT is essentially and intrinsically a combination of radio- and photodynamic-therapy. X-PDT nanoparticles increase tissue cross-section for high-energy photons and possibly alters the distribution of radicals in favor of cellular damage, thus improving therapeutic ratios (i.e. therapeutic effect relative to toxicity to normal tissues). In this sense, X-PDT can be viewed as a radiosensitizing technology for enhancing the efficacy of beam irradiation. This is why clonogenic and comet assays, which are conventional methods to evaluate the efficacy of radiosensitizers, are widely used to evaluate the performance of X-PDT agents.

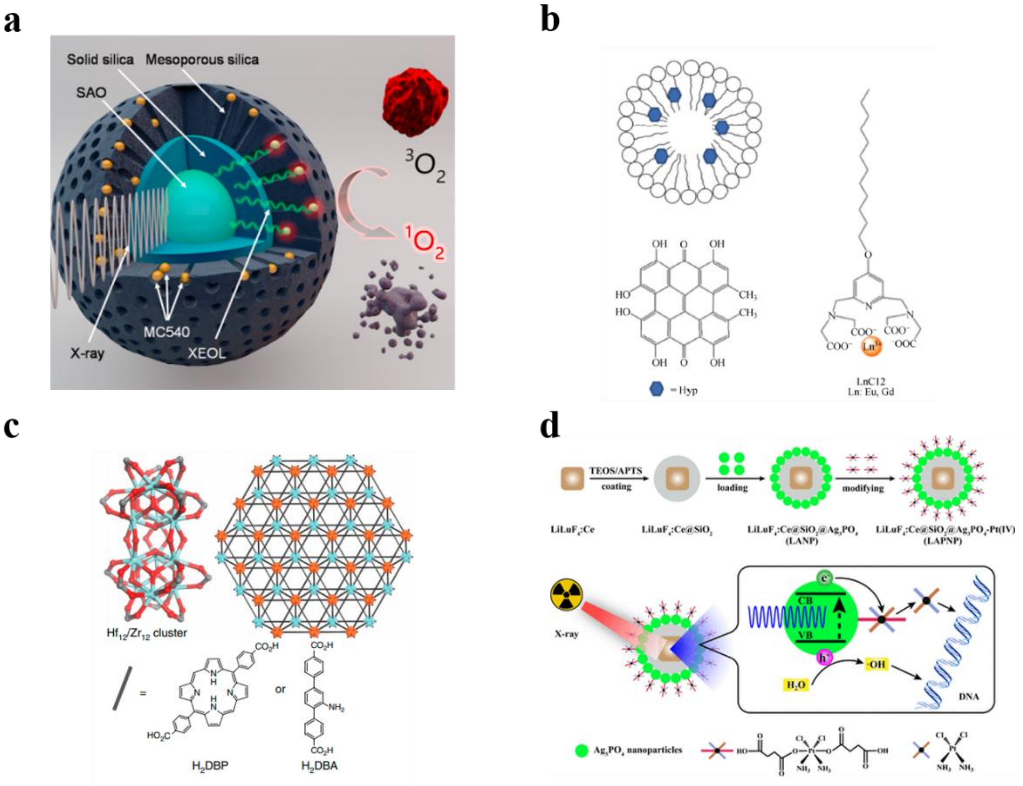

Figure 1.2 Representative nanoparticles for X-PDT. **(a)** Schematic illustration of the structure of M-SAO@SiO$_2$ nanoparticles, where a SAO core and is coated with mesoporous silica shell. MC540 was encapsulated in the silica pores. **(b)** Schematic illustration of the Hyp-GdEuC12 micellar particles constructed with amphiphilic LnC12 complex and the photosensitizer Hyp. **(c)** Schematic illustration of Hf12/Zr12 clusters, which are linked with H2DBP or H2DBA to generate nMOFs. **(d)** The structure of LiLuF$_4$:Ce@SiO$_2$@Ag$_3$PO$_4$@Pt(IV) nanoparticles (LAPNP) and their application for X-PDT. [Reprinted with permission from Chen et al. (2015), Kaščáková et al. (2015), Lu et al. (2018), and Wang et al. (2018). Copyright 2015 and 2018 American Chemical Society, Tsinghua University Press and Springer-Verlag Berlin Heidelberg, and Springer Nature.]

1.3 Synthesis of nanoscintillators

Nanoscintillators are nanoparticle scintillators that can transduce X-rays to visible or NIR photons. Using nanoscale particles is instrumental to systemic tumor targeting. Nanoparticles' large surface area also allows for loading a large amount of photosensitizer molecules. Over the years, nanoscintillators made of lanthanide fluorides [28-30], lanthanide oxides [31, 32], quantum dots [33-35], and MOFs [36, 37] etc. have been synthesized and tested for X-PDT [1, 4]. Depending on scintillator materials and surface properties, photosensitizers can be either conjugated or adsorbed onto nanoparticle surface or sometimes directly imbedded into nanoparticles.

Both bottom-up or top-down approaches have been explored for the synthesis of nanoparticle scintillators. Wet chemistry methods such as thermal decomposition and hydrothermal reactions are typical bottom-up approaches where nanoparticles grow from single atoms and/or basic building blocks. During the reaction, precursors are first dissociated at high temperature and/or pressure, and atoms/ligands of interest are self-assembled in a concentration- and temperature-dependent manner. Surfactants are often employed to passivate particle surface. Parameters such as reaction time, temperature, precursor amounts, and surfactant to precursor ratio can be adjusted to fine tune nanoparticle size and morphology. Dopant amount can also be adjusted and in turn tune X-ray luminescence properties. However, not all scintillators can be made by wet chemistry, which has restrictions including boiling temperature of solvents, solubility of precursors in solvents, aggregation of nanoparticles.

Top-down synthesis, such as attrition or milling strategies, are also widely used as a decomposition strategy to yield nanoparticles. These strategies start with bulk materials and break them down through etching and exfoliating building blocks. These methods are especially useful for scintillators made of ceramics that are difficult to be made from bottom up approaches. Bulk materials often feature high crystallinity which is inherited by the resulting nanoscintillator. However, top-down approaches are in general associated with suboptimal size control. Multiple steps of size selection and post-synthesis modification may be required to produce nanoparticles of desires sizes. Moreover, defects are generated during size reduction, which negatively affect luminescence properties. Overall, top down and bottom up approaches have their pros and cons which need to be considered when preparing nanoscintillators.

1.4 Surface modification and photosensitizer encapsulation

Post-synthesis surface modification is essential for most X-PDT agents. Surface modification improves the colloidal stability and sometimes the biocompatibility of the nanoparticles. Concomitantly, it introduces functional groups (carboxyl, primary amine, and thiol, etc.) onto nanoparticles so that the particles can be coupled to a tumor targeting ligand. Surface modification can also be used to impart docking moieties to which photosensitizer molecules can be tethered to or adsorbed onto. Notably, many photosensitizer molecules are hydrophobic and require a vehicle to deliver them to tumor sites.

While established coating methods exist, the exact strategy must be tailored to suit the scintillator materials and their surface properties. A polyethylene glycol (PEG) chain is often introduced to improve colloidal stability. Some scintillators can be directly functionalized with ligands or polymers containing carboxyl, thiol, and phosphate moieties. For instance, Ma et al. modified ZnS:Cu,Co nanoparticles with a heterodimer PEG possessing carboxyl and primary amine terminals [34]. While the carboxyl attaches to the particle surface, the amine can be used to couple the scintillator with targeting ligands such as the photosensitizer tetrabromorhodamine-123

(TBrRh123) via the EDC/NHS reaction [38]. Similarly, Liu et al. synthesized LaF_3:Tb nanoparticles using the precipitation method and modified the surface with $H_2N–(CH_2)_{10}–COOH(AA_{11})$. The nanoparticles were then covalently conjugated with a photosensitizer meso-tetra(4-carboxyphenyl) porphine (MTCP) [39].

The surfaces of scintillator nanoparticles made in organic solvents are often coated with ligands containing a long alkyl chain. A layer of phospholipids or amphiphilic polymers may be imparted to make nanoparticles water soluble. Photosensitizers can either be loaded into the lipid layer through hydrophobic interactions or tethered onto the surface through covalent coupling. For instance, Kaščáková et al. reported a liponanoparticle containing GdEuC12 micelles and hypericin [40]. The particles were prepared through micro-emulsion by mixing an aqueous solution containing $GdCl_3$ and $EuCl_3$ and a solution containing a C12 ligand. The resulting GdEuC12 micelle solution was then mixed with a stock solution of hypericin, and the photosensitizer hypericin was directly incorporated into the hydrophobic core.

Another common strategy is coating nanoparticles with a layer of silica. This approach applies for nanoparticles made from both bottom-up and top-down methods. Silane derivatives such as (3-aminopropyl) triethoxysilane (APTES) and (3-mercaptopropyl) trimethoxysilane (MPTS) can be mixed with tetraethoxysilane (TEOS) as coating precursors to introduce functional groups such as primary amine and thiol onto the silica surface. The resulting nanoparticles can be PEGylated and/or coupled with photosensitizers as well as other functional molecules. For instance, Wang et al. coated $LiLuF_4$:Ce nanoparticles with silica using TEOS, and further modified them with Ag_3PO_4 nanoparticles and a cisplatin prodrug by covalent binding [41, 42]. Ag_3PO_4 nanoparticles were introduced as photosensitizers and attached strongly to surface amino groups. A cisplatin prodrug Pt(IV) was tethered to the surfaces of the Ag_3PO_4 nanoparticles, acting as sacrificial electron acceptors and improving hydroxyl radical (·OH) generation. Alternatively, particle surfaces can be coated with a layer of mesoporous silica, into which photosensitizers can be loaded. For instance, we synthesized $LiGa_5O_8$:Cr using sol-gel reactions and ball-milled the material down to nanoscale particles. The resulting nanoparticles were coated with mesoporous silica, into which a photosensitizer 2,3-naphthalocyanine was loaded [43]. Sun et al. employed an ion-incorporated method where metals such as Zn, Mn, and Eu were loaded into mesoporous silica to form silicate nanoscintillators [44]. The surface of the silica was further coordinated with rose bengal and arginylglycylaspartic acid (RGD) peptide to achieve final mesoporous silicate nanoscintillators.

While small molecule photosensitizers are most common, inorganic materials such as ZnO and TiO_2 can also function as photosensitizers and have been explored to construct X-PDT agents. Yang et al. synthesized TiO_2 nanoparticles via the sol-gel method and doped carbon atoms into the anatase lattice to narrow the nanoparticle band gap [45]. The resulting carbon-doped TiO_2 nanoparticles can be activated by X-rays to produce ROS and kill cancer cells. Zhang et al. similarly synthesized Ce^{3+}-doped $LiYF_4$ nanoparticles by thermal decomposition and coated them with silica [30]. MPTS was mixed with TESO during silica coating so that the resulting nanoparticles presented thiol groups on their surfaces. Zn^{2+} was first immobilized onto particle surfaces via interactions with thiol groups, and then grown into a ZnO shell by supersonic treatment. The particle surface was further modified with PEG to improve biological compatibility. Unlike conventional scintillators, nanoscale metal organic frameworks (nMOFs) are constructed from metal binding sites and coordinated organic ligands [36, 37, 46-48]. During synthesis, photosensitizer molecules can be directly embedded into nMOFs with high loading capacity and accuracy. For instance, Liu et al. reported a nMOF composed of hafnium (Hf^{4+}) and tetrakis (4-

carboxyphenyl) porphyrin (TCPP) [49], where TCPP serves as both a photosensitizer and a coordinating ligand. The nMOFs were further coated with poly(maleic anhydride-alt-1-octadecene)-poly(ethylene glycol), an amphiphilic polymer. The same group also synthesized several other nMOF-based X-PDT agents using a similar strategy [26, 36, 47, 50-52].

1.5 X-PDT nanoplatforms and their applications

As discussed, nanoscintillators made of lanthanide fluorides [28-30], lanthanide oxides [31, 32], quantum dots [33-35], and nanoscale metal-organic framework (nMOFs) [36, 37, 53-55] have been prepared and subsequently coupled with or adsorbed onto matching photosensitizers. The X-PDT mediated anti-cancer potency of these conjugates has been tested both *in vitro* and *in vivo*.

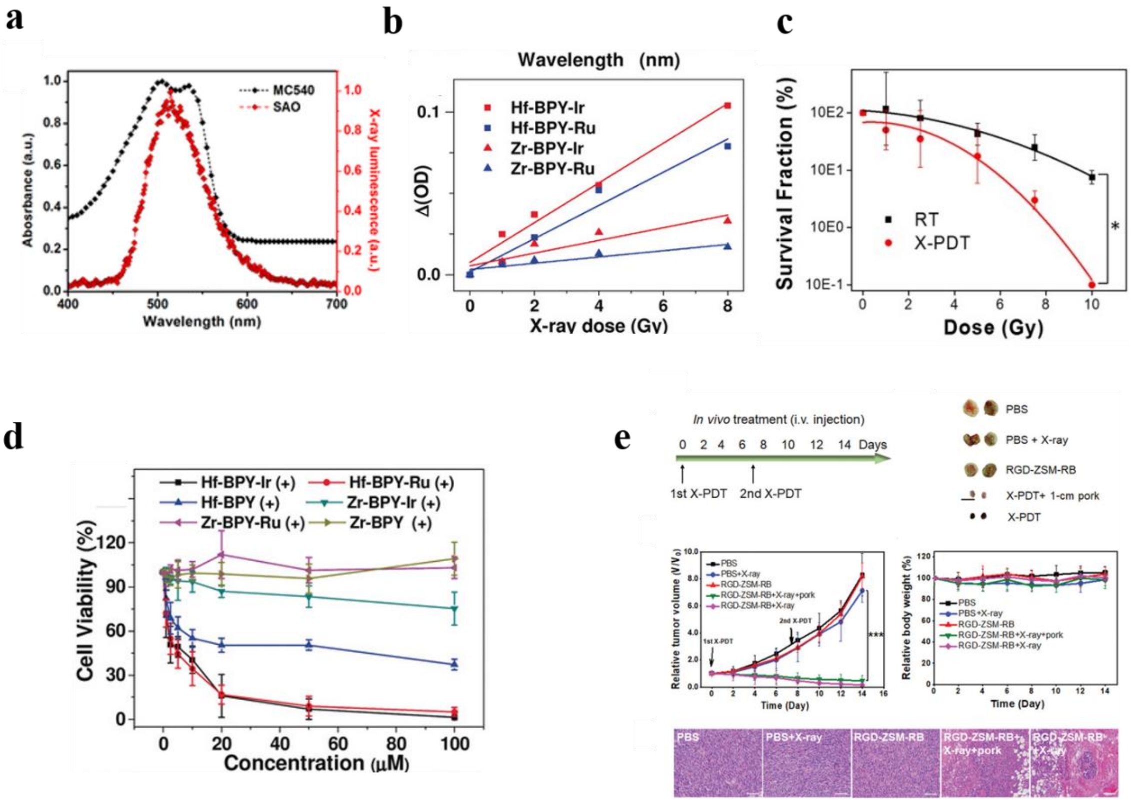

Figure 1.3 *In vitro* and *in vivo* assessments of X-PDT. **(a)** A good overlap between X-ray induced luminescence of a scintillator (SAO) and the absorbance of a photosensitizer MC540 is essential for successful X-PDT. **(b)** Dose-dependent radical generation can be evaluated in solutions using sensors such as 4-nitroso-N,N-dimethylaniline (RNO). **(c,d)** Clonogenic **(c)** and viability **(d)** assays are commonly used to evaluate X-PDT efficacy in vitro. **(e)** Animal studies are often performed to evaluate the efficacy and safety of X-PDT *in vivo*. [Reprinted with permission from Chen et al. (2015), Lan et al. (2017) and Sun et al. (2019). Copyright 2015, 2017 and 2019 American Chemical Society and WILEY-VCH Verlag GmbH & Co. KGaA, Weinheim]

1.5.1 Lanthanide fluorides and oxides

Multiple lanthanide fluorides have been used as scintillators, and they were some of the first to be tested for X-PDT. For instance, LaF_3:Tb exhibits strong X-ray luminescence at ~540 nm. Liu et al. constructed LaF_3:Tb-MTCP nanoparticles and showed that the conjugates under X-ray irradiation can quench anthracenedipropionic acid, a chemical sensor responds to singlet oxygen [39]. This study represents one of the earliest proof-of-concept of X-PDT. In another instance, Tang et al. synthesized mesoporous LaF_3:Tb nanoparticles using a hydrothermal reaction and loaded rose bengal into the pores of the particle surface [29]. Steady-state spectrum and fluorescence delay dynamic analysis confirmed that LaF_3:Tb nanoparticles activated the photosensitizer through the fluorescence resonance energy transfer (FRET) process with an impressively high $^1O_2$ production efficiency of 85%.

Clement et al. showed that CeF_3 nanoparticles, either uncoated or adsorbed with verteporfin, generated $^1O_2$ under 8 keV of X-ray irradiation [56]. The $^1O_2$ quantum yield was as high as 0.79 ± 0.05. According to their estimates, the $^1O_2$ generated from the CeF_3-verteporfin conjugates over 60 Gy administered via 6 MeV and 30 KeV beams were $(1.2 \pm 0.7) \times 10^8$ per cell and $(2.0 \pm 0.1) \times 10^9$ per cell, respectively. According to Niedre et al, 5×10^7–2×10^9 $^1O_2$ per cell are sufficient to induce cell death [57]. These results suggest that CeF_3-verteporfin conjugates may significantly enhance radiotherapy.

More recently, Zhang et al. studied $LiYF_4$:Ce nanoparticle-based X-PDT [30]. Specifically, $LiYF_4$:Ce nanoparticles were coated with SiO_2 and then ZnO in a core/shell/shell structure. The resulting nanoparticles form electron–hole pairs in the ZnO shell under irradiation, which in turn produce ROS such as hydroxyl radicals, as indicated by effective methylene blue quenching. When tested in HeLa tumor-bearing mice, the nanoparticles potently mediated X-PDT and cause almost complete tumor eradication.

Wang et al. reported that $LiLuF_4$:Ce nanoparticles can be coated with SiO_2 and then covalently decorated with Ag_3PO_4 nanoparticles and a cisplatin prodrug Pt(IV) [41]. *In vitro* experiments confirmed efficient production of ·OH under both normoxic and hypoxic conditions. Balb/c nude mice were inoculated with HeLa cells, generating tumors into which nanoparticles injected prior to 4 Gy of X-ray irradiation. Compared to radiation alone, nanoparticles plus radiation more efficiently killed cancer cells and abrogated tumor growth.

Similar to lanthanide fluorides, lanthanide oxides are commonly exploited as scintillators for X-PDT. For instance, Bulin et al. synthesized Tb_2O_3 nanoparticles via the sol-gel method and coated them with a polysiloxane layer [31]. The nanoparticles were then covalently coupled with porphyrin. Time-resolved laser spectroscopy coupled with $^1O_2$ probes confirmed that the nanoparticle conjugates produce $^1O_2$ under X-ray radiation.

Scaffidi et al. conjugated Y_2O_3 nanoparticles with TAT, a cell-penetrating peptide, and psoralen, a photosensitizer [32]. Y_2O_3 nanoparticles emitted UV light after absorbing X-ray radiation, activating psoralen and causing the cross-linking of adenine and thymine residues in

DNA. When tested *in vitro* against PC-3 cells, Y_2O_3-psoralen conjugates under irradiation more efficiently killed cancer cells than psoralen-free Y_2O_3 nanoparticles. Vadim et al. synthesized Y_2O_3:Eu and $Y_3Al_5O_{12}$:Eu particles using the Pechini method and self-propagating high-temperature synthesis [58, 59]. These nanoparticles exhibited 610 nm X-ray luminescence and when physically mixed with photosensitizers such as silicon phthalocyanine, destroyed fibroblasts under X-ray irradiation *in vitro* with almost zero colonies survived.

1.5.2 Ceramics

Many promising ceramics have been employed as scintillators for X-PDT. For instance, we synthesized ~80 nm $SrAl_2O_4$:Eu nanoparticles by ball milling, and we coated them with a layer of solid silica which protected the core from aqueous degradation [25, 60]. Subsequently, a mesoporous silica shell was imparted, into which MC540, a photosensitizer, was loaded. We confirmed that $SrAl_2O_4$:Eu nanoparticles can convert X-rays to visible photons, which thereby activate MC540 to produce cytotoxic $^1O_2$. Studies in nude mice bearing H1299 human non-small cell lung carcinoma-derived and U87MG human glioblastoma-derived tumors both demonstrated the therapeutic efficacy of M-SAO@SiO_2 nanoparticles. After X-PDT, the tumors of treated mice were impalpable after 16 days, whereas tumors in control mice grew to termination (> 1.7 cm in diameter).

Rossi et al. synthesized hybrid core/shell SiC/SiO_x ($1.8 < x < 2$) nanowires using chemical vapor deposition [61]. These nanowires were conjugated with a tetracarboxyphenyl porphyrin derivative using click-chemistry. When irradiated with 6 MV beams, the nanowires generated $^1O_2$ even at relatively low doses (e.g. 0.4–2 Gy). Clonogenic assays with A549 cells showed that X-PDT via the SiC/SiO_x nanowires reduced colony formation. Sun et al. developed a simple and high throughput method to synthesize metal-doped silicate nanoparticles, which are also good scintillators [44]. By adjusting the choice of metal dopant (e.g Zn, Mn, Eu), the luminescence of the silicate nanoscintillators was able to be tuned between 450-900 nm. These nanoparticles were coupled with Rose Bengal and RGD, a tumor targeting ligand. When tested in a U87MG tumor model, silicate nanoparticles plus irradiation led to 98.1% tumor inhibition relative to radiation alone.

We also studied $LiGa_5O_8$:Cr, which emits near-infrared X-ray luminescence [43]. Briefly, bulk $LiGa_5O_8$:Cr was first synthesized through a sol-gel a reaction, and ground to ~100 nm nanoparticles by ball milling. The nanoparticles were then coated with mesoporous silica and loaded with 2,3-naphthalocyanine, a photosensitizer whose excitation matches the emission of $LiGa_5O_8$:Cr. Unlike most scintillators whose luminescence is short-lived, $LiGa_5O_8$:Cr emits strong afterglow even hours after irradiation. This allows sustained production of radicals, which enhance treatment. The NIR luminescence also permits *in vivo* tracking of the $LiGa_5O_8$:Cr nanoparticles, making concomitant therapeutic monitoring possible. In a proof-of-concept study, $LiGa_5O_8$:Cr-naphthalocyanine nanoparticles were coupled with cetuximab, an anti-EGFR antibody, and intravenously injected into an orthotopic lung cancer model established with H1299 cells. The nanoparticles selectively accumulated in tumors by targeting epidermal growth factor receptor, which was specifically monitored by tracking the afterglow of the nanoparticles. Compared to radiation alone, $LiGa_5O_8$:Cr-naphthalocyanine nanoparticles plus X-rays significantly retarded tumor growth. This is the first demonstration showing that systemically administered scintillators can mediate X-PDT to improve radiotherapy against deep-seated tumors.

1.5.3 Quantum dots

Quantum dots (QDs) are semiconductor nanoparticles. Owing to the quantum confinement effect, many QDs are good scintillators and exhibit superior light yield [62-65]. While QDs are predominantly investigated as fluorescence tags, their potential in X-PDT has also been demonstrated.

As early as 2007, Takahashi et al. tested the feasibility of using CdTe and CdSe QDs to mediate X-PDT [14]. They observed that 20-170 keV photons were efficiently attenuated (up to 90%) when they traversed CdTe or CdSe nanoparticle solutions with concentrations varying between 0.01 and 100 wt%. The QDs produced ROS in a dose-dependent manner when coupled with dihydroethidium. Clonogenic assays with HeLa suggested that the nanoparticles function as radiosensitizers. Later, Lemon et al. prepared nanoparticle conjugates made of Pd-porphyrin and CdSe QDs and confirmed energy transfer and porphyrin activation under UV light irradiation both experimentally and theoretically [66]. Ma et al. studied ZnS:Cu,Co QDs for X-PDT [34]. These nanoparticles were conjugated with tetrabromorhodamine-123. Successful conjugation and energy transfer were supported by diminished nanoscintillator emission and concomitant increase of photosensitizer emission. ZnS:Cu, Co nanoscintillators exhibit afterglow, eliciting consistent photosensitizer activation and $^1O_2$ production after X-ray irradiation has ended. The afterglow also permitted the visualization of cells under 2 Gy X-ray excitation, indicating its potential as a light source for tumor imaging.

1.5.4 nMOFs

The Lin group first reported the synthesis of nMOF-based X-PDT agents via a post-synthetic metalation method. These were constructed with $[Hf_6O_4(OH)_4(HCO_2)_6]$ and a photosensitizer ligand, such as tricarboxylate derivatives of $Ir[bpy(ppy)_2]^+$ or $[Ru(bpy)_3]^{2+}$. The authors found that the nanoparticles efficiently mediate X-PDT against colon cancer cells [53]. Heavy metal Hf-based secondary building units can be excited by X-rays, indirectly activating the photosensitizer embedded in the matrix. The nMOFs feature an ultrathin 2-D structure (ca. 1.2 nm in thickness and 500 nm in diameter) and benefit from enhanced diffusion of $^1O_2$ generated within the particles. Solution-based study confirmed that $^1O_2$ production depends on the dose of radiation administered, and Hf MOFs appeared to generate more $^1O_2$ than their Zr counterparts. Studies with colon adenocarcinoma cells and tumor bearing animals demonstrated impressive treatment efficacy, establishing nMOFs as attractive X-PDT agents.

The same group later reported a series of hafnium-based nMOFs, including those fabricated using 5,15-di(p-benzoato)porphyrin (DBP) and 5,10,15,20-tetra(p-benzoato)porphyrin (TBP) as the bridge ligands [47]. They injected nanoparticles intratumorally into TUBO and CT26 tumor-bearing mice and gave the animals 2-Gy of radiation daily for 5 days. Tumors were completely eradicated after 30 days. Interestingly, the treatment also elicited an anti-tumor immune response. nMOFs encapsulated with an inhibitor of the immune checkpoint enzyme indoleamine 2,3-dioxygenase (IDO) generated an impressive abscopal effect, causing regression of distant tumors.

The Lin group also developed nMOFs which target a specific organelle, such as the mitochondria [26]. Specifically, they prepared a tris(2,2'-bipyridyl)ruthenium(II) [$Ru(bpy)_3^{2+}$]-based hafnium nMOFs with a diameter less than 100 nm. The nanoparticles carry positive charge on their surfaces due to the delocalized lipophilic cation $Ru(bpy)^{3+}$, prompting their intra-mitochondrial accumulation. *In vitro* studies with colon adenocarcinoma cells showed a significant drop in viability when treated with the nMOF plus X-ray combination. The REF_{10} value, which measures radiation enhancement at the dose which produces 10% survival, is 2.68, compared to 1.50 when cells were treated with nMOFs lacking the Ru photosensitizer. Interestingly, mechanistic studies also confirmed mitochondrial membrane depolarization, cytochrome c release, and the induction of intrinsic apoptosis. Impressive *in vivo* results were obtained with a modest fractional dose (1 Gy per fraction and 6 fractions in total).

In summary, nanoparticles made of conventional scintillator materials have been synthesized and coupled with photosensitizers to enable X-PDT. Moreover, new nanomaterials based on nMOFs are constructed for X-PDT applications.

Table 1. Summary of X-PDT studies

Publication Year	Dose	Transducer	Size /nm	Photosensitizers	Attachment strategy	Exp. subject	Ref.
2006	N/A	LaF_3:Ce, LuF_3:Ce, CaF_2:Mn, CaF_2:Eu, BaFBr:Eu, BaFBr:Mn, $CaPO_4$:Mn ZnO, ZnS, TiO_2	N/A	N/A	N/A	concept	[11]
2009	0.1-100 Gy	LaF_3:Ce, LuF_3:Ce, CaF_2:Mn, CaF_2:Eu, BaFBr:Eu, BaFBr:Mn, $CaPO_4$:Mn ZnO, ZnS, TiO_2	N/A	photofrin, fullerenes, TiO_2	N/A	in solution & in silico	[15]
2015	100/500 keV	Gd_2O_3, Gd_2O_2S, Lu_2O_3, CdSe, InP	100	N/A	N/A	in solution & in silico	[67]
2008	250 kV, 0.44 $Gy{\cdot}min^{-1}$	LaF_3:Tb	15	MTCP	covalent binding	in solution	[68]
2015	75 kV, 20 mA	LaF_3:Tb	39	rose bengal	covalent binding	in solution	[29]
2015	75 kV, 20 mA	LaF_3:Tb @SiO_2	40	rose bengal	covalent binding	in solution	[69]
2013	44 kV, 40 mA, 14.6 Gy	Tb_2O_3	3	porphyrin	covalent binding	in solution	[31]
2015	400 mA, 10^{15} $photons{\cdot}s^{-1}$	GdEuC12 micelles	4.6	hypericin	physical loading	in solution	[40]
2016	40 kV, 15 mA	$[M_6L^i_8L^a_6]^n$ complexes	N/A	self	complex	in solution	[70]
2021	50 kV, 80 μA	$NaLuF_4$:Dy^{3+},Gd^{3+}	11.1	rose bengal and merocyanine 540	pore loading	in solution	[71]
2007	1-10 Gy	TiO_2, ZnS:Ag, CeF_3, CdTe and CdSe	N/A	self	N/A	HeLa cells (*in vitro*)	[14]
2011	120 kVp, 20 mA	Gd_2O_2S:Tb	20 μm	photofrin II	co-location	glioblastoma cells (*in vitro*)	[72]
2011	2 Gy	Y_2O_3	12	psoralen	physical attachment	PC3 cells (*in vitro*)	[32]
2014	120 kV, 2 Gy	ZnS:Cu,Co	4	TBrRh123	covalent binding	PC3 cells (*in vitro*)	[34]
2015	6 MV, 2 Gy	SiC/SiO_x nanowires	20	H_2TPACPP	covalent binding	A549 cells (*in vitro*)	[61]

2020	320 kV, 4 Gy	Gold nanoparticles in liposomes (Lipo-VP-Au)	10, 5	verteporfin	physical loading	HCT116 cells and CCD841 CoN cells (*in vitro*)	[73]
2020	100 kV or 6 MV, 100-400 cGy	TiO_2-MSN	70-110	PpIX	Pore loading	HT-29 cells (*in vitro*)	[74]
2020	130 kV, 5 mA, 4 Gy	CaF_2:Ln (Tb or Eu)	13.4	N/A	N/A	CT26 cells (*in vitro*)	[75]
2021	320 kV, 4 Gy	PLGA–VP–PFOB (secondary electrons from tissue)	100-140	verteporfin	physical loading	PANC-1 cells (*in vitro*)	[76]
2021	320 kV, 10 mA, 5 Gy	AGuIX@Tb	11	5-(4-carboxyphenyl succinimide ester)-10,15,20-triphenyl porphyrin (P1)	covalent binding	U-251 MG cells (*in vitro*)	[77]
2015	220 keV, 8 Gy	$LiYF_4$:Ce	40	ZnO	coating	animal (i.t.)	[30]
2016	5 Gy	$SrAl_2O_4$:Eu@mSiO_2	73.5	MC540	pore loading	animal (i.t.)	[25]
2018	80 kV, 4 Gy	$LiLuF_4$:Ce	30	Ag_3PO_4-Pt(IV)	coordination	animal (i.t.)	[41]
2017	120 kV, 20 mA	$[Hf_6O_4(OH)_4(HCO_2)_6]$ SBUs	500	Ir[bpy ppy$)_2]^+$ $[Ru(bpy)_3]^{2+}$	post-synthetic metalation	animal (i.t.)	[53]
2018	5 × 0.5 Gy	Hf_6 SBUs, Hf_{12} SBUs	295.3, 91.3	$Ir(DBB)[dF(CF_3)ppy]_2^+$	post-synthetic metalation	animal (i.t.)	[78]
2015	50 kV, 70 µA, 0.5 Gy	$SrAl_2O_4$:Eu	150	MC540	pore loading	animal (i.t.)	[60]
2019	90 kV, 30 mA, 5 Gy	pHLIP-Cu-Cy	200	Self	covalent binding	animal (i.t.)	[79]
2019	0.5 or 1 Gy·fraction^{-1}	Hf-DBP nMOL	150	Self	post-synthetic metalation	animal (i.t.)	[52]
2020	8 Gy	Y_2O_3:Eu@SiO_2	160	N/A	N/A	animal (i.t.)	[80]
2020	4 Gy	PLGA-gold nanocarrier	160	verteporfin	covalent binding	animal (i.t.)	[81]
2017	50 kV, 70 µA, 5 Gy	$LiGa_5O_8$:Cr	100	NC	pore loading	animal (i.v.)	[43]
2018	50 kV, 60 µA, 0.18 Gy	$ZnGa_2O_4$:Cr/W	15	$ZnPcS_4$	pore loading	animal (i.v.)	[82]
2018	250 kVp, 15 mA	Hf-DBB-Ru	98	DBB-Ru	coordination	animal (i.v.)	[26]
2019	50 kV, 70 µA, 6 Gy	$Gd_2(WO_4)_3$:Tb	50	MC540	physical attachment	animal (i.v.)	[83]
2019	50 kV, 70 µA, 1 Gy	Zn_2SiO_4:Mn	30-120	rose bengal	bioconjugation	animal (i.v.)	[44]
2019	80 kV, 10 mA, 0.08 Gy/min	TiO_2:C	300	TiO_2	post-synthetic metalation	animal (i.v.)	[45]
2019	1 Gy·fraction^{-1}	W_{18}@Hf_{12}-DBB-Ir	114.8	DBB-Ir	post-synthetic metalation	animal (i.v.)	[51]
2020	2 Gy	GNRs@mSiO_2−EuBA	86, 51.2	Hematoporphyrin (HP)	covalent binding	animal (i.v.)	[84]
2020	2 Gy	Polyoxomolybdate (POM) nanoclusters	5.9	rose bengal	pore loading	animal (i.v.)	[85]

2020	50 kV, 70 µA, 1 Gy	gold clustoluminogens (AIE-Au)	68.2	rose bengal	bioconjugation	animal (i.v.)	[86]
2020	50 kV, 70 µA, 4 Gy	$Zn_3Ga_2GeO_8$:Cr3+, Yb3+, Er3+ (mZGGOs)	100	silicon phthalocyanine (Si-Pc)	pore loading	animal (i.v.)	[87]
2020	6 Gy	$NaGdF_4$:Tb,Ce@$NaGdF_4$	19	rose bengal	bioconjugation	animal (i.t.)	[88]
2018	0.5 Gy·fraction^{-1}	DBP-Hf, TBP-Hf nMOFs	72	self	post-synthetic metalation	animal (i.t.& i.v.)	[47]
2018	1 Gy·fraction^{-1}	Hf-DBB-Ru nMOFs	98	$Ru(bpy)_3^{2+}$	post-synthetic metalation	animal (i.t.& i.v.)	[26]

1.6 Singlet oxygen production for effective cancer cell killing

To effectively kill nearby cancer cells, the amount of singlet oxygen generated needs to fulfill the estimated threshold called Niedre killing dose[15]. Here we utilized an established model elsewhere to calculate the scintillation yield of the nanoparticles.

Equation: $$N^1O_2 = 3.2D * Mv * \Phi_1O_2$$

i. Where N^1O_2 is number of Singlet oxygen molecules generated per cell

ii. D is the X-ray dose in Gy delivered

iii. M (unitless) is the absorption of the nanoparticle cores relative to that of tissue and is strongly dependent on incident X-ray energy

iv. v is the volume fraction of the cell occupied by the nanoparticle cores, also unitless

v. Φ_1O_2 denotes the efficiency with which incident X-ray energy is converted into singlet oxygen (in units of molecules of singlet oxygen generated per MeV absorbed X rays)

vi. The conversion factor 3.2 arises from the conversion between Gy and MeV

Based on the Niedre killing dose, the number of singlet oxygens need to approach 5.6×10^7 molecules per cell, and a typical concentration of singlet oxygen causing effective cytotoxic would be: 5×10^7–2×10^9 molecules per cell.

1.6.1 Cellular uptakes of nanoparticles

To better understand the cancer cell killing effect, here we made several assumptions to simplify our calculations.

i. Assume a spherical cell 10 µm diameter (density 1 g/ml).

Total volume based on $4/3*\Pi r^3 = 523.33\ \mu m^{3\,=}\ 5.23*10^{-7}\ mm^3$

ii. Here we pick up CsI nanoparticles for example. Assume we have 200 ug/ml with 50 ul = 10 ug CsI solutions (ρCsI = 4.51 g/cm^3) and only 1.0 ug (10%) goes into tumors.

The volume of particles would be $= 1.0/4.51*\ 10^3 = 221.72\ \mu m^3$

iii. # of nanoparticles per cell $= 1/252*6.02*10^{23}*10^{-9}*10^{-6} = 2.38*\ 10^6$

iv. Assuming we have 10^6 cells for 4.186 mm^3 tumor.

Then for a tumor of 50 mm^3 we have $11.93*10^6$ cancer cells = 4188.79 μm^3

v. **The volume fraction v** would then be = 221.72/4188.79 = 5.29 %

vi. Among the volume of cancer cells, we also have a volume ratio of 10 % for cell nucleus, which would then be: (1-5.29%) *10% = 9.471 % volume ratio.

1.6.2 Radiation ratio of RT versus PDT

ρCsI = 4.51 g/cm3

ρt densities of the nanoparticle core and the surrounding tissue = 1.1 g/cm3

µI, µCs and µt are mass energy absorption coefficients for the respective elements and for soft tissue

i. For 16 MeV

µI=2.98*10-2 µCs= 3.026*10-2 µt= 1.4*10-2

M = ρCsI/ρt*(0.488µI+0.512uCs)/ µt = 4.1*(0.488*2.98+0.512*3.026)/1.42= 8.672

In view of the radiation ratio of PDT versus RT = M*5.29 %/9.471 % = 4.84 or approximately 5:1 ratio

ii. For 50 KV

$$\mu I=6.573 \quad \mu Cs= 6.618 \quad \mu t= 3.99*10-2$$

$M = \rho CsI/\rho t*(0.488\mu I+0.512uCs)/ \mu t = 4.1*(0.488*6.573+0.512*6.618)/0.0399= 678.299$

In view of the radiation ratio of PDT versus RT = M*5.29 %/9.471 % = 378.86 or approximately 400:1 ratio.

1.6.3 Limit of light yield: an energy transfer from NPs to PS

$$\text{Yield}= S* C*P$$

1. S= light yield of Scintillator 41 ph/KeV * 50 % photons for 380-420 nm = 2.1 * 104 ph/MeV
2. C= energy transfer from particle to PS (> 0.75 for FRET) Supposed to be 0.7 for our case and need to be proofed by experiment
3. P= efficiency with which the excited photosensitizer generates singlet oxygen (usually > 0.89, for PPIX we take 0.56)

1.6.4 Singlet oxygen generation efficiency

For perfect energy transition, one cell absorbs 1 MeV X-ray energies and can convert to $3.23*10^5$ photons/MeV (400 nm light 3.1 eV) Based on Luminescence spectrum of CsI:Na, assuming 50% photons locate at 380- 420 nm

$$\text{S yield} = 1.62 *10^5 \text{ photons/MeV}$$

Suppose we have same concentration of PPIX in each cell with a singlet oxygen generation quantum yield of 0.56, ALA induce the concentration of PPIX to be 4 times higher, then for PPIX it can generate = Yield= S* C*P = $3.23*10^5 * 0.5* 4 *0.7 * 0.56 = 2.532 *10^5$

i. For 50% energy conversion and 60 Gy

50 KV Equation: $N^1O_2 = 3.2D * Mv * \Phi_1O_2 = 3.2*60*678.299*0.0529*1.62*10^5 = 4.38*10^8$

16 MV Equation: $N^1O_2 = 3.2D * Mv * \Phi_1O_2 = 3.2*60*8.672*0.0529*1.62*10^5 = 5.59*10^6$

ii. For CsI light yield and 60 Gy

50 KV Equation: $N^1O_2 = 3.2D * Mv * \Phi_1O_2 = 3.2*60*678.299*0.0529*2.1*10^4 = 5.67*10^7$

16 MV Equation: $N^1O_2 = 3.2D * Mv * \Phi_1O_2 = 3.2*60*8.672*0.0529*2.1*10^4 = 7.25*10^5$

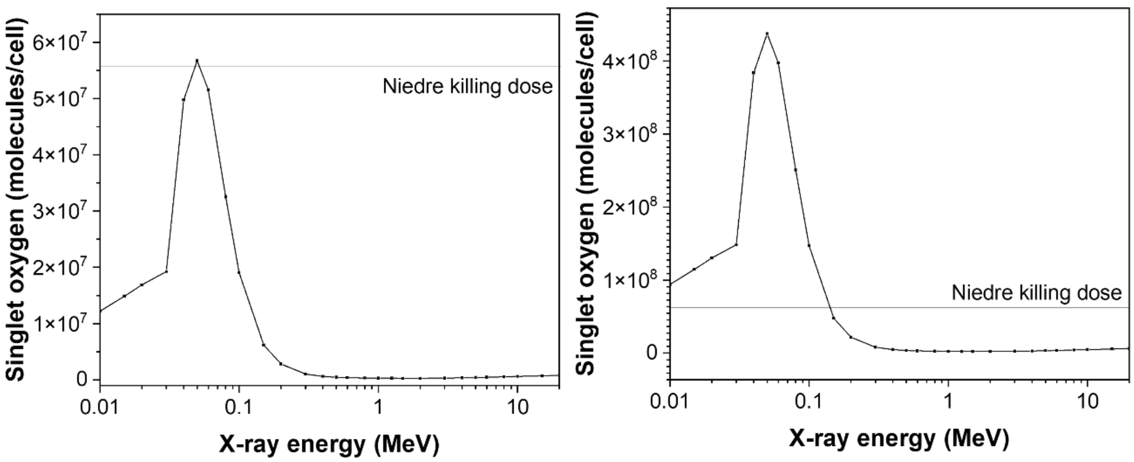

Based on CsI light yield

Based on 50 % energy conversion

Figure 1.4 Calculated singlet oxygen generation under 60 Gy

1.6.5 Discussion of X-PDT with respect to its RT and PDT component

i. Under low X-ray power (50 KV):

It seems a high number of energies (400:1) was absorbed and functionalized through PDT process. Previous calculations have shown that under 50 KV and 60 Gy X-ray dose, the PDT part in X-PDT can reach the Niedre killing dose for an effective amount of singlet oxygen generation related to cell death. Besides, the RT itself might promote the treatment efficacy by breaking DNA double-strand and lead to cell death. Furthermore, it is worth mentioning that our nanoparticles have XEOL properties with its spectrum starting from ultraviolet part. The light localized around 420 nm can be utilized for PDT while those ultraviolet light either from scintillator or unknown particles in the complex microenvironment, instead of motivating photosensitizers, can be potentially applied for direct DNA damage. Needless to say, thermal effect, scattering, and other radicals that could potentially occur during X-PDT.

Thus, we think under low X-ray power, PDT part dominates. And with the addition of RT and a series of scattering, thermal effect, radicals, X-PDT eventually results in an observed synergistic efficacy superior to RT or PDT alone.

ii. Under high X-ray power (16 MeV):

The energy ratio regarding PDT and RT is approximately 5: 1. Previous calculations also indicate that under such a high power, the amount of singlet oxygen generated through PDT in this progress was only 1 % compared to the Niedre killing dose.

Thus, under high X-ray power, the treatment works more like a RT progress with the decoration of PDT and a series synergistic effect derived from the complicated microenvironment.

CHAPTER 2

Ultrathin gold nanowires to enhance radiation therapy[1]

---

[1] Reprinted with permission from Fangchao Jiang[*], Lin Bai[*], Renjie Wang, Chaebin Lee, Hui Wang, Weizhong Zhang, Wen Jiang, Dandan Li, Bin Ji, Zibo Li, Shi Gao, Jin Xie, and Qingjie Ma. Accepted by Journal of Nanobiotechnology. 2020, 18, 131. * Authors contributed equally to this work*

ABSTRACT

Radiation therapy (RT) is a main treatment option for cancer. Due to normal tissue toxicity, radiosensitizers are commonly used to enhance RT. In particular, high-Z nanoparticles, such as gold nanoparticles, have been investigated as radiosensitizers. So far, however, the studies have been focused on gold nanospheres (GNSs). In this study, we assessed the potential of ultra-thin gold nanowires (GNWs) as a radiosensitizer, which is the first time. Ultrathin gold nanowires (GNWs) and gold nanospheres (GNSs) were synthesized and further characterized by DSPE-PEG(2000) Amine. Those materials were then dispersed in PBS for in vitro and in vivo studies. For in vitro studies, GNWs or GNSs solution was mixed with RPMI cell culture medium and incubated together with 4T1 cells. X-ray was applied as radiation source. Our studies showed that GNWs are superior to GNSs with regards to enhancing radical production under radiation. *In vitro* analysis found that GNWs could stick to the plasma membrane and elevate lipid peroxidation and intracellular oxidative stress under radiation. When tested *in vivo*, GNWs led to improved tumor suppression by RT relative to GNSs. GNWs may be gradually reduced to form GNSs and shorter gold nanowires, which benefits repeated radiation. Our studies suggest that GNWs are as a promising type of radiosensitizer, which can be safely injected into tumors to enhance radiotherapy. While the current study was conducted in breast cancer models, the approach can be extended to the treatment of other cancers.

2.1 Introduction

External radiotherapy (RT) remains a mainstay cancer treatment method. Radiotherapy exploits ionizing radiation such as X-rays to damage DNA and lipids, eventually causing cancer cell death.[89, 90] However, the amount of radiation one can receive is limited by normal tissue exposure and the toxicity it may cause.[91] To improve tumor control at a given radiation dose, radiation modifiers are often used.[92] One promising type of radiosensitizer is heavy-metal or high-Z nanoparticles.[93] Possessing high atomic number elements and large mass energy coefficients, heavy-metal nanoparticles can enhance local photoelectric interactions and Auger effects, leading to elevated energy deposition and improved RT outcomes.[94-97] A common approach is to directly administer high-Z nanoparticles into tumors to boost RT efficacy. One example is hafnium oxide nanoparticles, which are being tested in the clinic for soft tissue sarcoma and head and neck cancer.[98-100] Another widely explored high-Z element is gold.[101, 102] A number of groups have reported on radiosensitizing effects of gold nanoparticles under both kV and MV beams.[103, 104] So far, most of the studies are performed with spherical gold nanoparticles,[104, 105] although gold nanorods[106-108] and nanospikes[107] have also been tested.

Herein we investigate gold nanowires (GNWs) as a novel type of high-Z radiosensitizer (**Scheme 1**). Briefly, we synthesized GNWs through a reverse micelle reaction and coated them with a layer of positively charged phospholipid, (1,2-distearoyl-sn-glycero-3-phosphoethanolamine-N-[amino(polyethylene glycol)-2000]), or DSPE-PEG (2000) Amine. The resulting GNWs possess a small diameter and a length of 1-3 μm. We assessed whether GNWs could enhance radiotherapy *in vitro* and *in vivo* and compared the results with gold nanospheres (GNSs). Our results suggest that GNWs afford superior radiosensitizing effects to GNSs, with much of the damage attributable to their ability to enhance lipid peroxidation. We also found that GNWs can be slowly reduced by glutathione to form smaller particles or truncated nanowires. This potentially provides a mechanism for sustained release of gold nanoparticles, benefiting RT that often involves multiple radiation sessions. To the best of our knowledge, GNWs have rarely been explored for bio-applications, and have never been investigated for radiation therapy.

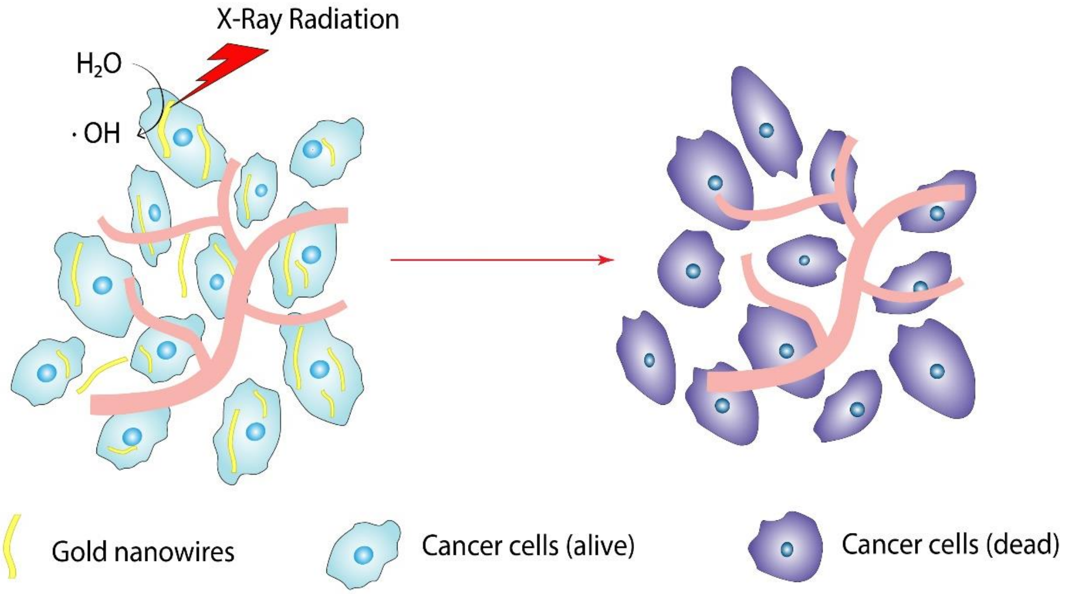

Figure 2.1 Schematic illustration of GNW-based radiosensitizing effects that enhance RT.

2.2 Material and method

Materials

Gold chloride trihydrate ($HAuCl_4 \cdot 3H_2O$, ≥99.9%, Sigma), tri-isopropylsilane ($C_9H_{22}Si$, 98%, Sigma), L-Glutathione reduced ($C_{10}H_{17}N_3O_6S$, ≥98.0%, Sigma), hexane (C_6H_{14}, ≥99%, Sigma), oleylamine ($C_{18}H_{35}NH_2$, technical grade, 70%, Sigma), toluene (C_7H_8, anhydrous, 99.8%, Sigma), Methylene blue ($C_{16}H_{18}ClN_3S \cdot xH_2O$, powder, ≥82%, Sigma) were purchased from Sigma-Aldrich. The other chemicals include chloroform ($CHCl_3$, ≥99.8%, Fisher Scientific), 3’-(p-aminophenyl) fluorescein (APF, Life Technologies), Singlet Oxygen Sensor Green (SOSG, Life

Technologies), Superoxide dismutase assay kit (SOD, Cayman Chemical), Phosphate Buffer saline (PBS, pH 7.2), Milli-Q Water (H_2O, 18.2 MΩ.cm@25℃), ATPlite 1step kit (ATP, PerkinElmer), TBARs assay kit (TBARs, Cayman Chemical).

Synthesis of gold nanowires (GNWs)

The gold nanowires were synthesized according to a published protocol with modifications.[109] Briefly, 22 mg $HAuCl_4{\cdot}3H_2O$ was mixed with 0.738 mL of oleylamine and 20 mL of hexane. The solution was vigorously stirred at room temperature until a homogeneous solution was formed. 1.03 mL of triisopropylsilane was then added into the solution and mild stirring was applied. The final solution was kept still at room temperature for 12 hours. Gold nanowires were collected by centrifugation at 6,000 rpm for 20 minutes and repeatedly wash with a toluene/ethanol 1:1 volume ratio mixture. The final product can be store in 10 mL of toluene or hexane.

Synthesis of gold nanospheres (GNSs)

Gold nanospheres were synthesized according to a published protocol.[110] Typically, 0.2318 g $HAuCl_4{\cdot}3H_2O$ was mixed with 2 mL hexane and 10 mL oleylamine in a 50 mL flask. The solution was kept at 80 °C under vigorous stirring and N_2 gas was applied to evaporate extra hexane. After 5 minutes, the stirring was stopped and the solution kept still at 80 °C for 5 hours. Nanospheres can be collected by adding 10 mL ethanol and centrifuge at 7,000 rpm for 5 minutes. The final product was washed three times with ethanol, and finally stored in 10 mL hexane.

Lipid coating of gold nanoparticles

The as-synthesized GNWs or GNSs were coated with a layer of PEGylated phospholipid. Typically, 200 µL of GNWs or GNSs solution was diluted with 5 mL hexane. 160 µL of DSPE-PEG(2000) Amine in chloroform (1 mg/mL) was then added into the solution. The solution was stirred at room temperature for half an hour. Then the solvent was removed by rotorvap. Milli-Q Water or PBS was finally added to the vessel to redisperse the lipid coated gold nanoparticles.

Characterizations of gold nanoparticles

The hydrodynamic size and surface charge of the particles were characterized by DLS and Z-potential. The morphology and EDS element mapping of nanoparticles were assessed by both Scanning Electron Microscope (SEM, FEI Teneo) equipped with a EDAX EDS system and Transmission Electron Microscope (TEM, FEI Tecnai20, 200 kV).

Cell culture

4T1 breast cancer cells were used for *in vitro* and *in vivo* studies. Cells were grown in RPMI1640 medium supplemented with 10% FBS and 100 units/mL of penicillin (ATCC). The cells were maintained in a humidified, 5% carbon dioxide (CO_2) atmosphere at 37 °C.

Cell viability

Cell viability was evaluated by ATP assay with 4T1 cells. Briefly, 4T1 cells with an initial density of 5,000 cells/well were seeded in a 96-well plate. After 24 h's inoculation, the incubation medium was aspirated and replaced with RPMI solutions containing different concentrations of GNWs or GNSs. After another 24 h's incubation, incubation medium was aspirated. 50 µL ATPlite 1 step substrate solution was mixed with 50 µL RPMI medium and the mixture was added into each well. The plate was sealed and mixed for 10 minutes at room temperature before test. Luminescence signals were measured using a microreader (Biotek). Average luminescence intensity was computed and compared. For treatment with nanoparticles+X-ray, 4T1 cells with an initial density of 5,000 cells/well were incubated in 96-well plates. 24 hours after the inoculation, cell medium was replaced with 100 µL RPMI medium solutions containing GNWs or GNSs. 5Gy X-ray radiation was applied 24 hours after the incubation. 24 h after the irradiation, cell medium was replaced with a mixture of 50 µL of ATPlite 1 step substrate solution and 50 µL RPMI. The plate was sealed and mixed for 10 minutes at room temperature before test. Luminescent signals were measured on a microreader (Biotek). Average luminescence intensity was computed and compared.

Singlet oxygen quantification by SOSG assay

SOSG assay was performed by following vendor's protocol (ThermoFisher). Typically, 100 µg SOSG was dissolved in 33 µL methanol to make a 5 mM stock solution. The solution was diluted with Milli-Q water to 5µM test solution before use. 4T1 cells were incubated in 96-well plates with an initial density of 5,000 cells/well. 50 µg/mL in 100 µL incubation medium was added after 24 h's inoculation. After another 24 h's of incubation, 5 Gy X-ray radiation was applied. Immediately after irradiation, cell medium was aspirated and replaced with 100 µL RPMI containing 5 µM SOSG. The plate was kept in the dark at room temperature. Fluorescence signals were measured on a microreader (Biotek). Excitation/emission wavelength were set at 504/525 nm. Similar protocol was used for SOSG studies with nanoparticle solutions.

SOD assay

SOD activity was assessed by following the vendor's protocol (Cayman Chemical). Assay buffer, sample buffer, radical detector, SOD standard, and Xanthine oxidase were from the vendor. 4T1 cells were incubated in 96-well plates with an initial density of 5,000 cells/well. 100 µL medium containing 50 µg·Au/mL GNWs or GNSs were incubated with the cells for 24 h. 5 Gy X-ray radiation was applied. Immediately after irradiation, medium was aspired and cells rinsed with sample buffer. 200 µL diluted Radical Detector was mixed with 10 µL sample buffer solution and added to each well. Reaction was initiated with 20 µL Xanithine Oxidase solution and the 96-well plate was kept in dark at room temperature and shaken for 10 minutes before test. For standards, the provided standard solution was diluted with sample buffer and 10 μL diluted sample buffer solution was mixed with 200 μL diluted Radical Detector and 20 μL diluted Xanthine Oxidase. Signals were measured on a microreader (Biotek). Absorbance at 450 nm was measured and compared to a standard curve.

Hydroxyl radicals in solutions

Hydroxyl radical generation was characterized by APF radical assay according to a vendor's protocol (ThermoFisher). A 20 μL 5mM stock APF solution was diluted with PBS to make a 2 μM testing solution before test. 100 μL testing solution containing GNWs or GNSswas were exposed to 5 Gy X-ray radiation and kept in the dark for 30 min. The resulting solution was finally diluted with same amount of fresh PBS and the fluorescence (490/515 nm) was measured on a microreader (Biotek).

Lipid peroxidation

TBARs assay kit was used to detect malondialdehyde (MDA), a product of lipid peroxidation. 4T1 cells were incubated in 96-well plates with an initial density of 5,000 cells/well for 24 h. After that 100 μL medium containing 50 μg·Au/mL GNWs or GNSs were incubated with the cells for another 24 h. After incubation with nanoparticles cells were irradiated with X-ray with dose of 5 Gy. Immediately after irradiation, the medium was aspirated and cells were rinsed with PBS buffer. Cells were homogenized on ice and the protein was collected and determined by BCA method. In each sample, equal amount protein was mixed with TBARs reagents (50 μL sodium dodecyl sulfate (SDS) solution and 2 mL color reagent) and samples vials were then placed in boiling water for one hour. After the reaction, the vails were placed immediately in ice bath for 10 minutes to stop the reaction. After 10 minutes, the vials were centrifuged for 15 minutes at 1,600 g, 4 °C. 150 μL of the solution was then transferred into a new 96-well plate and data were collected by reading the absorbance at 530 nm and emission at 550 nm with the help of a microplate reader (Biotek).

In vivo study

Animal studied were performed according to a protocol approved by the Institutional Animal Care and Use Committee (IACUC) of the University of Georgia. The animals were maintained under pathogen-free conditions. 4T-1 tumor model was generated by subcutaneously injecting 2×10^5 cells in 50 μL PBS into the right flank of 5-6 week old female BALB/c mice (Charles River). All the mice were randomly divided into 3 groups (n = 5). When the average tumor volume was about 100 mm^3, 70 μL GNWs or GNSs in PBS (1.0 mg/mL) were intratumorally injected into the mice on Day 0. The injection was performed at five sites of the tumor to ensure good coverage. Three doses of irradiation (3 Gy ×3) through an X-RAD 320 system to tumors on Day 0 (1 h after injection), 1 and 2. PBS treated group with or without radiation was used as control. The tumor size and body weight were inspected every 3 days. The tumor was measured in two dimensions with a caliper, and the tumor volume was estimated as $(\text{length})\times(\text{width})^2/2$. After 28 days, animals were euthanized and the tumor were dissected into slices for H&E staining.

Statistical analysis

For *in vitro* study, all measurements were performed at least three times. Measured values were presented as mean ± SD. One tailed Student's *t* test was used for comparison among groups, with *P* values of 0.05 or less representing statistical significance.

2.3 Result and discussion

Result

We synthesized GNWs following a published protocol with modifications.[109] Briefly, we dissolved $HAuCl_4$ along with oleylamine in hexane. The solution was vigorously stirred, and into the solution tri-isopropylsilane was added. After 12 h, we collected GNWs by centrifugation. Transmission electron microscopy (TEM) found that the as-synthesized GNWs had a diameter of ~4 nm and a length of 1-3 µm (**Figure 1a&b**). GNWs tend to form bundles when deposited onto a substrate and the solvent was removed. This was visualized by both TEM and scanning transmission electron microscopy (STEM) (**Figure 1b&c**). Energy Dispersive Spectroscopy (EDS) elemental analysis confirmed that the nanowires were made of gold (**Figure 1d**). Dynamic light scattering (DLS) showed the hydrodynamic size of GNWs in hexane was 3.6 nm (**Figure 2a**). This agrees well with individual nanowire diameter (**Figure 1a&b**).

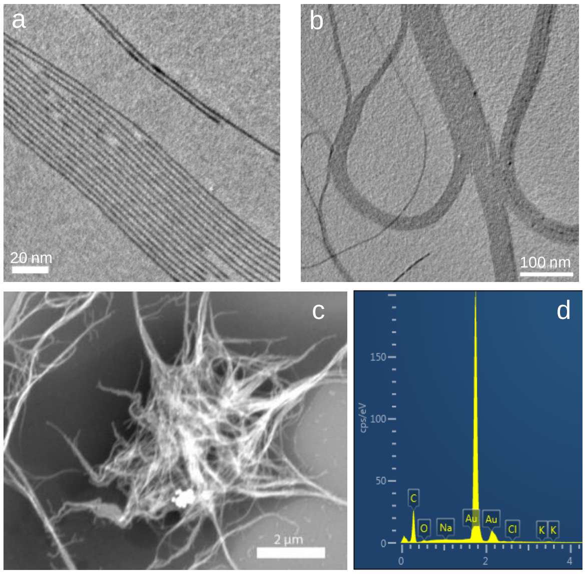

Figure 2.2 a,b) TEM image of GNWs. The long GNWs tend to form bundles when deposited onto a substrate. c) SEM image of GNWs, scale bar 2 µm. d) EDS spectrum of GNWs. Au is the main element in the nanostructure.

The as-synthesized GNWs were coated with a layer of oleylamine and the surface was hydrophobic. These GNWs can be dispersed in non-polar solvents like hexane and chloroform but cannot be dispersed in water. To render these GNWs dispersible in aqueous solutions, we coated GNWs with PEGylated phospholipid. This was achieved by mixing GNWs and DSPE-PEG (2000) Amine in chloroform and then removing the solvent on a rotary evaporator. The amphiphilic DSPE-PEG (2000) Amine was imparted onto GNWs through hydrophobic-hydrophobic interaction, with the PEG chains sticking outward to interact with water molecules. Adding water or phosphate-buffered saline (PBS) to the vessel readily redispersed the GNWs. The resulting, lipid coated GNWs was 45 nm in diameter (**Figure 2b**) with a positive surface charge of +31.1 mV (**Figure 2c**). The resulting aqueous solution was stable with a wine-like hue that is similar to spherical gold nanoparticles (**Figure 2d**). For comparison, we also synthesized GNSs,[110] and coated the GNSs with DSPE-PEG(2000) Amine (**Figure 2d**). The resulting GNSs have a core size of 14 nm (**Figure 2e**) and a similar positive surface charge of +37.1 mV (**Figure 2f**).

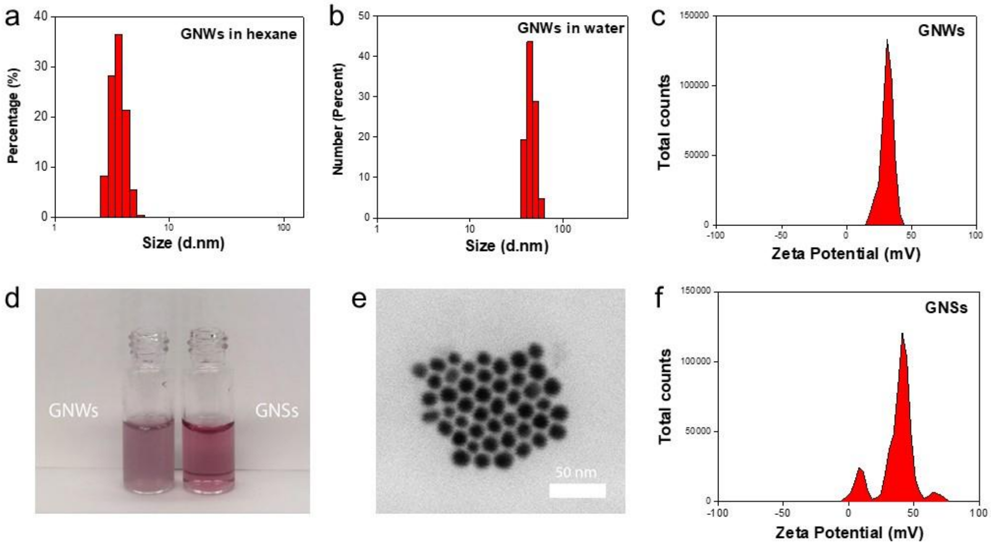

Figure 2.3 a) DLS of GNWs in hexane. b) DLS of phospholipid coated GNWs in water. c) Zeta potential of phospholipid coated GNWs in water. d) Photos of GNWs and GNSs dispersed in

water. e) TEM image of GNSs, scale bar 50 nm. f) Zeta potential of phospholipid coated GNSs in water.

We then analyzed the cytotoxicity of GNWs and GNSs using ATPlite viability assay in the absence of radiation. We incubated GNWs or GNSs with 4T1 cells at different concentrations (3.1-500.0 μg/mL, gold concentration). After 24 h incubation, the cells were washed, incubated with an ATPlite solution for 10 min, and the luminescent signals were analyzed on a microplate reader. For both GNWs and GNSs, the toxicity was low when the concentration was below 50 μg·Au/mL (**Figure 3a**), where the cell viability remained above 80%. Interestingly, GNSs induced a significant cell viability drop when their concentration was above 100 μg/mL, while GNWs showing greater biocompatibility (**Figure 3a**). This toxicity of positively charged gold nanoparticles at high concentrations was observed by others.[111-113]

We next examined the efficacy of GNWs as radiosensitizers. We first tested radical generation in PBS solutions of GNWs or GNSs (50 μg/mL Au/mL) with and without irradiation (5 Gy, the same below). This was assessed with aminophenyl fluorescein (APF), a florigenic sensor specific to hydroxyl radicals. APF radical assay showed that GNWs increased hydroxyl radical production by 20.8% (**Figure 3b**), relative to that of 2.7% for GNSs (**Figure 3b**). This is likely attributed to the relative large surface area of the thin nanowires.

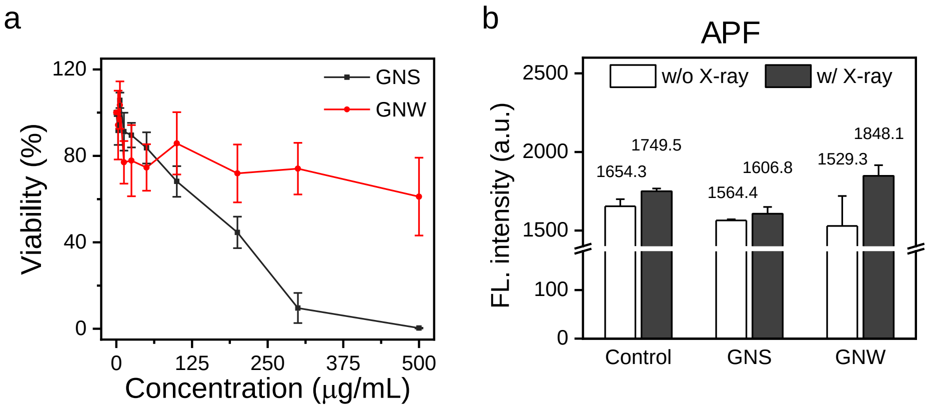

Figure 2.4 a) Cytotoxicity of GNWs and GNSs in the absence of radiation, measured by ATP assay at 24 h. 4T1 cells were incubated with GNWs and GNSs at different concentrations (3.125–500 μg·Au/mL) for 24 h. PBS treated cells were studied as a control. b) Hydroxyl radical generation under RT in the presence of GNWs or GNSs (50 μg/mL), measured by APF radical assay.

We then assessed the impact of GNWs+RT on intracellular radical levels. This was assessed with Singlet Oxygen Sensor Green (SOSG) assays in 4T1 cells, a breast cancer cell line. Our results showed that X-ray alone increased $^1O_2$ level by 62.9% relative to the control (**Figure 4a**). In the presence of GNSs and GNWs, the $^1O_2$ levels were further elevated, showing an increase of 107.4 and 126.6%, respectively, relative to control cells. We also next assessed the impact of this radical enhancement to cellular oxidative stress (**Figure 4b**). GNWs plus radiation (5 Gy) drastically elevated cellular superoxide dismutase (SOD) activity to 0.244 U/mL, compared to 0.119 U/mL for RT only. As a comparison, GNSs plus X-ray did not significantly increase the SOD level compared to the radiation only group (0.092 U/mL). The increase in oxidative stress was also confirmed by thiobarbituric acid reactive substances assay or TBRAS assay (**Figure 4c**), which measures the level of lipid oxidation. Specifically, untreated 4T1 cells showed a malondialdehyde (MDA) level of 2.63 µM. This number barely changed when cells were incubated with GNWs or GNSs (2.83 and 2.65 µM, respectively). GNSs+RT led to a small increase of MDA level relative to RT alone (3.17 and 2.83 µM, respectively). Much greater lipid oxidation was observed when GNWs were used in combination with RT, in which case the MDA level was elevated to 6.81 µM.

Subsequently, we assessed how GNWs would facilitate RT induced toxicity. This was evaluated in 4T1 cells using ATPlite assay (**Figure 4d**). Briefly, we incubated 4T1 cells with either GNWs or GNSs at 50 µg·Au/mL for 24 h. According to cytotoxicity studies in the absence of irradiation (**Figure 3a**), neither GNWs nor GNSs would not cause severe toxicity at this concentration. We then applied 5 Gy radiation to the cells, and conducted ATPlite assay 24 h later. We found enhanced toxicity for both nanomaterials (**Figure 4d**). Specifically, while RT alone had minimal impact of cell viability at 24 h, GNSs+RT and GNWs+RT reduced the viability to 59.6% and 63.5%, respectively, relative to the control.

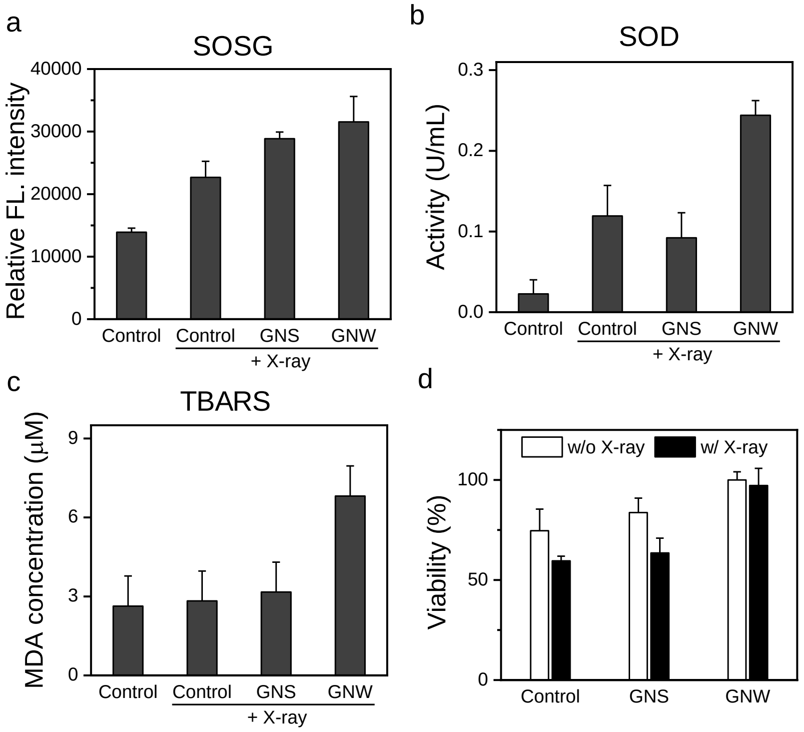

Figure 2.5 a) SOSG assay, b) SOD assay, and c) TBARS assay with 4T1 cells after they were incubated with GNWs or GNSs (50 μg/mL) and then irradiated (5 Gy). d) Cytotoxicity of GNWs+RT and GNSs+RT (50 μg·Au/mL, 5 Gy), assessed by ATP assay with 4T1 cells.

Lastly, we examined GNWs+RT *in vivo* in 4T1 subcutaneous tumor models. Briefly, we inoculated 2×10^5 4T1 cells to the right flank of BALB/c mice. When tumor size reached ~ 100 mm^3, we intratumorally (i.t.) injected GNWs or GNSs (1 mg·Au/mL in 70 µL PBS) into the mice (n=5). We then delivered three doses of irradiation (3 Gy × 3) through an X-RAD 320 system to tumors on Day 0, 1 and 2, with the rest of the animal body lead-shielded. For controls, PBS was i.t. injected. GNWs+RT efficiently slowed down tumor growth, leading to a tumor inhibition rate (TIR) of 212.5% on Day 22 (**Figure 5a**). This was superior to GNSs+RT, which showed a TIR value of 35.7% ($P < 0.05$, **Figure 5a**). We euthanized the animals on Day 22 and harvested tumors for H&E staining (**Figure 5c**). The staining results overall corroborate with the tumor growth, with the GNWs+RT group showing a significantly reduced cancer cell population in tumors. Meanwhile, in both treatment groups, we observed no sign of acute toxicity. No weight loss was observed during the whole experiment (**Figure 5b**).

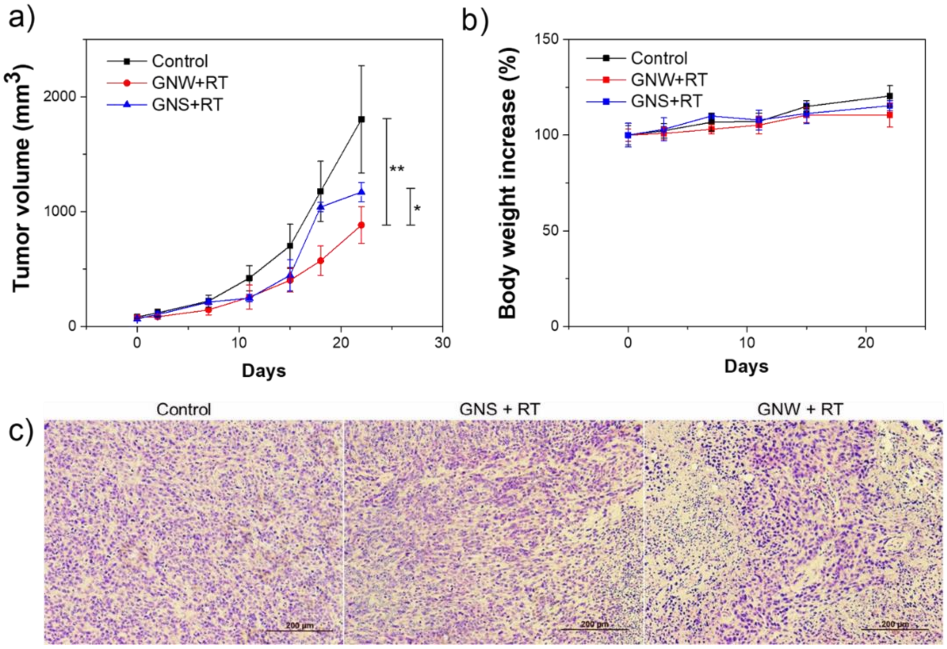

Figure 2.6 *In vivo* RT studies with GNWs or GNSs. a) Tumor growth curves. 4T1 bearing mice were i.t. injected with GNWs or GNSs (1 mg/mL in 70 μL PBS). PBS alone was studied as a control. *, P<0.05; **, P<0.01. b) Tumor growth curves. c) H&E staining of tumor tissues taken from treated animals.

Discussion

In this study, we investigated the potential of GNWs as a radiosensitizer, which, to the best of our knowledge, is the first time. Compared with GNSs, we observed increased production of radicals under radiation in solutions. This is attributed to the relative large surface area of GNWs. While GNWs may be too long for direct cell uptake, our studies found that GNWs are superior to GNS with regard to enhancing cellular oxidative stress under radiation. This is likely attributable to cell-surface-bound GNWs that cause elevated lipid damage under radiation. This hypothesis was supported by TBARS assay results.

In a separate study, we tested the stability of GNWs in solutions. We added into the incubation medium glutathione (1 mM), a thiol-containing reducing agent that is abundant in extracellular milieu. After the incubation, we examined the absorbance at 530 nm, which is the characteristic absorbance of GNSs. Our studies showed that 530-nm absorbance, which was characteristic of surface plasmon resonance peak, was increased over time. This indicates gradual degradation of GNWs, which results in the formation of shorter nanowires or GNSs. This hypothesis was supported by TEM analysis, finding GNWs with reduced lengths and increasing number of particles over incubation. Unlike small GNSs that may be quickly cleared from tumor areas after injection, GNWs, with their long length, may well retain in tumors after injection and serve as a reservoir for GNSs. Considering that repeated radiations are often adopted in clinical RT, the slow degradation of GNWs is considered an advantage.

It is also possible to combine GNWs with small molecule therapeutics to further enhance RT. For instance, the di-layered lipid layer on GNWs can be inserted with small molecule radiosensitizers, such as 5-FU and paclitaxel. In that case, GNWs can also serve as a platform to release small molecule agents, which can synergize with gold-based radiosensitizing to achieve maximum therapy results. There have been extensive reports on gold nanostructures' ability to absorb radio frequency[114, 115] or visible/near-infrared light[116, 117] and convert the energy to heat. It is possible to exploit GNWs as a transducer to mediate radio frequency or photothermal therapy, along with RT. These possibilities will be evaluated in future studies.

2.4 Conclusion

Overall, our studies suggest the potential of GNWs as a novel type of radiosensitizer. Compared to GNSs, GNWs showed lower toxicity in the absence of radiation but higher efficiency to enhance radiotherapy. While the current study is performed in breast cancer models, the approach can be potentially extended to the treatment of other cancer types such as brain, prostate, and head and neck cancer.

CHAPTER 3

X-RAY INDUCED RADIATION THERAPY WITH CsI(Na)@MgO NANOPARTICLES AND 5-AMINOLEVULINIC ACID[2]

---

[2] Reprinted with permission from Fangchao Jiang, Chaebin Lee, Weizhong Zhang, Wen Jiang, Zhengwei Cao, Harrison Byron Chong, Wei Yang, Shuyue Zhan, Jianwen Li, Yong Teng, Zibo Li, Jin Xie. Accepted by Journal of Nanobiotechnology. 2022, 20, 330.

ABSTRACT

X-ray induced photodynamic therapy (X-PDT) holds the potential to overcome the shallow tissue penetration issue associated with conventional photodynamic therapy (PDT). To this end, complex and sometimes toxic scintillator-photosensitizer nanoconjugates are often used, posing barriers for large-scale manufacturing and regulatory approval. Herein, we report a streamlined X-PDT strategy based on CsI(Na)@MgO nanoparticles and 5-aminolevulinic acid (5-ALA). 5-ALA is a clinically approved photosensitizer, converted to protoporphyrin IX (PpIX) in cancer cells' mitochondria. CsI(Na)@MgO nanoparticles produce strong ~410 nm X-ray luminescence, which matches the Soret band of PpIX. We hypothesize that the CsI(Na)@MgO-and-5-ALA combination can mediate X-PDT wherein mitochondria-targeted PDT synergizes with DNA-targeted irradiation for cancer cell killing. Because scintillator nanoparticles and photosensitizer are administered separately, the approach forgoes issues such as self-quenching or uncontrolled release of photosensitizers. When tested *in vitro* with 4T1 cells, the CsI(Na)@MgO and 5-ALA combination elevated radiation-induced reactive oxygen species (ROS), enhancing damages to mitochondria, DNA, and lipids, eventually reducing cell proliferation and clonogenicity. When tested *in vivo* in 4T1 models, X-PDT with the CsI(Na)@MgO and 5-ALA combination significantly improved tumor suppression and animal survival relative to radiation therapy (RT) alone. After treatment, the scintillator nanoparticles, made of low-toxic alkali and halide elements, were efficiently excreted, causing no detectable harm to the hosts. Overall, separately administering CsI(Na)@MgO nanoparticles and 5-ALA represents a safe and streamlined X-PDT approach with a potential in clinical translation.

3.1 Introduction

PDT is an emerging cancer treatment modality.[1, 2] During PDT, a photosensitizer (PS, both singular and plural)[3-5] molecule is activated by light to produce ROS, most importantly singlet oxygen ($^1O_2$), which cause cancer cell death.[6-8] Light and PS need to be colocalized to mediate toxicity, rendering PDT innately selective. PDT can be delivered repeatedly without incurring resistance to therapy, and can be combined with both chemotherapies and immunotherapies for enhanced efficacy.[9-12] Despite these merits, PDT has not yet been accepted as a mainstream cancer treatment option. One major caveat is that light cannot deeply penetrate biological tissues, precluding PDT from treatment of large and/or multifocal, deep-seated tumors.[13] To address the issue, others and us have developed a modality known as X-ray induced radiation therapy (X-PDT).[14-17] X-PDT is often mediated with a scintillator-PS nanoconjugate,[18-20] in which the scintillator down-converts X-ray photons to visible photons that activate the PS.[21] Leveraging the excellent tissue penetration of X-rays, X-PDT offers a solution to the restricted tissue penetration problem.

Multiple nanoplatforms have been tested for X-PDT.[22-31] For instance, Chen *et al.* demonstrated that LaF_3:Tb, ZnS:Cu,Co, and copper-cysteamine nanoparticles can mediate X-PDT.[24-26] Lin *et al.* synthesized a series of metal-organic frameworks and confirmed their ability to enhance cancer cell killing under radiation;[29-31] one formulation, RiMO-301, is being investigated in the clinic.[32] We have prepared $SrAl_2O_4:Eu^{2+}$-MC540 and $LiGa_5O_8:Cr^{3+}$-2,3-naphthalocyanine nanoparticle conjugates[22, 23] and confirmed their radiosensitizing efficacy.[14, 22, 23] However, PS may experience self-quenching or pre-mature release in these nanoconjugates, limiting activation efficacy. Some scintillator nanoparticles are made from top-down approaches, which are associated with relatively large batch-to-batch variations. Furthermore, scintillators often contain toxic transition or lanthanide elements, and their long-term side effects remain to be fully investigated. Overall, these issues pose as barriers for large-scale manufacturing and regulatory approval of the technologies.

Herein we explore a streamlined X-PDT strategy based on CsI(Na)@MgO nanoparticles and 5-aminolevulinic acid (5-ALA). Cesium iodides such as CsI(Na) are established scintillation materials with high light outputs (e.g. 42,000 photons/MeV for CsI(Na)).[33] The emission of CsI(Na) perfectly matches the absorbance of PpIX, a biosynthetic product of 5-ALA.[34] Owing to the Warburg effect, cancer cells downregulate ferrochelatase, an enzyme that incorporates Fe^{2+} into PpIX in the final step of heme synthesis,[35] resulting in selective accumulation of PpIX in cancer cells' mitochondria.[36] This tumor targeting ability has motivated the use of 5-ALA as either a PS[37-39] or an imaging agent[40] in the clinic. We postulate that, when irradiated, CsI(Na) nanoparticles can activate 5-ALA-induced PpIX, causing cancer cell death. Of note, clinical 5-ALA PDT employs red light to activate the 630-nm Q-band of PpIX, which has relatively low absorptivity. This compromise is necessary because shorter wavelength photons would be largely scattered by the skin or absorbed by pigments such as melanins. In the current approach, the light source, *i.e.* CsI(Na) nanoparticles, are delivered into cancer cells and illuminate therein, minimizing light attenuation. The ~410 nm luminescence from CsI(Na) activates the Soret band of PpIX, which absorbs at least one order of magnitude more strongly than the 630-nm Q-band, potentially improving efficacy. Cesium iodide is highly water soluble, so we coat CsI(Na) nanoparticles with a layer of MgO to prevent fast degradation. We also impart DSPE-PEG-Folate to nanoparticle surface to render them with good colloidal stability and tumor targeting ability.

The current X-PDT strategy affords several benefits. First, there is no need to load PS onto CsI(Na)@MgO nanoparticles, forgoing issues such as self-quenching among PS molecules and uncontrolled release of them. CsI(Na)@MgO nanoparticles are synthesized through wet chemistry with excellent reproducibility and scalability. Second, CsI(Na) nanoparticles comprise no transition and lanthanide elements. After treatment, the nanoparticles are degraded to low-toxic alkali and halogen ions, which are safely excreted from the hosts. Third, the PDT component specifically targets mitochondria, which are 5-10 times more susceptible to PDT than plasma membrane and endosomes/lysosomes[41, 42] that are common targets of previous X-PDT nanoplatforms. We expect the mitochondria-targeted component to synergize with the DNA-target RT, improving cancer cell killing (Scheme 1). We evaluated the efficacy of the approach first *in vitro* with 4T1 cells and then *in vivo* in 4T1 mouse models.

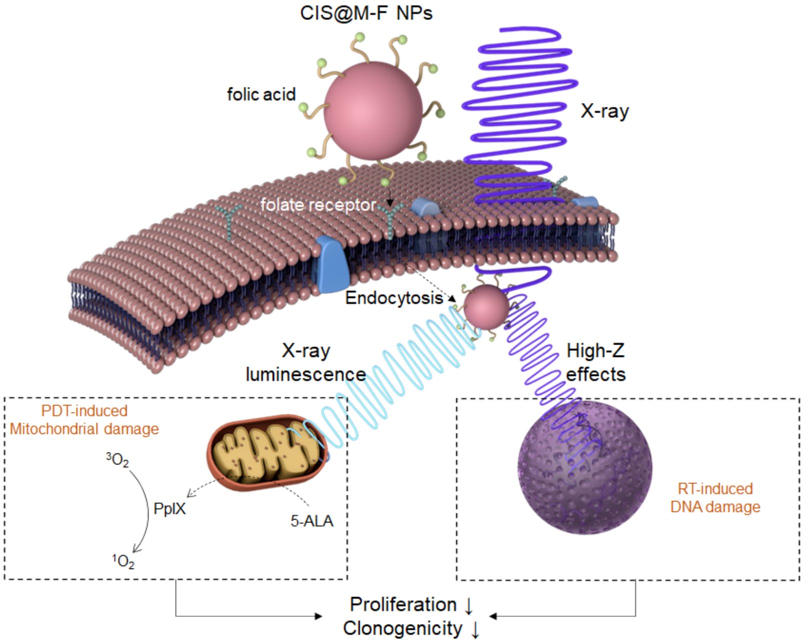

Scheme 1. CsI(Na)@MgO@DSPE-Folate nanoparticles (CIS@M-F) and 5-ALA are separately administered but colocalized in cancer cells to enable X-PDT. CIS@M-F are internalized by

cancer cells through receptor-mediated endocytosis. 5-ALA is converted to PpIX, which accumulates in cancer cells' mitochondria. When irradiated, CIS@M-F produce X-ray luminescence that activates PpIX, causing mitochondria damage. Meanwhile, CIS@M-F also afford high-Z effects that enhance RT-induced DNA damage. The two components synergize to reduce cancer cell proliferation and tumorigenicity.

3.2 Materials and Methods

Materials

Cs_2CO_3 (99%, Sigma, Cat#441902), I_2 (≥99.8%, Sigma, Cat#207772), NaI (≥99.5%, Sigma, Cat#383112), magnesium acetylacetonate dihydrate, ($Mg(acac)_2$, 98%, Sigma, Cat#129577), 1-Octadecene ($C_{18}H_{36}$, technical grade, 90%, Sigma, Cat#0806), oleic acid ($C_{18}H_{34}O_2$, technical grade, 90%, Sigma, Cat#364525), oleylamine ($C_{18}H_{35}NH_2$, technical grade, 70%, Sigma, Cat#07805), 1,2-tetradecanediol (technical grade, 90%, Sigma, Cat#260290), 1,2-hexadecanediol (technical grade, 90%, Sigma, Cat#213748), hexane (C_6H_{14}, ≥99%, Sigma, Cat#139386), ethanol (anhydrous, Sigma, Cat#443611), benzyl ether (98%, Sigma, Cat#108014), chloroform ($CHCl_3$, ≥99.8%, Fisher Scientific), 1,2-dipalmitoyl-sn-glycero-3-phosphoethanolamine-N-(lissamine rhodamine B sulfonyl) (ammonium salt) (16:0 Liss Rhod PE) (Avanti, Cat#810158), 1,2-distearoyl-sn-glycero-3-phosphoethanolamine-N-[carboxy(polyethylene glycol)-2000] (sodium salt) (DSPE-PEG(2000) Carboxylic Acid) (Avanti, Cat#880135), 1,2-distearoyl-sn-glycero-3-phosphoethanolamine-N-[folate(polyethylene glycol)-2000] (ammonium salt) DSPE-PEG(2000) Folate (Avanti, Cat#880124), methylene blue ($C_{16}H_{18}ClN_3S \cdot xH_2O$, powder, ≥82%, Sigma), phosphate buffer saline (PBS, pH 7.2), Milli-Q Water (H_2O, 18.2 MΩ.cm@25℃).

Synthesis of CsI(Na) nanoparticles

0.203 g Cs_2CO_3 was mixed with 10 mL 1-octadecene and 1 mL oleic acid in a 100 mL flask. The solution was heated to 150 ℃ and maintained at this temperature for 30 mins with magnetic stirring. Next, 1 mL oleylamine, 0.02954 g 1,2-hexadecanediol, and 0.01 g NaI were added into the mixture. After reacting for 10 minutes, the solution was cooled to room temperature, and 0.3165 g I_2 were added. The flask was then sealed and stirred for another 3 hours. CsI nanoparticles were collected by centrifugation and washed with a 1:1 hexane and ethanol mixture 3 times.

Synthesis of CsI(Na)@MgO nanoparticles

In a typical reaction, 20 mg CsI(Na) nanoparticles in 5 mL hexane was mixed with 0.02 g $Mg(acac)_2$, 0.053 g 1,2-tetradecanediol, and 20 mL benzyl ether in a 100 mL three-neck flask. The solution was heated to 120 ℃ under Argon protection and maintained at this temperature for 20 min. The solution was further heated to 310 ℃ before the addition of 1 mL pre-heated oleic acid. The reaction continued for 10 min before being cooled to room temperature. The product was collected by centrifugation and washed with a 1:1 hexane and ethanol mixture 3 times.

Synthesis of CIS@M-F

20 mg CsI(Na)@MgO nanoparticles were dispersed in 2 mL chloroform. Into the solution, 75 µL of DSPE-PEG(2000)-COOH in chloroform (10 mg mL^{-1}) and 25 µL DSPE-PEG(2000)-Folate in chloroform (10 mg mL^{-1}) were added. The mixture was stirred at room temperature overnight, and the solvent was removed by rotary evaporation. The nanoparticles were dispersed in PBS and passed through a desalting column before use.

Synthesis of CIS@M-F or CIS@M-C with rhodamine B labelling

20 mg CsI(Na)@MgO nanoparticles were dispersed in 2 mL chloroform. Into the solution, 50 µL of DSPE-PEG(2000)-COOH in chloroform (10 mg mL^{-1}) and 25 µL DSPE-PEG(2000)-Folate in chloroform (10 mg mL^{-1}) together with 25 µL of 16:0 Liss Rhod PE in chloroform (10 mg mL^{-1}) were added. The mixture was stirred at room temperature overnight, and the solvent was removed by rotary evaporation. The nanoparticles were dispersed in PBS and passed through a desalting column before use.

Nanoparticle characterizations

Nanoparticle crystallinity was assessed using the Bruker D8-Advance X-ray diffraction (XRD) diffractometer with Cu Kα radiation ($\lambda = 1.5418$ Å) at a scanning rate of 10° min^{-1}. The hydrodynamic sizes and surface charges of the particles were characterized on a Malvern Zetasizer Nano ZS system. Nanoparticle size, morphology, and elemental analysis was characterized using a Scanning Electron Microscope (FE-SEM Thermo Fisher Teneo) which was equipped with an EDX system and Transmission Electron Microscope (FEI Tecnai20 and FEI Tecnai G2 F30 Hi-Res TEM). Nanoparticle composition was analyzed by Inductively Coupled Plasma Atomic Emission Spectroscopy using an Xseries II ICP/MS system (Thermo Electron Corporation). An iodide-selective electrode was used to conduct release experiments in PBS solutions of nanoparticles at room temperature (Mettler Toledo perfectION™).

Radical production

100 µL PBS control, 100 µg mL^{-1} CIS@M-F, 0.04 M PpIX, and 100 µg mL^{-1} CIS@M-F plus 0.04 M PpIX solutions were prepared, distributed into a 96-well plate, and irradiated with 5

Gy X-ray (X-RAD 320). 80 μL 1 μᴍ methylene blue was added to each well immediately following radiation, and the plate was shaken and kept in darkness at room temperature for 5 mins before testing. A UV-vis spectrometer was then used to record absorbances (664 nm).

Cell culturing

4T1 breast cancer cells were used for *in vitro* and *in vivo* studies. Cells were grown in RPMI1640 medium which was supplemented with 10% FBS and 100 units mL^{-1} of penicillin (ATCC). Cells were maintained in a humidified, 5% carbon dioxide (CO_2) atmosphere at 37 °C.

ATP viability assay to test nanoparticle and 5-ALA toxicity

The ATP viability assay was performed according to the manufacturer's protocol (PerkinElmer, ATPlite 1step Luminescence Assay Cat#6016736).[61] 4T1 cells were seeded at 5000 cells/well in a white 96-well plate. After 24 hours of incubation, CIS@M-F and 5-ALA (18.75, 37.5, 75, 150, 300, 600 μg mL^{-1} for CIS@M-F； 19.5, 78.1, 312.5, 1250 μg mL^{-1} for 5-ALA) were added to each well for another 24 hours of incubation. The ATP kit solution was then added to each well, and a 96-well microplate reader was used to measure total luminescence. Cell viability was calculated as a percentage of the luminescence of the untreated control.

ATP viability assay to test X-PDT efficacy

The ATP viability assay was performed according to the manufacturer's protocol (PerkinElmer, ATPlite 1step Luminescence Assay Cat#6016736). 4T1 cells were seeded at 5000 cells/well in a white 96-well plate and incubated for 24 hours before the addition of 20 μg 5-ALA to each well. Cells were incubated for 1 hour before the addition of 10 μg CIS@M-F. Cells were then incubated for 2 hours before being irradiated (5 Gy). The plate was returned to the incubator and maintained in darkness for 24 hours before the ATP luminescence test.

Intracellular PpIX analysis

PpIX extraction was performed according to a published protocol.[62] Cells were seeded in a 96-well plate at 5000 cells/well. After 24 hours of incubation, cells were trypsinized, harvested by centrifugation, and redispersed in 5% HCl at 37 ℃ for an hour. Following incubation in acid, the supernatant was collected and fluorescence signals (ex/em: 406/604 nm) were recorded.

APF assay

ROS (reactive oxygen species) were measured with the APF assay (Invitrogen™ Cat#A36003).[63] 4T1 cells were seeded in 96-well plates at 5000 cells/well. After 24 hours, nanoparticles in 100 µL RPMI medium or medium only were added to each well and incubated for 2 hours before being irradiated (5 Gy by X-Rad 320). Thereafter, the plate was incubated with 100 µL APF solution (2 µᴍ) for 30 mins at room temperature in the dark. Lastly, the medium was diluted with an equal volume of fresh PBS, and fluorescence signals (ex/em: 490/515 nm) were analyzed on a microplate reader (Biotek).

SOSG (singlet oxygen) assay

The SOSG assay was conducted following the vendor's protocol (Invitrogen™ Cat#S36002).[64] 4T1 cells were seeded in 96-well plates at 5000 cells/well. Following 24 hours of incubation, the medium was aspirated and 20 µL SOSG solution (5 µᴍ) with 100 µg mL^{-1} CIS@M-F in 100 µL medium were added to each well. After 1 hour, 20 µL 5-ALA (1 mg mL^{-1})

was added. 5 Gy radiation was delivered following another 2 hours of incubation. Fluorescence signals (ex/em: 504/525 nm) were recorded on a microplate reader (Biotek).

Cell uptake studies

Cell uptake of CIS@M-C and CIS@M-F nanoparticles were analyzed on a CytoFLEX flow cytometer. 4T1 cells were seeded at 0.5 × 10^6 cells/well into 6-well plates. Then, nanoparticles were incubated with cells at a final nanoparticle concentration of 100 μg mL^{-1}. Both CIS@M-F and CIS@M-C were labeled with Rhodamine B following a published protocol.[65] Following either 2 or 6 hours of incubation, cells were harvested for flow cytometer analysis, and the MFI was recorded.

SOD activity

SOD activity was assessed following the vendor's protocol (Cayman Chemical Cat#706002). 4T1 cells were seeded into 6-well plates at 1 million cells/well. After 24 hours, 2 mL RPMI medium containing 100 μg mL^{-1} CIS@M-F and 200 mL^{-1} 5-ALA were added to each well. 5 Gy X-ray irradiation was delivered after 4 hours. Immediately following irradiation cells were washed with PBS three times and collected with a rubber scraper. Cell pellets were subjected to differential centrifugation at 4°C and 12000 rpm for 20 mins to separate the mitochondrial and cytosolic fractions. Both the supernatant and mitochondrion were collected, aliquoted, sonicated and transferred into a 96-well plate. Test kit solution was added to each well, and the 96-well plate was shaken for 10 mins in the dark at room temperature before measurement. Absorbance (450 nm) was measured on a microplate reader (Biotek).

Lipid peroxidation

The Image-iT Lipid Peroxidation Kit (Invitrogen™ Cat#C10445) was used to assess lipid peroxidation. 4T1 cells were seeded into 96-well plates at 5000 cells/well. Following 24 hours of incubation, 200 µg mL^{-1} 5-ALA or 100 µg mL^{-1} CIS@M-F were added to each well. Following 4 hours of incubation, the plate was irradiated (5 Gy). The Image-iT Lipid Peroxidation dye was added to each well, and the plate was incubated at 37 °C and 5% CO_2 for 30 mins. Green (ex/em: 488/510 nm) fluorescence intensity was used to quantitate lipid peroxidation.

Caspase-3 activity

4T1 cells were incubated with CIS@M-F (100 µg mL^{-1}) and 5-ALA (200 µg mL^{-1}) for 2 hours prior to receiving 5 Gy X-ray irradiation. Control treatments included CIS@M-F, 5-ALA, or PBS. Following 24 hours of incubation, cells were stained with the FAM-FLICA® Caspase-3/7 kit (Immunochemistry, Cat# 94) following the manufacturer's protocol. The caspase-3 activity was evaluated by measuring fluorescence signals (ex/em: 488/530 nm) on a microplate reader (Synergy Mx, BioTeK).

Mitochondrial membrane potential ($\Delta\Psi_m$)

Mitochondrial potential was assessed using the TMRE staining kit following the vendor's protocol (Abcam Cat#ab113852). 4T1 cells were incubated with CIS@M-F (100 µg mL^{-1}) for 2 hours followed by 5-ALA (200 µg mL^{-1}) for 3 hours before receiving 5 Gy irradiation. Control treatments included CIS@M-F, 5-ALA, or PBS with or without irradiation. The medium was aspirated after 24 hours, and cells were incubated in TMRE staining solution for 15 min. Fluorescence signals (ex/em: 549/575 nm) were measured on a microplate reader.

γH2AX assay

DNA damage was evaluated using anti-rH2AX (Alexa 647 labeled) antibodies (Millipore Sigma, Cat# 07-164-AF647). Briefly, 4T1 cells were seeded onto a 4-well imaging chamber at a density of 10,000 cells/well and incubated for 24 hours. After washing, the cells were incubated with CIS@M-F (100 μg mL^{-1}) for 2 hours followed by 5-ALA (200 μg mL^{-1}) for 3 hours before receiving 5 Gy irradiation. Control treatments included CIS@M-F, 5-ALA, or PBS with or without irradiation. After 1 hr, cells were collected, fixed, permeabilized, and stained with anti-rH2AX antibodies following the vendor's protocol. Fluorescent images were acquired on a Zeiss LSM 710 confocal microscope. ImageJ was used to count the number of foci per cell.

Clonogenic assay

Clonogenic assays were performed using a modified protocol.[66] 4T1 cells were pre-seeded into 6-well plates. After 24 hours, cells were incubated with CIS@M-F (100 μg mL^{-1}) for 2 hours followed by 5-ALA (200 μg mL^{-1}) for 3 hours before receiving 0, 1, 3, 5, 7, and 9 Gy of radiation. Treated cells were trypsinized, replanted in petri dishes (100 *15 mm), and incubated at 37 °C with 5% CO_2. After 14 days, cells were rinsed carefully with PBS, fixed in 2-3 mL of 6.0% glutaraldehyde solutions, and treated with 1 mL of 0.5% crystal violet. After 10 mins, cells were rinsed with D.I. water and dried before colony counting. Colonies containing at least 50 stained cells were included in survival fraction (SF) calculations.

In vivo therapy studies

Animal studies were performed according to a protocol (A2020 06-004-R1) approved by the Institutional Animal Care and Use Committee (IACUC) of the University of Georgia. The animals were maintained under pathogen-free conditions. 4T1 tumors were established by subcutaneously injecting 2 × 10^5 cells in 50 μL PBS into the right flanks of 5-6-week old female BALB/c mice (Charles River). When tumor volume reached 50 mm^3, the animals were randomly divided into 6 groups (n = 5) and received the following treatments (Day 1): PBS plus ionizing radiation (PBS + IR), 5-ALA with irradiation (5-ALA + IR), CIS@M-F plus irradiation (CIS@M-F + IR), PBS only (PBS), CIS@M-F plus 5-ALA, no irradiation (CIS@M-F + 5-ALA), or CIS@M-F plus 5-ALA plus irradiation (CIS@M-F + 5-ALA + IR). 5-ALA (50 mg kg^{-1} in PBS) was administered intraperitoneally. CIS@M-F in PBS (1.25 mg kg^{-1}) were intratumorally injected 2 hours after the 5-ALA injection. A 320 KV cabinet irradiator (X-RAD 320, Precision X-ray, Inc.) was used to irradiate (3 Gy) tumors 1 hour after CIS@M-F administration, while the rest of the animal body was protected with lead. Animals underwent two additional treatment sessions on Days 3 and 5. Tumor size and body weight were inspected every 3 days. Tumor dimensions were measured with a caliper. Tumor volume was estimated by calculating $(\text{length})\times(\text{width})^2/2$. Animals were euthanized after 22 days. Tumors were dissected and sliced for H&E and Ki67 staining. Organs including the heart, spleen, liver, brain, intestine, kidney, and lung were also harvested for H&E staining.

Biodistribution studies

5-6 week-old female BALB/c mice (Charles River) were intravenously injected with CIS@M-F (50 μL, 1.25 mg kg^{-1}) or PBS (control) *via* the tail vein. All mice were sacrificed after two weeks. Blood was collected through cardiac puncture for complete blood count (CBC), BUN, and ALT measurements. Major organs, including the heart, spleen, liver, brain, intestine, kidney, and lung were harvested. Half of the tissues were weighted, homogenized, and digested in hot nitric acid. Supernatants were subjected to ICP-MS analysis to measure tissue concentrations of cesium and iodine in tissues (µg/grams of tissue). The remaining tissues were fixed and sliced for H&E staining.

Safety Statement

No unexpected or unusually high safety hazards were encountered

Statistical analysis

All quantitative data were shown as mean ± SD. Statistical analysis was conducted using student's *t* or ANOVA test. $*p < 0.05$, $**p < 0.01$, $***p < 0.001$.

3.3 Results and discussion

Synthesis and characterizations of CsI(Na) nanoparticles

We dissolved oleic acid and cesium carbonate in 1-octadecene and heated the solution to 150 ℃ (Figure 1a). We then added oleylamine, 1,2-hexadecanediol, and NaI into the mixture, followed by the addition of I_2. After reaction, we collected the products by centrifugation and redispersed them in hexane. The yield is ~90%. As-synthesized CsI(Na) nanoparticles were cubic (Figure 1b) with an average size of 55.2 ± 15.1 nm. Energy-dispersive X-ray spectroscopy (EDX) confirmed that the Cs-I molar ratio was ~ 1:1 (Figure S1a). Inductively coupled plasma mass spectrometry (ICP-MS) found that the Na dopant was ~1%. Selected area electron diffraction (SAED) revealed a diffraction pattern that matches bulk CsI (Figure S1b).[151] X-ray diffraction (XRD) also confirmed that the nanoparticles were CsI in composition and belonged to the Pm3m space group (No. 221, JCPDS#06-0311, Figure 1c).

CsI(Na) is hygroscopic. To prevent fast degradation, we imparted a layer of MgO onto CsI(Na) nanoparticles *via* seed-mediated growth.[152] We chose MgO because it is low-toxic, stable at neutral pH, and biodegradable.[153-157] The resulting CsI(Na)@MgO nanoparticles were spherical and possessed a ~25.0-nm-thick shell (Figure 1d&e, and Figure S1c). EDX confirmed the presence of Mg in the resulting nanoparticles, and that the Cs-I ratio remained at ~1:1 (Figure S1d). XRD identified characteristic CsI peaks but no MgO peaks (Figure 1c), indicating that the coating is amorphous. We also studied the X-ray luminescence of CsI(Na)@MgO nanoparticles. Both CsI(Na) and CsI(Na)@MgO nanoparticles displayed an intense luminescence peak at ~410 nm (Figure 1f), which agrees with the bulk material.[16] The luminescence peak overlapped well with the Soret band of PpIX (Figure 1f), suggesting the potential for activating the PS with luminescence from CsI(Na).

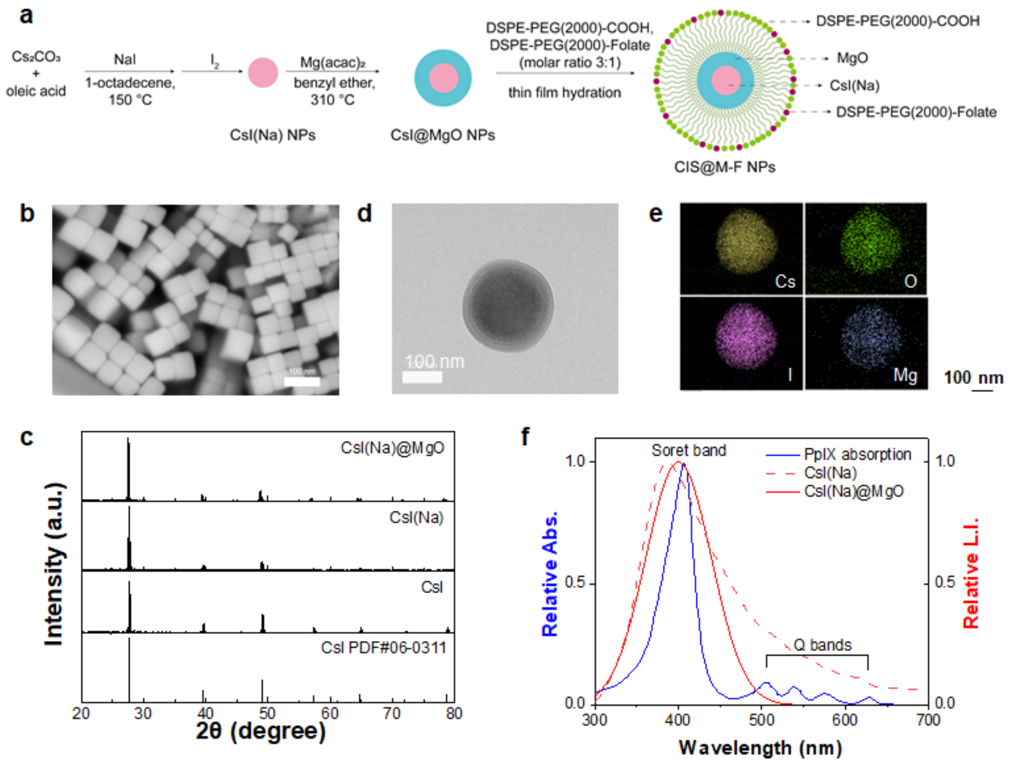

Figure 3.1 Synthesis and characterizations of CsI(Na) and CsI(Na)@MgO nanoparticles. a) Schematic illustration of CsI(Na)@MgO synthesis and surface modification. b) SEM of CsI(Na) nanoparticles. Scale bar, 100 nm. The average nanoparticle size was 55 ± 15 nm, determined by ImageJ. c) XRD spectra of CsI(Na)@MgO, CsI(Na), and CsI (no Na dopant) nanoparticles, as well as a CsI standard (PDF#06-0311 from the JCPDS database). d) TEM image of a single CsI(Na)@MgO nanoparticle. e) EDX elemental analysis of a single CsI(Na)@MgO nanoparticle. Scale bar, 100 nm. f) X-ray luminescence spectra of CsI(Na) (dashed red) and CsI(Na)@MgO (solid red) nanoparticles, along with the absorption spectrum of PpIX (blue). Abs., absorbance. L.I., luminescence intensity.

Evaluate X-PDT with CIS@M-F and 5-ALA in solutions

We coated CsI(Na)@MgO nanoparticles with DSPE-PEG-COOH and DSPE-PEG-Folate (molar ratio 3:1) through thin-film hydration. The resulting CsI(Na)@MgO@DSPE-Folate nanoparticles, hereafter referred to as CIS@M-F, are readily dispersed in aqueous solutions. Dynamic light scattering (DLS) showed that the average hydrodynamic size of CIS@M-F was 190.2 ± 30.1 nm (Figure 2a). For comparison, CsI(Na)@MgO nanoparticles without a phospholipid coating were 175.2 ± 37.5 nm (in hexane, Figure 2a). Z-potential analysis found that CIS@M-F were slightly negatively charged (-22.5 mV, Figure S2a), which is attributed to the surface carboxyl groups.

We studied the degradation of CIS@M-F in PBS, tracing iodine released from the nanoparticles by ICP-MS. For comparison, we also tested uncoated CsI(Na) nanoparticles (which can be temporally dispersed in PBS). Uncoated CsI(Na) nanoparticles rapidly degraded, releasing >90% of their iodine within 30 min (Figure 2b). CIS@M-F showed significantly improved water stability. While a small amount of iodine was released at the beginning of incubation, virtually no iodine was leaked after one hour. After 24 hours, CIS@M-F remained a stable colloidal solution, while CsI(Na) solutions turned completely transparent due to degradation (Figure S2b).

To test whether CIS@M-F can activate PpIX under X-ray irradiation, we prepared solutions containing CIS@M-F, PpIX, and methylene blue (MB), and irradiated the solutions by X-rays (5 Gy). We observed a significant drop of 664 nm absorbance (Figure 2c), suggesting MB being quenched by newly generated ROS. As a comparison, solutions containing CIS@M-F or PpIX only showed moderate MB quenching under the same condition. We next examined $^1O_2$ production using singlet oxygen sensor green (SOSG) as a fluorogenic sensor. SOSG intensity was increased by more than 4-fold in solutions containing both CIS@M-F and PpIX (Figure 2d), suggesting PpIX activation. As a comparison, solutions containing CIS@M-F or PpIX alone showed a minor SOSG intensity increase when irradiated. To validate that PpIX can be activated through X-PDT, we placed solutions containing CIS@M-F and PpIX under 3-cm-thick tissues and irradiated from atop (Figure S2c). We observed comparable levels of SOSG fluorescence upon X-ray radiation (Figure 2d). On the contrary, LED light failed to activate PpIX under this condition. Overall, our solution studies support that X-PDT can be activated under irradiation if both PpIX and CIS@M-F are present.

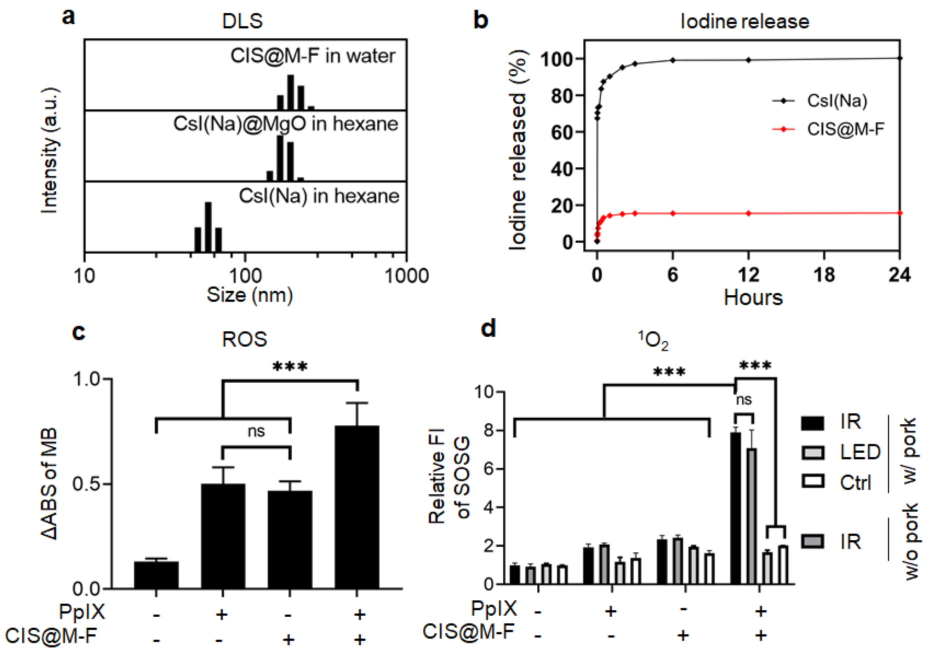

Figure 3.2 Stability and X-ray luminescence of CsI(Na)@MgO@DSPE-Folate nanoparticles (CIS@M-F). a) DLS analysis of CsI(Na), CsI(Na)@MgO, and CIS@M-F nanoparticles. The hydrodynamic sizes are 58.7 ± 8.0 nm and 175.2 ± 37.5 nm, respectively, for CsI(Na) and CsI(Na)@MgO nanoparticles (in hexane). CIS@M-F can be stably dispersed in water, with a hydrodynamic size of 190.0 ± 30.0 nm. b) Iodine release from CsI(Na) and CIS@M-F nanoparticles in PBS (pH 7.4). c) ROS production under ionizing irradiation (IR, 5 Gy), measured with solutions containing CIS@M-F with or without PpIX, using methylene blue (MB) as an indicator. A decreased absorbance at 664 nm suggests an elevated ROS level. The experiments were repeated in quintuplicates. ***, $p < 0.001$; ns, $p > 0.05$. d) $^1O_2$ generation under ionizing irradiation (IR, 5 Gy), measured with solutions containing CIS@M-F with or without PpIX, using SOSG (ex/em: 504/525 nm) as an indicator. Solutions were placed under 3-cm-thick pork. For comparison, LED light instead of X-rays was applied. The experiments were repeated in triplicates. ***, $p < 0.001$; ns, $p > 0.05$.

Evaluate X-PDT *in vitro* in cells treated with CIS@M-F and 5-ALA

We first studied CIS@M-F uptake by 4T1 cells, in which folate receptor is upregulated. To this end, we labeled CIS@M-F with rhodamine-B. For comparison, we also prepared rhodamine-B-labeled CsI(Na)@MgO nanoparticles coated with DSPE-PEG-COOH only (referred to as CIS@M-C). Flow cytometry found significantly increased median fluorescence intensity (MFI) of rhodamine-B in cells treated with CIS@M-F relative to those treated with CIS@M-C (Figure 3a). Extending incubation time from 2 to 6 hours increased uptake but the change was not marked (Figure 3a). These results indicate that CIS@M-F were quickly internalized by cancer cells through receptor-mediated endocytosis.

We then investigated the impacts of X-PDT on cells. Briefly, 4T1 cells were incubated with CIS@M-F (100 μg mL^{-1}) and 5-ALA (200 μg mL^{-1}) for 3 hours, and then treated with ionizing radiation (IR, 320 kV, 5 Gy). We chose this drug-radiation interval because the 5-ALA-to-PpIX conversion peaked at ~3 hours (Figure S3a&b). Note that CIS@M-F and 5-ALA are not toxic to cells at the above therapeutic doses when there is no radiation (Figure S3c&d).

We first examined intracellular ROS level changes. Relative to un-irradiated cells, cells treated with IR alone showed an increased level of hydroxyl radical, measured with aminophenyl fluorescein or APF, a fluorogenic sensor of ·OH (Figure 3b); this is mainly attributed to radiolysis of water. Treatment with 5-ALA prior to IR slightly elevated ·OH relative to IR alone but the increase was insignificant (p=0.3865). Pre-treatment with CIS@M-F or a combination of CIS@M-F and 5-ALA moderately increased ·OH levels. The increase is attributed to high-Z element effects, which was observed with other nanoparticles.[51] Meanwhile, SOSG fluorescence intensity was not increased in cells treated with IR alone but more than doubled when cells were pre-treated with the CIS@M-F and 5-ALA combination (Figure 3c). The result is consistent with observations made from solutions, supporting that X-PDT is activated in cells pre-treated with CIS@M-F and 5-ALA prior to IR.

Next, we evaluated the activities of superoxide dismutase (SOD) and manganese-dependent superoxide dismutase (MnSOD) in cells treated with CIS@M-F, 5-ALA, or their combination, with or without radiation. We observed significantly increased SOD and MnSOD activities in cells treated with CIS@M-F+5-ALA+IR (Figure 3d&e), indicating cell response to elevated ROS. In particular, MnSOD activity was more than 3 times higher than cells treated with CIS@M-F+5-ALA or IR alone (Figure 3e), which is attributed to the fact that PpIX activation in focused on mitochondria. Mitochondria-targeted activation was supported by the observation that mitochondria membrane potential ($\Delta\Psi_m$) significantly dropped in cells treated with CIS@M-F+5-ALA+IR (Figure 3f). Note that destructed mitochondria may promote secondary ROS that further oxidative stress.[52]

Elevated ROS may cause oxidative damage to a broad range of biomolecules such as DNA, lipids, and proteins. γH2AX staining revealed a significant increase of positively stained foci per cell in cells treated with CIS@M-F+5-ALA+IR relative to IR alone (Figure 3g and Figure S3e). Consistent with APF results, CIS@M-F+IR moderately increased double-strand breaks which is attributed to nanoparticle high-Z effects (Figure 3g). C11-BODIPY staining found a significant increase of 510-nm fluorescence in cells treated with CIS@M-F+5-ALA+IR (Figure 3h), suggesting elevated lipid peroxidation. Extensive oxidative damages, including damage to the mitochondria, triggered apoptosis, which was evidenced with increased caspase-3 activity (Figure 3i). ATP bioluminescence viability assay also confirmed reduced cell viability when cells were treated with the CIS@M-F+5-ALA+IR (Figure 3j).

Lastly, we evaluated how X-PDT affects cancer cell clonogenicity. We treated 4T1 cells with the same amounts of CIS@M-F (100 μg mL^{-1}) and 5-ALA (200 μg mL^{-1}) as the other *in vitro* experiments but varied the radiation doses (0-9 Gy). After 14 days, the survival fraction (S) relative to un-treated controls was calculated and fit into a linear-quadratic equation, $S = e^{-(aD+bD\text{^}2)}$, where D is the radiation dose and a and b are fitting coefficients (Figure 3k and Figure S4a). CIS@M-F+5-ALA+IR reduced the number of colonies formed at all radiation doses. D_{10}, dose required to achieve 10% clonogenic survival, was 4.45 (Figure 3i and Figure S4b). This corresponds to a dose modifying factor (DMF) of 1.54. As a comparison, D_{10} values were 5.15 and 6.69 for CIS@M-F+IR and 5-ALA+IR, respectively, corresponding to DMFs of 1.33 and 1.02, respectively (Figure 3i). Overall, our *in vitro* results support that under irradiation, the CIS@M-F-and-5-ALA combination enables X-PDT, promoting reduction in cell proliferation and reproduction relative to IR alone.

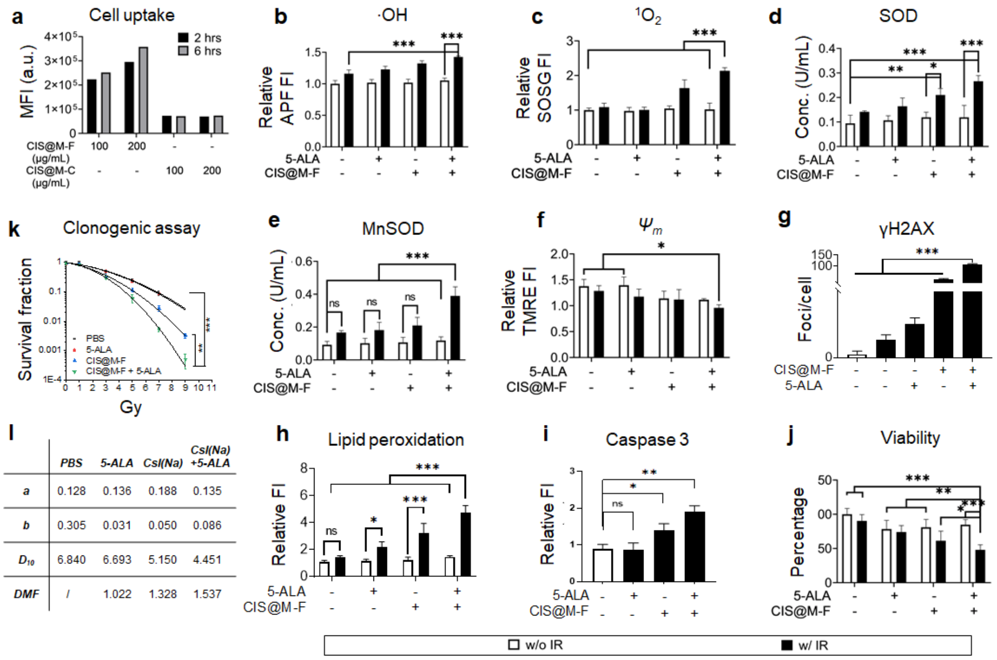

	PBS	5-ALA	CsI(Na)	CsI(Na) +5-ALA
a	0.128	0.136	0.188	0.135
b	0.305	0.031	0.050	0.086
D_{10}	6.840	6.693	5.150	4.451
DMF	/	1.022	1.328	1.537

Figure 3.3 *In vitro* X-PDT with CIS@M-F and 5-ALA, evaluated with 4T1 cells. a) Cell uptake, investigated with Rhodamine B labeled CIS@M-F or CIS@M-C (CsI(Na)@MgO nanoparticles

coated with DSPE-PEG-COOH only) nanoparticles using flow cytometry. MFI, median fluorescence intensity. Increased cell uptake was observed with CIS@M-F compared to CIS@M-C at both 100 and 200 µg/mL. b-e) Impact of CIS@M-F and 5-ALA on cellular oxidative stress. 4T1 cells were incubated with CIS@M-F (100 µg mL^{-1}), 5-ALA (200 µg mL^{-1}), or their combination, followed by IR (5 Gy). All experiments were repeated in quintuplicates. b) Cellular hydroxyl radical levels, measured with APF (ex/em: 490/515 nm). c) Cellular $^1O_2$ levels, measured with SOSG (ex/em: 504/525 nm). Cytosol SOD d) and mitochondrial MnSOD e) activities, measured with Superoxide Dismutase Assay Kit. f) Mitochondrial membrane potentials (Ψ_m), measured with TMRE assay. g) Double-strand DNA beaks, measured with anti-rH2AX staining. Positively stained foci per cells were quantified by ImageJ. h) Lipid peroxidation, measured with C11-BIDOPY (ex/em: 488/510 nm) assay. i) Cell viability, measured with ATP bioluminescence assay at 24 h. j) Tumorigenicity, measured with clonogenic assay at a range of radiation doses (0-9 Gy; n=3). k) Summary of linear-quadratic ($S = e^{-(a\mathrm{D}+b\mathrm{D}^\wedge 2)}$) fitting results, based on clonogenic assay results from j. D_{10}, dose required to achieve 10% survival. DMF, does modifying factor, based on D_{10} values. *, $p < 0.05$; **, $p < 0.01$; ***, $p < 0.001$; ns, $p > 0.05$.

Evaluate X-PDT with CIS@M-F and 5-ALA *in vivo*

We inoculated 4T1 cells into the right flanks of 5-6-week female nude mice. When tumor volume reached 50 mm^3, we intraperitoneally (i.p.) administered 50 mg kg^{-1} 5-ALA (Day 1). The same or a similar dose is commonly used in small animal studies and induces PpIX accumulation in tumors after 3 hours.[34, 53, 54] We intratumorally (i.t.) injected CIS@M-F (1.25 mg kg^{-1}) after 1 hour and delivered 3 Gy of radiation to the tumor area after 3 hours (CIS@M-F+5-ALA+IR, n=5). The rest of the animal body was protected with lead. Two more treatment sessions were applied on Days 3 and 5 (Figure 4a). Control treatments included PBS only, CIS@M-F+5-ALA, CIS@M-F+IR, 5-ALA+IR, and IR alone (n=5). Without treatment, 40% of the animals reached a humane endpoint within 16 days (Figure 4a&b). IR alone was moderately therapeutic, inhibiting tumor growth by 26.2% on Day 16 (Figure 4a). Animals in the 5-ALA+IR and CIS@M-F+IR groups exhibited tumor inhibition rates at 45.5% and 53.9%, respectively; the differences however were insignificant relative to IR alone (*p* = 0.5363 and 0.8056, respectively). By contrast, animals in the CIS@M-F+5-ALA+IR group led to a tumor inhibition of 164.3% compared to IR alone (Figure 4b, *p* = 0.0019). All mice in the CIS@M-F+5-ALA+IR group remained alive after three weeks (Figure 4c). Histopathology found reduced cell density and decreased levels of positive-Ki67 staining in tumors from the CIS@M-F+5-ALA+IR group (Figure 4d). Meanwhile, there was no acute toxicity nor body weight drops throughout the experiment (Figure 4e). H&E staining found no signs of toxicity to normal tissues (Figure 5a).

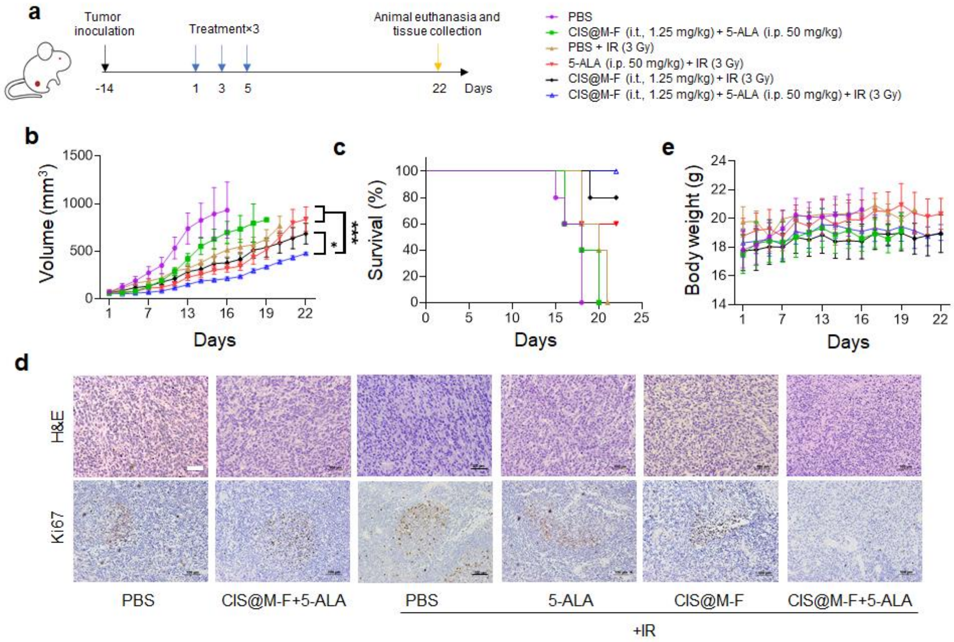

Figure 3.4 *In vivo* studies to evaluate the efficacy of X-PDT with CIS@M-F and 5-ALA. Experiments were performed in 4T1-tumor bearing balb/c mice. a) Scheme of experimental

design. On Day 1, animals received one of the following regimens, including PBS plus ionizing radiation (PBS+IR), 5-ALA with IR (5-ALA+IR), CIS@M-F plus IR (CIS@M-F+IR), PBS only (PBS), CIS@M-F plus 5-ALA without IR (CIS@M-F+5-ALA), and CIS@M-F plus 5-ALA plus irradiation (CIS@M-F+5-ALA+IR). 5-ALA (50 mg kg^{-1} in PBS) was i.p. administered, while CIS@M-F in PBS (1.25 mg kg^{-1}) were intratumorally administered 2 hours after the 5-ALA injection. IR (3 Gy) was applied to tumors 1 hour after CIS@M-F administration. Two more sessions of treatment were given on Days 3 and 5. Animals were euthanized after 3 weeks or when a humane endpoint was reached. b) Tumor growth curves. *, $p < 0.05$; ***, $p < 0.001$. c) Kaplan Meier survival curves. d) Post-mortem staining of tumor tissues, with H&E (upper) and Ki67 (lower). Scale bar, 100 µm. e) Animal body weight curves.

To better understand the side effects and clearance of CIS@M-F, in a separate study, we intravenously injected CIS@M-F into healthy balb/c mice and collected blood and tissues on Day 14 for complete blood counts (CBCs), serum biochemistry, and histopathology analyses (Figure 5b). All CBC indices and liver and kidney function markers including alanine transaminase (ALT) and urea nitrogen (BUN) were within normal ranges[55] (Figure 5c). H&E staining found no abnormalities in all tissues (Figure S5). Post-mortem ICP-MS studies revealed that the Cs and I levels in all tissues fell to baseline or close-to-baseline levels after two weeks (Figure 5d). Overall, our *in vivo* studies confirm that X-PDT by CIS@M-F+5-ALA can significantly enhance tumor suppression without causing additional toxicities.

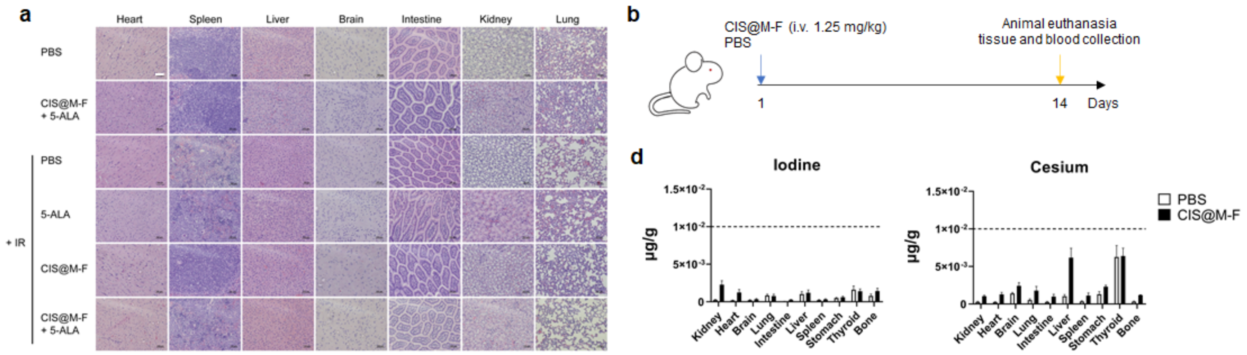

c

		RBC	Hgb	HCT	MCV	MCH	MCHC	RDW	PLT	MPV	WBC	NEUT	LYM	MONO	EOS	BASO	BUN	ALT
Unit		$x10^6/\mu L$	g/dL	%	fL	Pg	g/dL	%	$x10^3/\mu L$	fL	$x10^3/\mu L$	$x10^3/\mu L$	$x10^3/\mu L$	$x10^3/\mu L$	$x10^3/\mu L$	$x10^3/\mu L$	mg/dL	Unit/L
Ref.	*low*	6.50	11.0	35.0	41.0	13.0	30.0	12.0	400	4.0	0.8	0.23	0.60	0.04	0.00	0.00	7.0	40.0
	high	11.50	16.5	55.0	55.0	18.0	36.0	19.0	1600	6.2	10.6	3.60	8.90	1.40	0.51	0.12	31.0	170.0
PBS	*Ave.*	10.21	15.65	46.60	45.60	15.35	33.70	14.35	887	5.70	6.95	1.46	5.21	0.21	0.05	0.06	14.8	48.8
	Std.	0.36	0.64	2.12	0.42	0.07	0.14	0.07	97	0.14	0.78	0.08	0.64	0.04	0.01	0.01	2.1	1.6
CIS@M-F	*Ave.*	10.23	15.70	46.93	45.90	15.33	33.43	14.33	900	5.67	8.70	1.10	7.21	0.22	0.08	0.06	26.9	50.3
	Std.	0.22	0.20	1.10	0.10	0.15	0.40	0.25	95.01	0.06	3.55	0.51	3.07	0.05	0.03	0.01	0.5	6.5

Figure 3.5 Safety and clearance of CIS@M-F. a) H&E staining of tissues harvested from animals treated with regimens detailed in Figure 4. Scale bar, 100 μm. b) Scheme of experimental plans. In a separate experiment, CIS@M-F (1.25 mg/kg) or carrier only (PBS) was i.v. administered into healthy balb/c mice (n=5). Animals were euthanized after two weeks for CBC and serum biochem analyses. In addition, remaining cesium and iodine in tissues were analyzed by ICP-MS. c) Summary of CBC and serum biochem results, along with reported normal ranges of the indices. RBC, red blood cells; Hgb, hemoglobin; HCT, hematocrit; MCV, mean corpuscular volume; MCH, mean corpuscular hemoglobin; MCHC, mean corpuscular hemoglobin concentration; RDW, red cell distribution width; PLT, platelets; MPV, mean platelet volume; WBC, white blood cells; NEUT, neutrophils; LYM, lymphocytes; MONO, monocytes; EOS, eosinophils; BASO, basophils; BUN, blood urea nitrogen; ALT, alanine transaminase. d) Iodine (left) and cesium (right) remaining in organ tissues on Day 14. Contents of both elements fell well below 10 ng/g.

3.4 Conclusions

While CsI(Na) is an established scintillator material, CsI(Na) nanoparticles have seldom been explored. Employing CsI(Na) nanoparticles for X-PDT has not been reported. Herein we successfully synthesized CsI(Na) nanoparticles and, for water protection, coated them with MgO. We showed that X-ray luminescence from CsI(Na) nanoparticles can activate PpIX in 5-ALA-treated cells, enhancing mitochondria, DNA, and lipid damages thereby sensitizing cancer cells to RT. This strategy is distinct from conventional X-PDT approaches in that the scintillator (CIS@M-F) and PS (5-ALA) are administered separately rather than as a conjugate. CsI(Na)@MgO nanoparticles are synthesized by wet chemistry that is highly scalable. The approach is less affected by issues such as batch-to-batch variations, complex nanostructures, and suboptimal control in PS loading and release. Other benefits include high tumor selectivity (PpIX selectively accumulates in cancer cells and its activation takes place only when both CsI(Na) NPs and X-rays are present) and high efficiency (the PDT component focuses on mitochondria, which are sensitive to phototoxicities). Some have reported on the radio-sensitizing effects of 5-ALA.[56-58] In our *in vitro* and *in vivo* studies, however, we did not observe therapeutic benefits when 5-ALA was applied alone. This might be attributed to differences in radiation doses and animal models.

For proof-of-concept, we intratumorally injected CsI(Na) nanoparticles in therapy studies, which is common among X-PDT studies,[22, 26, 27, 59]. The injection route is viable for treating cancer types such as breast, prostate, and skin cancers.[22, 31, 60] It is possible to systemically administer CsI(Na) nanoparticles, whereby they accumulate in tumors through passive or active targeting. Tumor-targeting ligands other than folic acid may be imparted to the nanoparticle surface depending on targeted indications.

As afore-mentioned, one major advantage of the current approach is the low toxicity of both the PS and the scintillator. 5-ALA is FDA-approved and has been used in clinical PDT and image-guided brain surgery. CsI(Na) nanoparticles degrade into alkali and halogen ions that are safely excreted after treatment. The demonstrated biocompatibility and potential scalability of the nanoplatform ideally position this technology for further developments and clinical translation.

CHAPTER 4

MULTIPLEXING PHOTOSENSITIZERS WITH DUAL-WAVELENGTH NANOSCINTILLATORS AMELIORATE CANCER VIA RADIODYNAMIC THERAPY[3]

---

[3] Fangchao Jiang, Zhengwei Cao, Wei Yang, Shuyue Zhan, Jianwen Li, Zhi Liu, Yong Teng, Zibo Li, Jin Xie. To be submitted to Advanced Materials

ABSTRACT

Compared to conventional photodynamic therapy (PDT), X-ray induced photodynamic therapy (X-PDT) or radiodynamic therapy can potentially target deep-seated tumors. Because of this, there are ascending trends in exploring novel nanoconjugates for X-PDT. However, most nanoconjugates proposed require tedious processing and disqualify the need for a promising therapeutic efficacy for clinical transition. Because of that, we took advantage of our previous CsI(Na)@MgO nanoparticles and rationally designed a dual-wavelength CsI(CO_3, Na)@ZnS nanoparticle for cancer treatment. This co-doping nanoparticle can give off luminescence around 410 nm and 500 nm under irradiation, and we believe that it can be utilized to target nearby photosensitizers for elevated organelles damage. Inspired by this nanoparticle, we chose 5-ALA and Redaporfin as our two photosensitizers that are both clinically FDA approved. Because each photosensitizer can selectively absorb a specific wavelength of light and preferably accumulate in different organelles, this combination would favor the activation of reactive oxygen species and damage nearby mitochondria and the endoplasmic reticulum. For proof-of-concept, we chose CT26 colon cancer cell lines here and tested this concept *in vitro* and *in vivo*. *In vitro* studies with CT26 cells and our nanoplatform manifested the successful activation of multiplexing photosensitizers followed by apoptosis and immunogenic cell death. *In vivo* studies with CT26-bearing balb/c mice further consolidated our hypothesis, and tumors from treatment groups were eradicated without observed future recurrence. In short, external X-rays can trigger our nanoparticles and give off both ultraviolet and blue-green light for separate photosensitizer activation. The activation can then induce the mitochondria-oriented apoptosis and endoplasmic

reticulum-oriented immunogenic cell death process. Together with cell nucleus damage after irradiation, this approach can ameliorate cancer and stimulate the immune system against long-term cancer development.

4.1 Introduction

Thanks to the high selectivity and minimal side effect of photodynamic therapy, PDT is acknowledged as one of the provident cancer treatment modalities. However, most of the photosensitizers for PDT can only be efficiently activated by ultraviolet, visible, or near infrared light, and one concern people have is the limited penetration ability of those light sources. Even the near infrared light, which supposes to show strong penetrative capability, can hardly pass through more than 1 cm of tissue for deep-seated photosensitizer activation. Inspired by this, we and some other groups came up with the concept called X-ray induced photodynamic therapy or radiodynamic therapy[2, 131, 167-169]. For instance, we previously utilized SAO, LGO:Cr, and CsI(Na)@MgO for X-PDT and fulfilled the goal of tumor growth inhibition[43, 60, 170]. Those nanoplatforms were quite effective while still cannot get clinical acceptance due to the suboptimal therapeutic efficacy and potential tumor reoccurrence afterward. To circumvent these, we picked multiplexing photosensitizers to target different intracellular organelles for enhanced therapeutic efficacy. We choose 5-ALA as a prodrug of PpIX, which can accumulate in CT26 cancer cells' mitochondria and induce mitochondria damage-related apoptosis[171]. We also select Redaporfin, an FDA approved potent photosensitizer that can cause a direct antineoplastic effect by targeting the endoplasmic reticulum[172]. Its attack can further recall the immune-dependent destruction and achieve long-term tumor inhibition and recurrence. Owing to the characteristics of each photosensitizer, both photosensitizers can be intravenously or intraperitoneally injected and home to cancer sites by themselves. And this avoids the tedious manufacturing process for a conjugated nanoplatform potentially possessing several drawbacks[170]. We further choose CsI(CO_3, Na) co-doping nanoparticles as our energy transducer because this particle can absorb X-ray photons and give off both ultraviolet and blue-green light for separate photosensitizer activations. So far, CsI(Na) nanoparticles have been reported by our group as an X-PDT reagent, and there are no records concerning co-doped CsI nanoparticles as for X-PDT. Furthermore, we utilized ZnS as our coating material because of its remarkable stability and biocompatibility. The core@shell CsI(CO_3, Na)@ZnS nanoparticles are then modified with folate ligands to improve their intracellular uptakes and tumor homing capability.

We believe the current nanoplatform has multiple fabulous merits compared to previous nanoplatforms. First, this nanoplatform involves multiplexing photosensitizers that can attack separate intracellular components for cell death. Secondly, both photosensitizers are FDA approved and are both safe as well as accessible via intravenous injection. Thirdly, we have a one-pot synthesis of a co-doped nanoscintillator that is bio-friendly and can down convert X-ray photons to ultraviolet and blue-green photons for nearby photosensitizer activations. Lastly, *in vitro* and *in vivo* studies with CT26 cancer cells and balb/c mice perfectly substantiated our hypothesis. And we noticed that mitochondria-mediated apoptosis synergized with immunogenic death and cell nucleus damage, all of which resulted in tumor eradication and recurrence.

4.2 Materials and Methods

Materials

Cs_2CO_3 (99%, Sigma, Cat#441902), I_2 (≥99.8%, Sigma, Cat#207772), NaI (≥99.5%, Sigma, Cat#383112), thioacetamide (≥99%, Sigma, Cat#163678), zinc acetate (99.99%, Sigma, Cat#383317), 1-Octadecene ($C_{18}H_{36}$, technical grade, 90%, Sigma, Cat#0806), oleic acid ($C_{18}H_{34}O_2$, technical grade, 90%, Sigma, Cat#364525), oleylamine ($C_{18}H_{35}NH_2$, technical grade, 70%, Sigma, Cat#07805), 1,2-hexadecanediol (technical grade, 90%, Sigma, Cat#213748), hexane (C_6H_{14}, ≥99%, Sigma, Cat#139386), ethanol (anhydrous, Sigma, Cat#443611), chloroform ($CHCl_3$, ≥99.8%, Fisher Scientific), 1,2-dipalmitoyl-sn-glycero-3-phosphoethanolamine-N-(lissamine rhodamine B sulfonyl) (ammonium salt) (16:0 Liss Rhod PE) (Avanti, Cat#810158), 1,2-distearoyl-sn-glycero-3-phosphoethanolamine-N-[carboxy(polyethylene glycol)-2000] (sodium salt) (DSPE-PEG(2000) Carboxylic Acid) (Avanti, Cat#880135), 1,2-distearoyl-sn-glycero-3-phosphoethanolamine-N-[folate(polyethylene glycol)-2000] (ammonium salt) DSPE-PEG(2000) Folate (Avanti, Cat#880124), phosphate buffer saline (PBS, pH 7.2), Milli-Q Water (H_2O, 18.2 MΩ.cm@25℃).

Synthesis of CsI(CO_3, Na) nanoparticles

0.203 g Cs_2CO_3 was mixed with 10 mL 1-octadecene and 1 mL oleic acid in a 100 mL flask. The solution was heated to 150 ℃ and maintained at this temperature for 30 mins with magnetic stirring. Next, 1 mL oleylamine, 0.02954 g 1,2-hexadecanediol, 0.020 g Cs_2CO_3, and 0.01 g NaI were added into the mixture. After reacting for 10 minutes, the solution was cooled to room temperature, and 0.2030 g I_2 were added. The flask was then quickly transferred to a water bath and kept stirring for another 3 hours. CsI(CO_3, Na) nanoparticles were collected by centrifugation and washed with a mixture of 10 mL hexane and 0.5 mL ethanol for 3 times.

Synthesis of CsI(CO_3, Na)@ZnS nanoparticles

In a typical reaction, 10 mg CsI(CO_3, Na) nanoparticles were prepared in 10 mL ODE. The solution was sonicated and vigorously stirred following with the addition of 9 mg Zn acetate and 0.1 mL OAm. After that, the solution was gradually heated up to 100 °C under Argon protection and maintained at this temperature for 20 min. Thioacetamide (6-10 mg) was then introduced into the system as the S source. The reaction continued for 20 min before transferring to a water bath for cooling. The product was collected by centrifugation under 10000 rpm*10 mins and washed with a mixture of 6 mL hexane and 3 mL ethanol 3 times.

Synthesis of CIZS@M-F

20 mg CsI(CO_3, Na)@ZnS nanoparticles were dispersed in 2 mL chloroform. Into the solution, 75 µL of DSPE-PEG(2000)-COOH in chloroform (10 mg mL^{-1}) and 25 µL DSPE-PEG(2000)-Folate in chloroform (10 mg mL^{-1}) were added. The mixture was stirred at room temperature overnight, and the solvent was removed by rotary evaporation. The nanoparticles were dispersed in PBS and passed through a desalting column before use.

Synthesis of CIZS@M-F or CIZS@M-C with rhodamine B labelling

20 mg CsI(CO_3, Na)@ZnS nanoparticles were dispersed in 2 mL chloroform. Into the solution, 50 µL of DSPE-PEG(2000)-COOH in chloroform (10 mg mL^{-1}) and 25 µL DSPE-PEG(2000)-Folate in chloroform (10 mg mL^{-1}) together with 25 µL of 16:0 Liss Rhod PE in chloroform (10 mg mL^{-1}) were added. The mixture was stirred at room temperature overnight, and

the solvent was removed by rotary evaporation. The nanoparticles were dispersed in PBS and passed through a desalting column before use.

Nanoparticle characterizations

Nanoparticle crystallinity was assessed using the Bruker D8-Advance X-ray diffraction (XRD) diffractometer with Cu Kα radiation ($\lambda = 1.5418$ Å) at a scanning rate of 10° min^{-1}. The hydrodynamic sizes and surface charges of the particles were characterized on a Malvern Zetasizer Nano ZS system. Nanoparticle size, morphology, and elemental analysis was characterized using a Scanning Electron Microscope (FE-SEM Thermo Fisher Teneo) which was equipped with an EDX system and Transmission Electron Microscope (FEI Tecnai20 and FEI Tecnai G2 F30 Hi-Res TEM). Nanoparticle composition was analyzed by Inductively Coupled Plasma Atomic Emission Spectroscopy using an Xseries II ICP/MS system (Thermo Electron Corporation). An iodide-selective electrode was used to conduct release experiments in PBS solutions of nanoparticles at room temperature (Mettler Toledo perfectION™).

Radical production in solution

ROS (reactive oxygen species) were measured with the APF assay ($\text{Invitrogen}^{\text{TM}}$ Cat#A36003) and SOSG kit ($\text{Invitrogen}^{\text{TM}}$ Cat#S36002) in solution firstly.[147, 148] NPs were mixed with PpIX (1 mg/mL) or Redaporfin (10 μg/mL) solutions for ROS test. The solutions were further mixed with APF (5μM) and SOSG (5μM) kit to prepare the final solutions. 5 Gy X-ray irradiation was applied and fluorescence signals before and after irradiation were compared via a microplate reader (Biotek).

Cell culturing

CT26 colon cancer cells were used for *in vitro* and *in vivo* studies. Cells were grown in RPMI1640 medium which was supplemented with 10% FBS and 100 units mL^{-1} of penicillin (ATCC). Cells were maintained in a humidified, 5% carbon dioxide (CO_2) atmosphere at 37 °C.

ATP viability assay to test X-PDT efficacy

The ATP viability assay was performed according to the manufacturer's protocol (PerkinElmer, ATPlite 1step Luminescence Assay Cat#6016736). CT26 cells were seeded at 5000 cells/well in a white 96-well plate and incubated for 24 hours. After that cells were then incubated together with 5-ALA (1 mg/mL) or redaporfin (10 µg/mL) in RPMI medium. Two hours later, NPs (100 µg/mL) were added into each well, and cells were further irradiated with 5 Gy X-ray irradiation. After 24 hours, ATP1lite assay was utilized for quantification of cell viabilities.

In vitro intracellular PpIX analysis

PpIX extraction was performed according to a published protocol.[146] CT26 Cells were seeded in a 6-well plate at 10000 cells/well. When cells confluency reaches 80%, 5-ALA (20 µL, 5 mg/mL) was added into each well, and cells were incubated together with 5-ALA for different time points. After that cells were trypsinized, harvested by centrifugation, and redispersed in 5% HCl at 37 °C for an hour. Following incubation in acid, the supernatant was collected and fluorescence signals (ex/em: 406/604 nm) were recorded.

In vivo intracellular PpIX analysis with Newton imaging system

5-ALA (50 mg kg-1 in PBS) was intraperitoneally injected into CT26 bearing balb/c mice 2 hours before imaging. The luminescence signals based on the excitation of 640 nm light were recorded and quantified.

ROS generation *in vitro*

The ROS generation was conducted following the vendor's protocol. CT26 cells were seeded in 96-well plates at 5000 cells/well. Following 24 hours of incubation, the medium was aspirated CT26 cells were incubated together with 5-ALA (1 mg/mL) or Redaporfin (10 µg/mL) in RPMI medium. Two hours later, NPs (100 µg/mL) were added into each well, and cells were further mixed with H2DCFDA (5µM) and SOSG (5µM) kit to prepare the final solutions. 5 Gy X-ray irradiation was applied and fluorescence signals (ex/em: 504/525 nm) before and after irradiation were recorded and compared.

Cell uptake studies

Cell uptake of CIZS@M-C and CIZS@M-F nanoparticles were analyzed on a CytoFLEX flow cytometer. CT26 cells were seeded at 0.5×10^6 cells/well into 6-well plates. Then, nanoparticles were incubated with cells at a final nanoparticle concentration of 100 µg mL^{-1}. Both CIZS@M-F and CIZS@M-C were labeled with Rhodamine B following a published protocol.[149] Following either 2 or 6 hours of incubation, cells were harvested for flow cytometer analysis, and the MFI was recorded.

SOD activity

SOD activity was assessed following the vendor's protocol (Cayman Chemical Cat#706002). CT26 cells were seeded into 6-well plates at 1 million cells/well. After 24 hours, CT26 cells were incubated with NPs (100 µg mL-1), 5-ALA (1 mg/mL) or Redaporfin (10 µg/mL) for 2 hours prior to receiving 5 Gy irradiation. After irradiation, the cells were further incubated for 12 hours and were then harvested and followed with SOD assay (Cayman) for MnSOD and Cytostol SOD tests. Absorbance (450 nm) was measured on a microplate reader (Biotek).

Lipid peroxidation

The Image-iT Lipid Peroxidation Kit (Invitrogen^{TM} Cat#C10445) was used to assess lipid peroxidation. CT26 cells were subcultured in a 96-well plate at the density of 5000 cells per well, CT26 cells were incubated together with 5-ALA (1 mg/mL) or redaporfin (10 µg/mL) in RPMI medium. Two hours later, NPs (100 µg/mL) were added into each well, and cells were irradiated with 5 Gy X-ray after an hour of incubation. The irradiated cells were further cultured for 6 hours before lipid peroxidation analysis. After incubation, the treated cells were incubated with 10 µM of lipid peroxidation sensor (Life technologies) for 30 min in complete growth medium at 37 °C. The cells were washed once with PBS and then the fluorescence intensity of the reduced state (red, ex/em: 581/591 nm) and oxidized state (green, ex/em: 488/510 nm) were analyzed. The data were represented as red/green fluorescence intensity ratios

Caspase-3 activity

CT26 cells were incubated with NPs(100 µg mL-1), 5-ALA (1 mg/mL) or Redaporfin (10 µg/mL) for 2 hours prior to receiving 5 Gy X-ray irradiation. Control treatments included NPs, 5-

ALA, or PBS. Following 24 hours of incubation, cells were stained with the FAM-FLICA® Caspase-3/7 kit (Immunochemistry, Cat# 94) following the manufacturer's protocol. The caspase-3 activity was evaluated by measuring fluorescence signals (ex/em: 488/530 nm) on a microplate reader (Synergy Mx, BioTeK).

Mitochondrial membrane potential ($\Delta\Psi_m$)

The change of mitochondrial membrane potential was measured by a JC-1 mitochondrial membrane potential detection kit (Biotium, Cat No.: 30001). The JC-1 working solution was prepared by adding 10 μL of the concentrated dye to 1 mL of FBS-free RPMI medium. CT26 cells were subcultured in a 96-well plate at the density of 5000 cells per well, CT26 cells were incubated together with 5-ALA (1 mg/mL) or redaporfin (10 μg/mL) in RPMI medium. Two hours later, NPs (100 μg/mL) were added into each well, and cells were irradiated with 5 Gy X-ray after an hour of incubation. The irradiated cells were further cultured for 6 hours before mitochondria potential analysis. After incubation, the treated cells were incubated with JC-1 working solution for 15 mins at 37 °C. And the data were represented as red(585/590)/green(510/527) fluorescence intensity ratios using 96-well microplate reader.

Extracellular ATP assay

CT26 Cells were seeded into 6-well plates at the density of 1×104 cells per well and incubated overnight. When the cells confluency reach 80%, CT26 cells were incubated together with 5-ALA (1 mg/mL) or redaporfin (10 μg/mL) in RPMI medium. Two hours later, NPs (100 μg/mL) were added into each well, and cells were irradiated with 5 Gy X-ray after an hour of incubation. Cell supernatant was then collected from different time point (1, 2, 4, 24 hours) and tested in ATP 1step Luminescence Assay System, 100 mL ATP Assay Kit (PerkinElmer, US) following the manufacture's protocol. A 10-fold serial dilution series of ATP in culture medium (1 μM to 1 pM) were created to build up a standard curve and calculate the absolute amount of ATP in the supernatant. The luminescence was measured by a microplate reader (Synergy Mx, BioTeK).

HMGB1 (High mobility group box 1 protein) assay

CT26 Cells were seeded into 6-well plates at the density of 1×104 cells per well and incubated overnight. When the cells confluency reach 80%, CT26 cells were incubated together with 5-ALA (1 mg/mL) or redaporfin (10 μg/mL) in RPMI medium. Two hours later, NPs (100 μg/mL) were added into each well, and cells were irradiated with 5 Gy X-ray after an hour of incubation. The cells were further incubated for 24 hours and the HMGB1 levels were analyzed following the manufacture's protocol. The HMGB1 levels were quantified by a microplate reader (Synergy Mx, BioTeK) with 450 nm absorption.

In vivo therapy studies

Animal studies were performed according to a protocol (A2020 06-004-R1) approved by the Institutional Animal Care and Use Committee (IACUC) of the University of Georgia. The animals were maintained under pathogen-free conditions. CT26 tumors were established by subcutaneously injecting 2×10^5 cells in 50 μL PBS into the right flanks of 5-6-week old female BALB/c mice (Charles River). When tumor volume reached 50 mm^3, the animals were randomly divided into 6 groups (n = 5) and received the following treatments (Day 1): PBS only, PBS plus ionizing radiation (PBS + IR), CIZS@M-F plus irradiation (CIZS@M-F + IR), CIZS@M-F plus 5-ALA plus irradiation (CIZS@M-F + 5-ALA + IR), CIZS@M-F plus Redaporfin plus irradiation (CIZS@M-F + Redaporfin + IR), CIZS@M-F plus Redaporfin plus 5-ALA plus irradiation

(CIZS@M-F + 5-ALA + Redaporfin + IR). 5-ALA (50 mg kg^{-1} in PBS) and Redaporfin (20 mg kg^{-1} in PBS) was administered intraperitoneally. CIZS@M-F in PBS (1.25 mg kg^{-1}) were intratumorally injected 2 hours after the intraperitoneal injection. A 320 KV cabinet irradiator (X-RAD 320, Precision X-ray, Inc.) was used to irradiate (5 Gy) tumors 1 hour after CIZS@M-F administration, while the rest of the animal body was protected with lead. Animals underwent two additional treatment sessions on Days 3 and 5. Tumor size and body weight were inspected every 3 days. Tumor dimensions were measured with a caliper. Tumor volume was estimated by calculating $(\text{length})\times(\text{width})^2/2$. Animals were euthanized after 22 days. Tumors were dissected and sliced for H&E and Ki67 staining. Organs including the heart, spleen, liver, brain, intestine, kidney, and lung were also harvested for H&E staining.

Biodistribution studies

5-6 week-old female BALB/c mice (Charles River) were intravenously injected with CIZS@M-F (50 μL, 1.25 mg kg^{-1}) or PBS (control) *via* the tail vein. All mice were sacrificed after two weeks. Blood was collected through cardiac puncture for complete blood count (CBC), BUN, and ALT measurements. Major organs, including the heart, spleen, liver, brain, intestine, kidney, and lung were harvested. Half of the tissues were weighted, homogenized, and digested in hot nitric acid. Supernatants were subjected to ICP-MS analysis to measure tissue concentrations of cesium and iodine in tissues (μg/grams of tissue). The remaining tissues were fixed and sliced for H&E staining.

Safety Statement

No unexpected or unusually high safety hazards were encountered

Statistical analysis

All quantitative data were shown as mean ± SD. Statistical analysis was conducted using student's *t* or ANOVA test. *$p < 0.05$, **$p < 0.01$, ***$p < 0.001$.

4.3 Results and discussion

Synthesis and characterizations of CsI(CO_3, Na) nanoparticles

We started the reaction from a mixture of oleic acid and cesium carbonate in 1-octadecene. The mixture was then heated to 150 °C under argon gas and stayed there for 30 mins (Figure 1a). We then added oleylamine, 1,2-hexadecanediol, NaI and extra amount of $CsCO_3$ into the mixture as for doping. Limited amount of I_2 was then introduced 10 mins later. After reaction, we collected the products by centrifugation and redispersed them in hexane. According to TEM, the synthesized CsI(CO_3, Na) nanoparticles were cubic (Figure 1b) with an average size of 60.2 ± 5.2 nm. X-ray diffraction (XRD) confirmed that the nanoparticles were similar to undoped CsI and belonged to the Pm3m space group (No. 221, JCPDS#06-0311, Figure 1c).

Due to the high solubility of CsI(CO_3, Na) nanoparticles in an aqueous environment. We further imparted a layer of ZnS *via* seed-mediated growth to slow down its fast degradation. ZnS is a low-toxic, stable, and biodegradable material extensively utilized in bioimaging.[173] The resulting CsI(CO_3, Na)@ZnS nanoparticles were spherical in a layer of ZnS shell (Figure 1e). XPS analysis confirmed the existence of Cs, I, Zn, and S elements (Figure 1d). EDX also confirmed the presence of ZnS coating in the resulting nanoparticles (Figure 1f). XRD again identified characteristic peaks from CsI nanocrystals, and we did not observe apparent signals from ZnS coating due to the overwhelming signals from CsI (Figure 1c). We then studied the X-ray luminescence of CsI(CO_3, Na) nanoparticles. Fortunately, those nanoparticles displayed intense luminescence peaks at ~410 nm and ~510 nm with an intensity ratio of 2:3 (Figure 1g). The luminescence peaks overlapped well with the Soret band of PpIX and the absorption spectrum of Redaporfin (Figure 1g), suggesting the potential of utilizing our nanoparticles for multiplexing photosensitizers' activation.

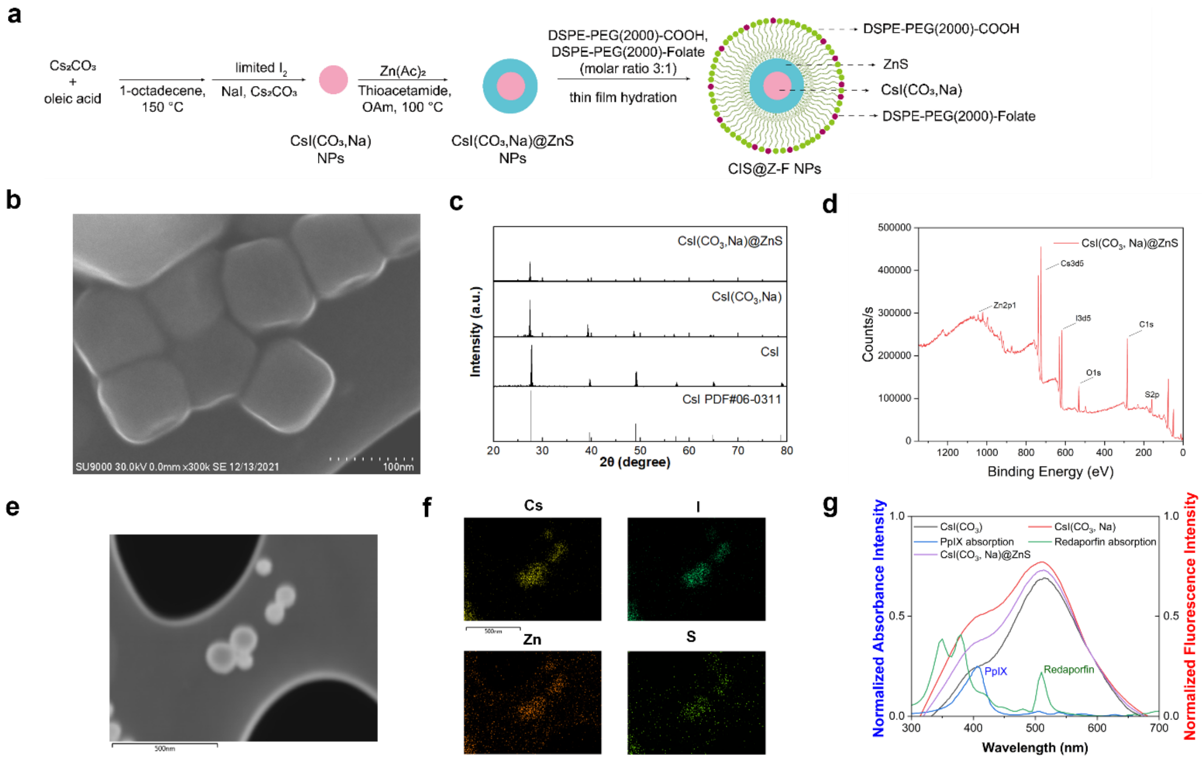

Figure 4.1 a) Synthetic route of CsI(CO_3, Na)@ZnS nanoparticles and its PEGylation. b) TEM image of CsI(CO_3, Na) nanoparticles. c) XRD of CsI(CO_3, Na) and CsI(CO_3, Na)@ZnS nanoparticles. d) XPS of CsI(CO_3, Na)@ZnS nanoparticles e) TEM image of CsI(CO_3, Na)@ZnS nanoparticles. f) EDS spectrum of CsI(CO_3, Na)@ZnS nanoparticles. g) X-ray induced luminescence from CsI(CO_3, Na) and CsI(CO_3) nanoparticles overlaps with absorption spectrum of PpIX and Redaporfin.

Stability and in solution evaluations of CsI(CO_3, Na)@ZnS nanoparticles

We further coated CsI(CO_3, Na)@ZnS nanoparticles with DSPE-PEG-COOH and DSPE-PEG-Folate (molar ratio 3:1) through thin-film hydration. The finalized CsI(CO_3, Na)@ZnS@DSPE-PEG-Folate nanoparticles are readily dispersed in aqueous solutions. Dynamic light scattering (DLS) showed that the average hydrodynamic size of our PEGylated nanoparticles was 132.1 ± 26.4 nm (Figure 2a). Besides, CsI(CO_3, Na)@ZnS nanoparticles without a phospholipid coating were 104.2 ± 12.9 nm (in hexane, Figure 2a), and CsI(CO_3, Na) nanoparticles were 87.6 ± 19.5 nm (in hexane, Figure 2a) respectively. Z-potential analysis found that CsI(CO_3, Na)@ZnS@DSPE-PEG-Folate were negatively charged (-62.17 mV, Figure 2b), and CsI(CO_3, Na)@DSPE-PEG-Folate nanoparticles were -59.01 mV.

We then studied the degradation of our finalized nanoparticles in PBS. The release profile was recorded under the guidance of an iodine electrode. Compared to uncoated CsI(Na) nanoparticles which release more than 90% iodine within 3 hours, our nanoparticles can be rather stable in PBS with only ~30% release after 24 hours (Figure 2c).

To further confirm the X-ray luminescence properties and its related energy conversion ability, nanoparticles were mixed with SOSG (5μM) or APF (5μM) in solution and irradiated with 5 Gy X-ray. Before irradiation, PpIX (1 mg/mL) or Redaporfin (10 μg/mL) was also introduced to provide a circumstance with multiplexing photosensitizers. After irradiation, we observed a significant luminescence increment from all those treatment groups (Figure 2d), which indicated the successful production of singlet oxygen after energy conversion. In addition, hydroxyl radicals were also generated after irradiation and that was evidenced by increased APF luminescence from our treated groups (Figure 2e).

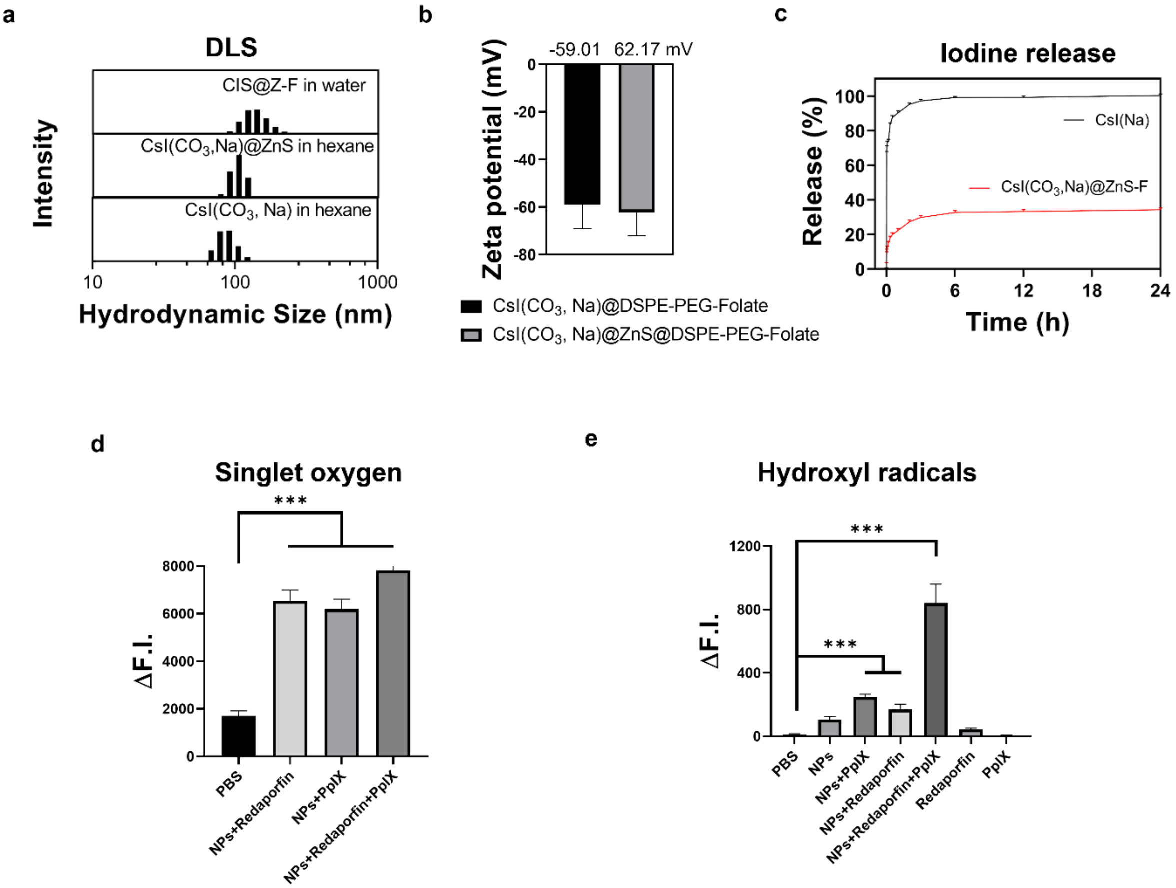

Figure 4.2 Stability and X-ray luminescence of CsI(CO_3, Na)@ZnS@DSPE-Folate nanoparticles (CIS@Z-F). a) DLS analysis of CsI(CO_3, Na), CsI(CO_3, Na)@ZnS, and CIS@Z-F nanoparticles. b) Zeta-potential analysis of CsI(CO_3, Na) @DSPE-PEG-F and CsI(CO_3, Na)@ZnS@DSPE-PEG-F. c) Iodine release from CsI(Na) and CIS@Z-F nanoparticles in PBS (pH 7.4). d) Singlet oxygen production under ionizing irradiation (IR, 5 Gy), measured with solutions containing CIS@Z-F with or without PpIX and Redaporfin, using SOSG (ex/em: 504/525 nm) as an indicator. The experiments were repeated in quintuplicates. ***, $p < 0.001$; ns, $p > 0.05$. e) Hydroxyl radical generations under ionizing irradiation (IR, 5 Gy), measured with solutions containing CIS@Z-F

with or without PpIX and Redaporfin, using APF (ex/em: 490/515 nm) as an indicator. The experiments were repeated in triplicates. ***, $p < 0.001$; ns, $p > 0.05$.

Evaluate X-PDT *in vitro* in CT26 cells treated with CIS@Z-F, 5-ALA, and Redaporfin

We first studied radical generations by incubating CT26 cells with CIS@Z-F nanoparticles, 5-ALA (1 mg/mL), or redaporfin (10 μg/mL) in RPMI medium. Compared to PBS only, nanoparticles themselves can stimulate the formation of singlet oxygens which is assumably due to the natural existence of PpIX in cancer cells' mitochondria (Figure 3a). The levels of singlet oxygens were further elevated when we exogenously introduced 5-ALA or Redaporfin. The highest singlet oxygen levels from the treatment group with both 5-ALA and Redaporfin manifested our hypothesis and proved the energy transfer process via nanoscale scintillators. Similar results were observed with H2DCFDA kit which was utilized for total ROS level quantification (Figure 3b). And that again proved that our nanoparticles can be excited by external X-ray irradiation and give off luminescence to stimulate nearby photosensitizers for a radical generation. Those generated radicals can finally lead to the cell death, which was evidenced by our viability study with ATP kit after irradiation (Figure 3c).

Because 5-ALA must be taken in and converted to PpIX for executing its functionality, we next investigated its conversion efficiency *in vitro* and *in vivo*. Briefly, we incubated 5-ALA together with CT26 cells in 6 well plates and extracted intracellular PpIX from different time points (Figure 3d). Intense luminescence 3 hours later after incubation indicated the significant 5-ALA transfer efficiency and the successful PpIX accumulation *in vitro*. We next intraperitoneally injected 5-ALA into CT26 tumor-bearing balb/c mice. After 2 hours, the control group showed no luminescence from the tumor area while the treatment group showed significant luminescence upon 640 nm excitation (Figure 3e). This find out is same as the previous reference and it indicated 3 hours can be a good time point for PpIX conversion[171]. Thus, we chose this time point for all our following studies.

Next, we evaluated cytosolic superoxide dismutase (SOD) and manganese-dependent superoxide dismutase (MnSOD) activities in cells after treatment. Significant increments of SOD and MnSOD activities were observed from the group treated with NPs + 5-ALA + Redaporfin+ IR (Figure 3f), indicating elevated ROS and corresponding cell response. Mitochondria membrane potential ($\Delta\Psi_m$) changes were then investigated and their changes after irradiation indicated the mitochondria-targeted activation (Figure 3g). The mitochondria damage from the treatment group then activated the apoptosis pathway and this was also evidenced by increased caspase-3 activities after irradiation (Figure 3h). The elevated ROS stress can also hamper the structure of DNA, proteins, or lipids. And the reduced red/green signals with our lipid peroxidation kit indicated the successful generation as well as accumulation of lipid peroxides after treatment (Figure 3i).

Besides 5-ALA oriented mitochondria damage and apoptosis, we also tested if the Redaporfin can induce the endoplasmic reticulum damage and trigger following immunogenic cell death. We initially tested the extracellular ATP concentration after our treatment and observed significant ATP accumulation. Compared to the control + IR group, the extracellular ATP concentration from NPs+ 5-ALA + Redaporfin + IR group was increased by 2.42 times after 2 hours (Figure 3j). We further investigated HMGB1 expression after the same treatment. And compared to the control alone, HMGB1 expression from NPs+ 5-ALA + Redaporfin + IR group was promoted by 2.24 times (Figure 3k). Both extracellular ATP and HMGB1 expressions were biomarkers for immunogenic cell death and our results indicated our nanoplatform can not only induce mitochondria damage but also endoplasmic reticulum damage.

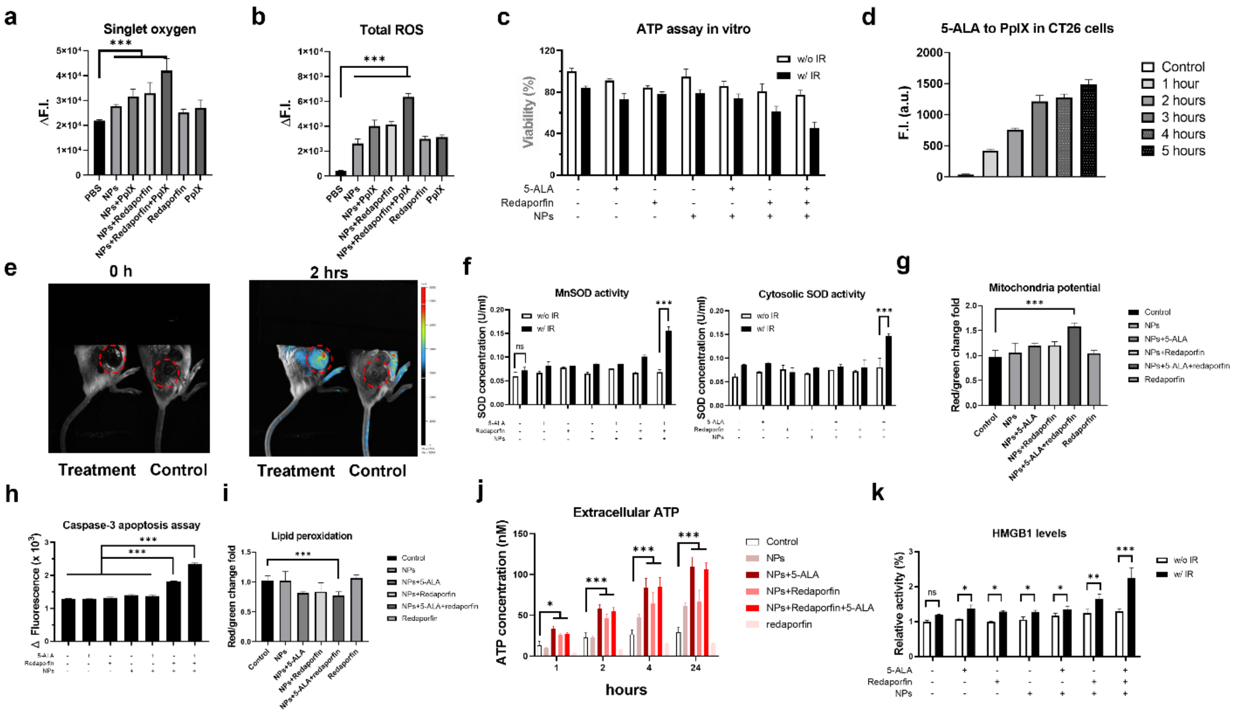

Figure 4.3 *In vitro* X-PDT with CIS@Z-F, 5-ALA, and Redaporfin, evaluated with CT26 cells. a-b) Impact of CIS@Z-F, 5-ALA, and Redaporfin on cellular oxidative stress. CT26 cells were incubated with CIS@Z-F (100 µg mL^{-1}), Redaporfin (10 µg mL^{-1}), and 5-ALA (1 mg mL^{-1}), or their combination, followed by IR (5 Gy). All experiments were repeated in quintuplicates. c) Cell viability, measured with ATP bioluminescence assay at 24 h. d) *In vitro* PpIX accumulation, measured by microplate reader (ex/em: 406/604 nm). e) *In vivo* PpIX accumulation on CT26-bearing balb/c mice, measured by 640 nm excitation with Newtown imaging system. f) Cytosol SOD and mitochondrial MnSOD activities, measured with Superoxide Dismutase Assay Kit. g) Mitochondrial membrane potentials (Ψ_m), measured with JC-1 assay. h) Caspase-3 activity, measured by microplate reader (ex/em: 488/530 nm). i) Lipid peroxidation, measured with C11-BIDOPY (ex/em: 488/510 nm) assay. j) Extracellular ATP concentrations, measured with ATP bioluminescence assay from different time points after 5 Gy X-ray irradiation. k) HMGB1 levels 24 hours after 5 Gy X-ray irradiation. *, $p < 0.05$; **, $p < 0.01$; ***, $p < 0.001$; ns, $p > 0.05$.

Evaluate X-PDT with CIS@Z-F and 5-ALA, and Redaporfin *in vivo*

We inoculated CT26 cells into the right flanks of 5-6-week female balc/c mice. When tumor volume reached 50 mm^3, we intraperitoneally (i.p.) administered 5-ALA (50 mg/kg) or Redaporfin (20 mg/kg). Two hours later, NPs (1.25 mg/Kg) or the same amount of PBS was intratumorally administrated. After another hour, we delivered 5 Gy of irradiation to the tumor site (Day 1), and the same progress was repeated on Day 3 and Day 5 (Figure 4a). Without treatment, animals from the control group reached an average tumor size of 797.78 mm^3 after 21 days. On the contrary, the average tumor sizes reached 388.77 mm^3 and 309.37 mm^3 for PBS + IR and NPs + IR groups, respectively. Fortunately, almost all mice from the three treatment groups have their tumors eradicated after 21 days, and that indicated our dual wavelength nanoparticles can be utilized as a remarkable tool against intracellular photosensitizer activation.

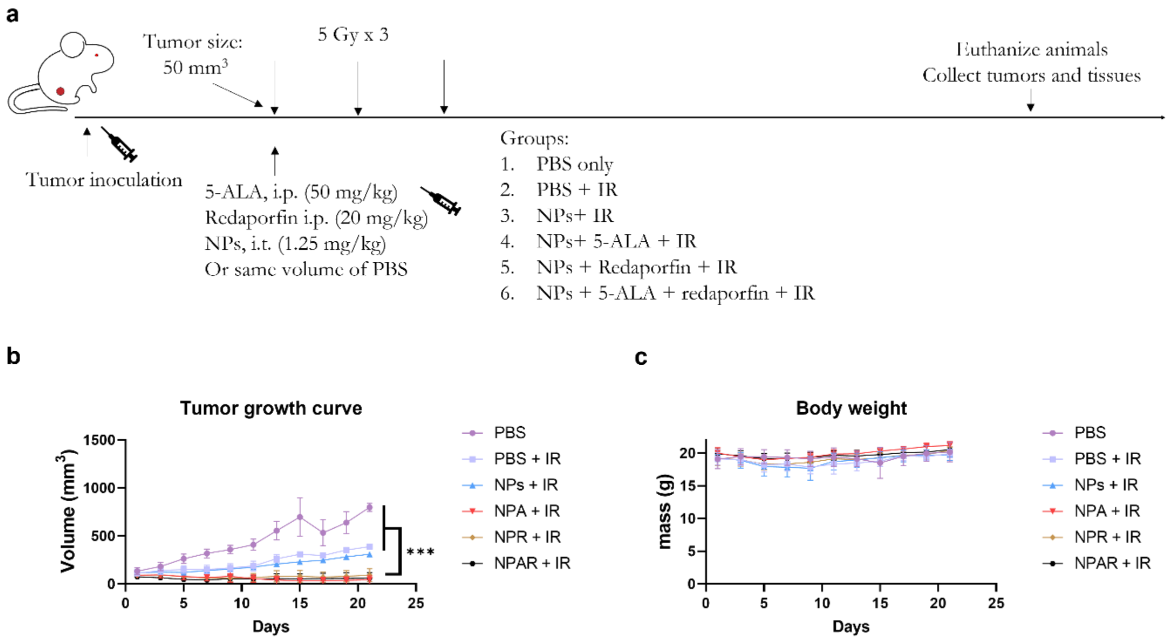

Figure 4.4 *In vivo* studies to evaluate the efficacy of X-PDT with CIS@Z-F, 5-ALA, and Redaporfin. Experiments were performed in CT26-tumor bearing balb/c mice. a) Scheme of experimental design. On Day 1, animals received one of the following regimens, including PBS only, PBS plus ionizing radiation (PBS+IR), nanoparticles with IR (NPs+IR), nanoparticles plus 5-ALA plus IR (NPs+5-ALA+IR), nanoparticles plus Redaporfin plus irradiation (NPs+Redaporfin+IR), and nanoparticles plus 5-ALA plus Redaporfin plus irradiation (NPs+5-ALA+Redaporfin+IR). 5-ALA (50 mg kg^{-1} in PBS) and Redaporfin (20 mg kg^{-1} in PBS) were i.p. administered, while nanoparticles in PBS (1.25 mg kg^{-1}) were intratumorally administered 2 hour after photosensitizer injections. IR (5 Gy) was applied to tumors 1 hour after nanoparticle administration. Two more sessions of treatment were given on Days 3 and 5. Animals were euthanized after 3 weeks or when a humane endpoint was reached. b) Tumor growth curves. ***, $p < 0.001$. c) Animal body weight curves.

4.4 Conclusion

Inspired by our previous CsI(Na) nanoparticles, here we successfully synthesized dual wavelength biodegradable CsI(CO_3, Na) nanoparticles via the wet method. The nanoparticles can produce both ~410 nm ultraviolet light and ~ 510 nm green light upon X-ray irradiation. We then chose a biocompatible material ZnS and successfully synthesized the core@shell CsI(CO_3, Na)@ZnS nanoparticles to slow down the inner hygroscopic nanoparticles from degradation. The nanoparticles were further modified via PEGylation with DSPE-PEG-Folate to enhance their cellular uptakes. *In vitro* studies with CT26 cells indicated the feasibility of our approach and the nanoparticles can be excited by an external X-ray source and stimulate nearby photosensitizers such as PpIX and Redaporfin. Aiding by those nanoparticles, photosensitizers were activated, and we observed elevated ROS stress *in vitro*. We also observed the following apoptosis and immunogenic death pathways after our treatment. Because both 5-ALA and Redaporfin have been approved by FDA for photodynamic therapy, our novel approach can surpass the imprisoned light penetration issue and significantly decrease the radiation dose needed for obtaining similar therapeutic efficacies. In the future, there will be more immunogenic cell death related assays conducted. And we will also explore the potential possibilities of DNA damage and radiation-compromised cell proliferative capabilities.

For proof-of-concept, we intratumorally injected our nanoparticles *in vivo* and noticed tumor eradication after our treatment. This approach can be further extended to other Folate-receptor positive cancer cell lines and even metastatic cell lines. In the future, safety studies will be tested to verify the biocompatibility of our nanoplatform. Dendritic cells related immunogenic cell death will also be confirmed *in vitro* and *in vivo*.

CHAPTER 5

CONCLUSION AND FUTURE PLAN

Radiosensitizing reagents have attracted a lot of attention due to their therapeutic efficacy and their synergistic effect for curtailing radiation dosage. With this in mind, numerous novel nanoplatforms have been developed and utilized for radiation therapy. However, finding a resolution to eradicate the tumor site while generating minimal cytotoxicity is not always easy. Here we reported ultrathin gold nanowires as one promising radiosensitizer for radiation therapy. Our gold nanowires with a high surface ratio can be favorably taken by cancer cell lines. Besides, the nanoparticles only contain low toxic and stable gold metals and could leave the body after irradiation by themselves. Our studies with 4T1 breast cancer cells and balb/c mice envisioned their superior therapeutic performance compared to conventional gold nanospheres, providing a new insight for clinical transition.

Moreover, we developed two nanoplatforms based on CsI(Na) nanoscale scintillators and the photosensitizer 5-ALA. This is a milestone in the era of radiodynamic therapy and we successfully averted the scintillator-photosensitizer nanoconjugate and followed tedious manufacturing process. For instance, in chapter 3 we substantiated that photosensitizers underneath 3 cm pork can still be activated by our nanoparticles and generate singlet oxygens. This concept was further confirmed by our *in vivo* studies with 4T1 bearing balb/c mice. Besides this, in chapter 4 we optimized our nanoplatform and confirmed the killing effect can be expanded to other organelles such as the endoplasmic reticulum, and other cancer cell lines such as CT26 colon cells. In the future, we will explore the efficacy of nanoplatforms against metastatic cell lines and explore whether the immune response is actively involved during our radiodynamic therapy.

REFERENCES

CHAPTER 1:

1. Fan W, Tang W, Lau J, Shen Z, Xie J, Shi J, Chen X: **Breaking the Depth Dependence by Nanotechnology-Enhanced X-Ray-Excited Deep Cancer Theranostics**. *Adv Mater* 2019, **31**(12):e1806381.
2. Fan W, Huang P, Chen X: **Overcoming the Achilles' heel of photodynamic therapy**. *Chem Soc Rev* 2016, **45**(23):6488-6519.
3. Kamkaew A, Chen F, Zhan Y, Majewski RL, Cai W: **Scintillating Nanoparticles as Energy Mediators for Enhanced Photodynamic Therapy**. *ACS Nano* 2016, **10**(4):3918-3935.
4. Cline B, Delahunty I, Xie J: **Nanoparticles to mediate X-ray-induced photodynamic therapy and Cherenkov radiation photodynamic therapy**. *Wiley Interdiscip Rev Nanomed Nanobiotechnol* 2019, **11**(2):e1541.
5. Ran C, Zhang Z, Hooker J, Moore A: **In vivo photoactivation without "light": use of Cherenkov radiation to overcome the penetration limit of light**. *Mol Imaging Biol* 2012, **14**(2):156-162.
6. Shaffer TM, Pratt EC, Grimm J: **Utilizing the power of Cerenkov light with nanotechnology**. *Nat Nanotechnol* 2017, **12**(2):106-117.
7. Pratt EC, Shaffer TM, Grimm J: **Nanoparticles and Radiotracers: Advances toward RadioNanomedicine**. *Wiley Interdiscip Rev Nanomed Nanobiotechnol* 2016, **8**(6):872-890.

8. Zhang Y, Hao Y, Chen S, Xu M: **Photodynamic Therapy of Cancers With Internal Light Sources: Chemiluminescence, Bioluminescence, and Cerenkov Radiation**. *Front Chem* 2020, **8**:770.
9. Kavadiya S, Biswas P: **Design of Cerenkov Radiation-Assisted Photoactivation of TiO2 Nanoparticles and Reactive Oxygen Species Generation for Cancer Treatment**. *J Nucl Med* 2019, **60**(5):702-709.
10. Dothager RS, Goiffon RJ, Jackson E, Harpstrite S, Piwnica-Worms D: **Cerenkov radiation energy transfer (CRET) imaging: a novel method for optical imaging of PET isotopes in biological systems**. *PLoS One* 2010, **5**(10):e13300.
11. Chen W, Zhang J: **Using nanoparticles to enable simultaneous radiation and photodynamic therapies for cancer treatment**. *J Nanosci Nanotechnol* 2006, **6**(4):1159-1166.
12. Lecoq P: **Scintillation Detectors for Charged Particles and Photons**. In: *Particle Physics Reference Library: Volume 2: Detectors for Particles and Radiation.* edn. Edited by Fabjan CW, Schopper H. Cham: Springer International Publishing; 2020: 45-89.
13. Kwiatkowski S, Knap B, Przystupski D, Saczko J, Kedzierska E, Knap-Czop K, Kotlinska J, Michel O, Kotowski K, Kulbacka J: **Photodynamic therapy - mechanisms, photosensitizers and combinations**. *Biomed Pharmacother* 2018, **106**:1098-1107.
14. Takahashi J, Misawa M: **Analysis of Potential Radiosensitizing Materials for X-Ray-Induced Photodynamic Therapy**. *NanoBiotechnology* 2007, **3**(2):116-126.
15. Morgan NY, Kramer-Marek G, Smith PD, Camphausen K, Capala J: **Nanoscintillator conjugates as photodynamic therapy-based radiosensitizers: calculation of required physical parameters**. *Radiat Res* 2009, **171**(2):236-244.

16. A. H. Kayal YM, C. Jaccard, and I. Rossel: **Luminescence processes in CsI doped with Na+ and K+ ions**. *Solid State Commun* 1980, **35**(6):457-460.

17. Giokaris N, Loudos G, Maintas D, Karabarbounis A, Lembesi M, Spanoudaki V, Stiliaris E, Boukis S, Sakellios N, Karakatsanis N *et al*: **Comparison of CsI(Tl) and CsI(Na) partially slotted crystals for high-resolution SPECT imaging**. *Nuclear Instruments and Methods in Physics Research Section A: Accelerators, Spectrometers, Detectors and Associated Equipment* 2006, **569**(2):185-187.

18. Dujardin C, Amans D, Belsky A, Chaput F, Ledoux G, Pillonnet A: **Luminescence and Scintillation Properties at the Nanoscale**. *IEEE Transactions on Nuclear Science* 2010, **57**(3):1348-1354.

19. Ledoux G, Mercier B, Louis C, Dujardin C, Tillement O, Perriat P: **Synthesis and optical characterization of Gd2O3:Eu3+ nanocrystals: surface states and VUV excitation**. *Radiation Measurements* 2004, **38**(4-6):763-766.

20. Zhu R-y: **Radiation damage in scintillating crystals**. *Nuclear Instruments and Methods in Physics Research Section A: Accelerators, Spectrometers, Detectors and Associated Equipment* 1998, **413**(2):297-311.

21. Annenkov AN, Auffray E, Chipaux R, Drobychev GY, Fedorov AA, Géléoc M, Golubev NA, Korzhik MV, Lecoq P, Lednev AA *et al*: **Systematic study of the short-term instability of PbWO4 scintillator parameters under irradiation**. *Radiation Measurements* 1998, **29**(1):27-38.

22. Agarwal ML, Larkin HE, Zaidi SI, Mukhtar H, Oleinick NL: **Phospholipase activation triggers apoptosis in photosensitized mouse lymphoma cells**. *Cancer Res* 1993, **53**(24):5897-5902.

23. Castano AP, Demidova TN, Hamblin MR: **Mechanisms in photodynamic therapy: part one—photosensitizers, photochemistry and cellular localization**. *Photodiagnosis and Photodynamic Therapy* 2004, **1**(4):279-293.

24. Castano AP, Mroz P, Hamblin MR: **Photodynamic therapy and anti-tumour immunity**. *Nat Rev Cancer* 2006, **6**(7):535-545.

25. Wang GD, Nguyen HT, Chen H, Cox PB, Wang L, Nagata K, Hao Z, Wang A, Li Z, Xie J: **X-Ray Induced Photodynamic Therapy: A Combination of Radiotherapy and Photodynamic Therapy**. *Theranostics* 2016, **6**(13):2295-2305.

26. Ni K, Lan G, Veroneau SS, Duan X, Song Y, Lin W: **Nanoscale metal-organic frameworks for mitochondria-targeted radiotherapy-radiodynamic therapy**. *Nat Commun* 2018, **9**(1):4321.

27. Buytaert E, Dewaele M, Agostinis P: **Molecular effectors of multiple cell death pathways initiated by photodynamic therapy**. *Biochim Biophys Acta* 2007, **1776**(1):86-107.

28. Chen M-H, Jenh Y-J, Wu S-K, Chen Y-S, Hanagata N, Lin F-H: **Non-invasive Photodynamic Therapy in Brain Cancer by Use of Tb(3+)-Doped LaF(3) Nanoparticles in Combination with Photosensitizer Through X-ray Irradiation: A Proof-of-Concept Study**. *Nanoscale research letters* 2017, **12**(1):62-62.

29. Tang Y, Hu J, Elmenoufy AH, Yang X: **Highly Efficient FRET System Capable of Deep Photodynamic Therapy Established on X-ray Excited Mesoporous LaF3:Tb Scintillating Nanoparticles**. *ACS Appl Mater Interfaces* 2015, **7**(22):12261-12269.

30. Zhang C, Zhao K, Bu W, Ni D, Liu Y, Feng J, Shi J: **Marriage of scintillator and semiconductor for synchronous radiotherapy and deep photodynamic therapy with diminished oxygen dependence**. *Angew Chem Int Ed Engl* 2015, **54**(6):1770-1774.

31. Bulin A-L, Truillet C, Chouikrat R, Lux F, Frochot C, Amans D, Ledoux G, Tillement O, Perriat P, Barberi-Heyob M *et al*: **X-ray-Induced Singlet Oxygen Activation with Nanoscintillator-Coupled Porphyrins**. *The Journal of Physical Chemistry C* 2013, **117**(41):21583-21589.

32. Scaffidi JP, Gregas MK, Lauly B, Zhang Y, Vo-Dinh T: **Activity of Psoralen-Functionalized Nanoscintillators against Cancer Cells upon X-ray Excitation**. *ACS Nano* 2011, **5**(6):4679-4687.

33. Martynenko IV, Kuznetsova VA, Orlova capital A C, Kanaev PA, Maslov VG, Loudon A, Zaharov V, Parfenov P, Gun'ko YK, Baranov AV *et al*: **Chlorin e6-ZnSe/ZnS quantum dots based system as reagent for photodynamic therapy**. *Nanotechnology* 2015, **26**(5):055102.

34. Ma L, Zou X, Bui B, Chen W, Song KH, Solberg T: **X-ray excited ZnS:Cu,Co afterglow nanoparticles for photodynamic activation**. *Applied Physics Letters* 2014, **105**(1).

35. Sadjadpour S, Safarian S, Zargar SJ, Sheibani N: **Antiproliferative effects of ZnO, ZnO-MTCP, and ZnO-CuMTCP nanoparticles with safe intensity UV and X-ray irradiation**. *Biotechnol Appl Biochem* 2016, **63**(1):113-124.

36. Ni K, Lan G, Lin W: **Nanoscale Metal-Organic Frameworks Generate Reactive Oxygen Species for Cancer Therapy**. *ACS Cent Sci* 2020, **6**(6):861-868.

37. Wang C, Volotskova O, Lu K, Ahmad M, Sun C, Xing L, Lin W: **Synergistic assembly of heavy metal clusters and luminescent organic bridging ligands in metal-organic frameworks for highly efficient X-ray scintillation**. *J Am Chem Soc* 2014, **136**(17):6171-6174.

38. Wang S, Mamedova N, Kotov NA, Chen W, Studer J: **Antigen/Antibody Immunocomplex from CdTe Nanoparticle Bioconjugates**. *Nano Letters* 2002, **2**(8):817-822.

39. Liu Y, Chen W, Wang S, Joly AG, Westcott S, Woo BK: **X-ray luminescence of LaF3:Tb3+ and LaF3:Ce3+,Tb3+ water-soluble nanoparticles**. *Journal of Applied Physics* 2008, **103**(6).

40. Kaščáková S, Giuliani A, Lacerda S, Pallier A, Mercère P, Tóth É, Réfrégiers M: **X-ray-induced radiophotodynamic therapy (RPDT) using lanthanide micelles: Beyond depth limitations**. *Nano Research* 2015, **8**(7):2373-2379.

41. Wang H, Lv B, Tang Z, Zhang M, Ge W, Liu Y, He X, Zhao K, Zheng X, He M *et al*: **Scintillator-Based Nanohybrids with Sacrificial Electron Prodrug for Enhanced X-ray-Induced Photodynamic Therapy**. *Nano Lett* 2018, **18**(9):5768-5774.

42. Dasari S, Tchounwou PB: **Cisplatin in cancer therapy: molecular mechanisms of action**. *Eur J Pharmacol* 2014, **740**:364-378.

43. Chen H, Sun X, Wang GD, Nagata K, Hao Z, Wang A, Li Z, Xie J, Shen B: **LiGa5O8:Cr-based theranostic nanoparticles for imaging-guided X-ray induced photodynamic therapy of deep-seated tumors**. *Mater Horiz* 2017, **4**(6):1092-1101.

44. Sun W, Shi T, Luo L, Chen X, Lv P, Lv Y, Zhuang Y, Zhu J, Liu G, Chen X *et al*: **Monodisperse and Uniform Mesoporous Silicate Nanosensitizers Achieve Low-Dose**

X-Ray-Induced Deep-Penetrating Photodynamic Therapy. *Adv Mater* 2019, **31**(16):e1808024.

45. Yang CC, Tsai MH, Li KY, Hou CH, Lin FH: **Carbon-Doped TiO2 Activated by X-Ray Irradiation for the Generation of Reactive Oxygen Species to Enhance Photodynamic Therapy in Tumor Treatment**. *Int J Mol Sci* 2019, **20**(9).

46. Lu K, He C, Guo N, Chan C, Ni K, Weichselbaum RR, Lin W: **Chlorin-Based Nanoscale Metal-Organic Framework Systemically Rejects Colorectal Cancers via Synergistic Photodynamic Therapy and Checkpoint Blockade Immunotherapy**. *J Am Chem Soc* 2016, **138**(38):12502-12510.

47. Lu K, He C, Guo N, Chan C, Ni K, Lan G, Tang H, Pelizzari C, Fu Y-X, Spiotto MT *et al*: **Low-dose X-ray radiotherapy–radiodynamic therapy via nanoscale metal–organic frameworks enhances checkpoint blockade immunotherapy**. *Nature Biomedical Engineering* 2018, **2**(8):600-610.

48. Zhang Y, Wang F, Liu C, Wang Z, Kang L, Huang Y, Dong K, Ren J, Qu X: **Nanozyme Decorated Metal-Organic Frameworks for Enhanced Photodynamic Therapy**. *ACS Nano* 2018, **12**(1):651-661.

49. Liu J, Yang Y, Zhu W, Yi X, Dong Z, Xu X, Chen M, Yang K, Lu G, Jiang L *et al*: **Nanoscale metal-organic frameworks for combined photodynamic & radiation therapy in cancer treatment**. *Biomaterials* 2016, **97**:1-9.

50. Zhu W, Yang Y, Jin Q, Chao Y, Tian L, Liu J, Dong Z, Liu Z: **Two-dimensional metal-organic-framework as a unique theranostic nano-platform for nuclear imaging and chemo-photodynamic cancer therapy**. *Nano Research* 2019, **12**(6):1307-1312.

51. Lan G, Ni K, Veroneau SS, Luo T, You E, Lin W: **Nanoscale Metal-Organic Framework Hierarchically Combines High-Z Components for Multifarious Radio-Enhancement**. *J Am Chem Soc* 2019, **141**(17):6859-6863.

52. Ni K, Lan G, Chan C, Duan X, Guo N, Veroneau SS, Weichselbaum RR, Lin W: **Ultrathin Metal-Organic-Layer Mediated Radiotherapy-Radiodynamic Therapy**. *Matter* 2019, **1**(5):1331-1353.

53. Lan G, Ni K, Xu R, Lu K, Lin Z, Chan C, Lin W: **Nanoscale Metal-Organic Layers for Deeply Penetrating X-ray-Induced Photodynamic Therapy**. *Angew Chem Int Ed Engl* 2017, **56**(40):12102-12106.

54. Neufeld MJ, Lutzke A, Pratx G, Sun C: **High-Z Metal-Organic Frameworks for X-ray Radiation-Based Cancer Theranostics**. *Chemistry* 2021, **27**(10):3229-3237.

55. Ni K, Lan G, Chan C, Quigley B, Lu K, Aung T, Guo N, La Riviere P, Weichselbaum RR, Lin W: **Nanoscale metal-organic frameworks enhance radiotherapy to potentiate checkpoint blockade immunotherapy**. *Nat Commun* 2018, **9**(1):2351.

56. Clement S, Deng W, Camilleri E, Wilson BC, Goldys EM: **X-ray induced singlet oxygen generation by nanoparticle-photosensitizer conjugates for photodynamic therapy: determination of singlet oxygen quantum yield**. *Sci Rep* 2016, **6**:19954.

57. Niedre MJ, Secord AJ, Patterson MS, Wilson BC: **In Vitro Tests of the Validity of Singlet Oxygen Luminescence Measurements as a Dose Metric in Photodynamic Therapy**. *Cancer Research* 2003, **63**(22):7986.

58. Bakhmetyev VV, Lebedev LA, Vlasenko AB, Bogdanov SP, Sovestnov AE, Minakova TS, Minakova LY, Sychov MM: **Luminescent Materials on the Basis of Yttrium**

Oxide and Yttrium Aluminum Garnet Used for Photodynamic Therapy. *Key Engineering Materials* 2015, **670**:232-238.

59. Bakhmetyev VV, Minakova TS, Mjakin SV, Lebedev LA, Vlasenko AB, Nikandrova AA, Ekimova IA, Eremina NS, Sychov MM, Ringuede A: **Synthesis and surface characterization of nanosized Y2O3:Eu and YAG:Eu luminescent phosphors which are useful in photodynamic therapy of cancer**. *European Journal of Nanomedicine* 2016, **8**(4).

60. Chen H, Wang GD, Chuang YJ, Zhen Z, Chen X, Biddinger P, Hao Z, Liu F, Shen B, Pan Z *et al*: **Nanoscintillator-mediated X-ray inducible photodynamic therapy for in vivo cancer treatment**. *Nano Lett* 2015, **15**(4):2249-2256.

61. Rossi F, Bedogni E, Bigi F, Rimoldi T, Cristofolini L, Pinelli S, Alinovi R, Negri M, Dhanabalan SC, Attolini G *et al*: **Porphyrin conjugated SiC/SiOx nanowires for X-ray-excited photodynamic therapy**. *Scientific Reports* 2015, **5**(1):7606.

62. Oktyabrsky S, Yakimov M, Tokranov V, Murat P: **Integrated Semiconductor Quantum Dot Scintillation Detector: Ultimate Limit for Speed and Light Yield**. *IEEE Transactions on Nuclear Science* 2016, **63**(2):656-663.

63. Gupta SK, Mao Y: **Recent advances, challenges, and opportunities of inorganic nanoscintillators**. *Frontiers of Optoelectronics* 2020, **13**(2):156-187.

64. Dujardin C, Auffray E, Bourret-Courchesne E, Dorenbos P, Lecoq P, Nikl M, Vasil'ev AN, Yoshikawa A, Zhu RY: **Needs, Trends, and Advances in Inorganic Scintillators**. *IEEE Transactions on Nuclear Science* 2018, **65**(8):1977-1997.

65. Liu B, Wu Q, Zhu Z, Cheng C, Gu M, Xu J, Chen H, Liu J, Chen L, Zhang Z *et al*: **Directional emission of quantum dot scintillators controlled by photonic crystals**. *Applied Physics Letters* 2017, **111**(8).

66. Lemon CM, Karnas E, Bawendi MG, Nocera DG: **Two-photon oxygen sensing with quantum dot-porphyrin conjugates**. *Inorg Chem* 2013, **52**(18):10394-10406.

CHAPTER 2:

1. Barker HE, Paget JT, Khan AA, Harrington KJ: **The tumour microenvironment after radiotherapy: mechanisms of resistance and recurrence**. *Nat Rev Cancer* 2015, **15**(7):409-425.
2. Wang JS, Wang HJ, Qian HL: **Biological effects of radiation on cancer cells**. *Mil Med Res* 2018, **5**(1):20.
3. Bentzen SM: **Preventing or reducing late side effects of radiation therapy: radiobiology meets molecular pathology**. *Nat Rev Cancer* 2006, **6**(9):702-713.
4. Thomas CT, Ammar A, Farrell JJ, Elsaleh H: **Radiation modifiers: treatment overview and future investigations**. *Hematol Oncol Clin North Am* 2006, **20**(1):119-139.
5. Retif P, Pinel S, Toussaint M, Frochot C, Chouikrat R, Bastogne T, Barberi-Heyob M: **Nanoparticles for Radiation Therapy Enhancement: the Key Parameters**. *Theranostics* 2015, **5**(9):1030-1044.
6. Retif P, Pinel S, Toussaint M, Frochot C, Chouikrat R, Bastogne T, Barberi-Heyob M: **Nanoparticles for radiation therapy enhancement: the key parameters**. *Theranostics* 2015, **5**(9):1030.
7. Shrestha S, Cooper LN, Andreev OA, Reshetnyak YK, Antosh MP: **Gold nanoparticles for radiation enhancement in vivo**. *Jacobs journal of radiation oncology* 2016, **3**(1).
8. Rosa S, Connolly C, Schettino G, Butterworth KT, Prise KM: **Biological mechanisms of gold nanoparticle radiosensitization**. *Cancer nanotechnology* 2017, **8**(1):2.

9. Schuemann J, Berbeco R, Chithrani DB, Cho SH, Kumar R, McMahon SJ, Sridhar S, Krishnan S: **Roadmap to clinical use of gold nanoparticles for radiation sensitization**. *International Journal of Radiation Oncology* Biology* Physics* 2016, **94**(1):189-205.

10. Le Tourneau C, Moreno V, Salas S, Mirabel X, Calvo E, Doger B, Florescu C, Thariat J, Fijuth J, Rutkowski T: **Hafnium oxide nanoparticles NBTXR3 activated by radiotherapy as a new therapeutic option for elderly/frail HNSCC patients**. In.: American Society of Clinical Oncology; 2019.

11. Maggiorella L, Barouch G, Devaux C, Pottier A, Deutsch E, Bourhis J, Borghi E, Levy L: **Nanoscale radiotherapy with hafnium oxide nanoparticles**. *Future oncology* 2012, **8**(9):1167-1181.

12. Bonvalot S, Rutkowski PL, Thariat J, Carrère S, Ducassou A, Sunyach M-P, Agoston P, Hong A, Mervoyer A, Rastrelli M: **NBTXR3, a first-in-class radioenhancer hafnium oxide nanoparticle, plus radiotherapy versus radiotherapy alone in patients with locally advanced soft-tissue sarcoma (Act. In. Sarc): a multicentre, phase 2–3, randomised, controlled trial**. *The Lancet Oncology* 2019, **20**(8):1148-1159.

13. Shrestha S, Cooper LN, Andreev OA, Reshetnyak YK, Antosh MP: **Gold Nanoparticles for Radiation Enhancement in Vivo**. *Jacobs J Radiat Oncol* 2016, **3**(1).

14. Cooper DR, Bekah D, Nadeau JL: **Gold nanoparticles and their alternatives for radiation therapy enhancement**. *Front Chem* 2014, **2**.

15. Cooper DR, Bekah D, Nadeau JL: **Gold nanoparticles and their alternatives for radiation therapy enhancement**. *Frontiers in chemistry* 2014, **2**:86.

16. Song G, Cheng L, Chao Y, Yang K, Liu Z: **Emerging nanotechnology and advanced materials for cancer radiation therapy**. *Advanced Materials* 2017, **29**(32):1700996.

17. Her S, Jaffray DA, Allen C: **Gold nanoparticles for applications in cancer radiotherapy: Mechanisms and recent advancements**. *Advanced drug delivery reviews* 2017, **109**:84-101.

18. Xu W, Luo T, Li P, Zhou C, Cui D, Pang B, Ren Q, Fu S: **RGD-conjugated gold nanorods induce radiosensitization in melanoma cancer cells by downregulating αvβ3 expression**. *International journal of nanomedicine* 2012, **7**:915.

19. Ma N, Wu F-G, Zhang X, Jiang Y-W, Jia H-R, Wang H-Y, Li Y-H, Liu P, Gu N, Chen Z: **Shape-dependent radiosensitization effect of gold nanostructures in cancer radiotherapy: comparison of gold nanoparticles, nanospikes, and nanorods**. *ACS applied materials & interfaces* 2017, **9**(15):13037-13048.

20. Zhao N, Yang Z, Li B, Meng J, Shi Z, Li P, Fu S: **RGD-conjugated mesoporous silica-encapsulated gold nanorods enhance the sensitization of triple-negative breast cancer to megavoltage radiation therapy**. *International journal of nanomedicine* 2016, **11**:5595.

21. Yu Y, Cui F, Sun JW, Yang PD: **Atomic Structure of Ultrathin Gold Nanowires**. *Nano Lett* 2016, **16**(5):3078-3084.

22. Peng S, Lee Y, Wang C, Yin H, Dai S, Sun S: **A facile synthesis of monodisperse Au nanoparticles and their catalysis of CO oxidation**. *Nano research* 2008, **1**(3):229-234.

23. Tzelepi K, Garcia CE, Williams P, Golding J: **Galactose: PEGamine coated gold nanoparticles adhere to filopodia and cause extrinsic apoptosis**. *Nanoscale Advances* 2019, **1**(2):807-816.

24. Carnovale C, Bryant G, Shukla R, Bansal V: **Identifying trends in gold nanoparticle toxicity and uptake: size, shape, capping ligand, and biological corona**. *ACS omega* 2019, **4**(1):242-256.

25. Choi SY, Jang SH, Park J, Jeong S, Park JH, Ock KS, Lee K, Yang SI, Joo S-W, Ryu PD: **Cellular uptake and cytotoxicity of positively charged chitosan gold nanoparticles in human lung adenocarcinoma cells**. *J Nanopart Res* 2012, **14**(12):1234.

26. Moran CH, Wainerdi SM, Cherukuri TK, Kittrell C, Wiley BJ, Nicholas NW, Curley SA, Kanzius JS, Cherukuri P: **Size-dependent joule heating of gold nanoparticles using capacitively coupled radiofrequency fields**. *Nano Research* 2009, **2**(5):400-405.

27. Cardinal J, Klune JR, Chory E, Jeyabalan G, Kanzius JS, Nalesnik M, Geller DA: **Noninvasive radiofrequency ablation of cancer targeted by gold nanoparticles**. *Surgery* 2008, **144**(2):125-132.

28. Hwang S, Nam J, Jung S, Song J, Doh H, Kim S: **Gold nanoparticle-mediated photothermal therapy: current status and future perspective**. *Nanomedicine* 2014, **9**(13):2003-2022.

29. Riley RS, Day ES: **Gold nanoparticle‐mediated photothermal therapy: applications and opportunities for multimodal cancer treatment**. *Wiley Interdisciplinary Reviews: Nanomedicine and Nanobiotechnology* 2017, **9**(4):e1449.

CHAPTER 3:

1. Dolmans DEJGJ, Fukumura D, Jain RK: **Photodynamic therapy for cancer**. *Nature Reviews Cancer* 2003, **3**(5):380-387.

2. Van Straten D, Mashayekhi V, De Bruijn HS, Oliveira S, Robinson DJ: **Oncologic Photodynamic Therapy: Basic Principles, Current Clinical Status and Future Directions**. *Cancers* 2017, **9**(2):19.

3. Allison RR, Downie GH, Cuenca R, Hu X-H, Childs CJH, Sibata CH: **Photosensitizers in clinical PDT**. *Photodiagnosis and Photodynamic Therapy* 2004, **1**(1):27-42.

4. Lovell JF, Liu TWB, Chen J, Zheng G: **Activatable Photosensitizers for Imaging and Therapy**. *Chemical Reviews* 2010, **110**(5):2839-2857.

5. Lim C-K, Heo J, Shin S, Jeong K, Seo YH, Jang W-D, Park CR, Park SY, Kim S, Kwon IC: **Nanophotosensitizers toward advanced photodynamic therapy of Cancer**. *Cancer Letters* 2013, **334**(2):176-187.

6. Mallidi S, Anbil S, Bulin A-L, Obaid G, Ichikawa M, Hasan T: **Beyond the Barriers of Light Penetration: Strategies, Perspectives and Possibilities for Photodynamic Therapy**. *Theranostics* 2016, **6**(13):2458-2487.

7. Lan M, Zhao S, Liu W, Lee C-S, Zhang W, Wang P: **Photosensitizers for Photodynamic Therapy**. *Advanced Healthcare Materials* 2019, **8**(13):1900132.

8. Yano S, Hirohara S, Obata M, Hagiya Y, Ogura S-i, Ikeda A, Kataoka H, Tanaka M, Joh T: **Current states and future views in photodynamic therapy**. *Journal of Photochemistry and Photobiology C: Photochemistry Reviews* 2011, **12**(1):46-67.

9. Zhou S, Li D, Lee C, Xie J: **Nanoparticle Phototherapy in the Era of Cancer Immunotherapy**. *Trends in Chemistry* 2020, **2**(12):1082-1095.

10. Yang X, Zhang W, Jiang W, Kumar A, Zhou S, Cao Z, Zhan S, Yang W, Liu R, Teng Y *et al*: **Nanoconjugates to enhance PDT-mediated cancerimmunotherapy by targeting the indoleamine-2,3-dioxygenase pathway**. *Journal of Nanobiotechnology* 2021, **19**(1):182.

11. Luo D, Carter KA, Miranda D, Lovell JF: **Chemophototherapy: An Emerging Treatment Option for Solid Tumors**. *Advanced Science* 2017, **4**(1):1600106.

12. Liu Z, Xie Z, Li W, Wu X, Jiang X, Li G, Cao L, Zhang D, Wang Q, Xue P *et al*: **Photodynamic immunotherapy of cancers based on nanotechnology: recent advances and future challenges**. *Journal of Nanobiotechnology* 2021, **19**(1):160.

13. Wilson BC: **Photodynamic therapy for cancer: principles**. *Can J Gastroenterol* 2002, **16**(6):393-396.

14. Wang GD, Nguyen HT, Chen H, Cox PB, Wang L, Nagata K, Hao Z, Wang A, Li Z, Xie J: **X-Ray Induced Photodynamic Therapy: A Combination of Radiotherapy and Photodynamic Therapy**. *Theranostics* 2016, **6**(13):2295-2305.

15. Fan W, Huang P, Chen X: **Overcoming the Achilles' heel of photodynamic therapy**. *Chem Soc Rev* 2016, **45**(23):6488-6519.

16. Chen X, Song J, Chen X, Yang H: **X-ray-activated nanosystems for theranostic applications**. *Chem Soc Rev* 2019, **48**(11):3073-3101.

17. Larue L, Ben Mihoub A, Youssef Z, Colombeau L, Acherar S, André JC, Arnoux P, Baros F, Vermandel M, Frochot C: **Using X-rays in photodynamic therapy: an overview**. *Photochem Photobiol Sci* 2018, **17**(11):1612-1650.

18. Cline B, Delahunty I, Xie J: **Nanoparticles to mediate X-ray-induced photodynamic therapy and Cherenkov radiation photodynamic therapy**. *Wiley Interdiscip Rev Nanomed Nanobiotechnol* 2019, **11**(2):e1541.

19. Fan W, Tang W, Lau J, Shen Z, Xie J, Shi J, Chen X: **Breaking the Depth Dependence by Nanotechnology-Enhanced X-Ray-Excited Deep Cancer Theranostics**. *Adv Mater* 2019, **31**(12):e1806381.

20. Sun W, Zhou Z, Pratx G, Chen X, Chen H: **Nanoscintillator-Mediated X-Ray Induced Photodynamic Therapy for Deep-Seated Tumors: From Concept to Biomedical Applications**. *Theranostics* 2020, **10**(3):1296-1318.

21. Liu T, Yang K, Liu Z: **Recent advances in functional nanomaterials for X-ray triggered cancer therapy**. *Progress in Natural Science: Materials International* 2020, **30**(5):567-576.

22. Chen H, Wang GD, Chuang YJ, Zhen Z, Chen X, Biddinger P, Hao Z, Liu F, Shen B, Pan Z *et al*: **Nanoscintillator-mediated X-ray inducible photodynamic therapy for in vivo cancer treatment**. *Nano Lett* 2015, **15**(4):2249-2256.

23. Chen H, Sun X, Wang GD, Nagata K, Hao Z, Wang A, Li Z, Xie J, Shen B: **LiGa5O8:Cr-based theranostic nanoparticles for imaging-guided X-ray induced photodynamic therapy of deep-seated tumors**. *Mater Horiz* 2017, **4**(6):1092-1101.

24. Ma L, Zou X, Bui B, Chen W, Song KH, Solberg T: **X-ray excited ZnS:Cu,Co afterglow nanoparticles for photodynamic activation**. *Applied Physics Letters* 2014, **105**(1).

25. Liu Y, Chen W, Wang S, Joly AG: **Investigation of water-soluble x-ray luminescence nanoparticles for photodynamic activation**. *Applied Physics Letters* 2008, **92**(4).

26. Shrestha S, Wu J, Sah B, Vanasse A, Cooper LN, Ma L, Li G, Zheng H, Chen W, Antosh MP: **X-ray induced photodynamic therapy with copper-cysteamine nanoparticles in mice tumors**. *Proc Natl Acad Sci U S A* 2019, **116**(34):16823-16828.

27. Wang H, Lv B, Tang Z, Zhang M, Ge W, Liu Y, He X, Zhao K, Zheng X, He M *et al*: **Scintillator-Based Nanohybrids with Sacrificial Electron Prodrug for Enhanced X-ray-Induced Photodynamic Therapy**. *Nano Lett* 2018, **18**(9):5768-5774.

28. Sun W, Shi T, Luo L, Chen X, Lv P, Lv Y, Zhuang Y, Zhu J, Liu G, Chen X *et al*: **Monodisperse and Uniform Mesoporous Silicate Nanosensitizers Achieve Low-Dose X-Ray-Induced Deep-Penetrating Photodynamic Therapy**. *Adv Mater* 2019, **31**(16):e1808024.

29. Lan G, Ni K, Xu R, Lu K, Lin Z, Chan C, Lin W: **Nanoscale Metal-Organic Layers for Deeply Penetrating X-ray-Induced Photodynamic Therapy**. *Angew Chem Int Ed Engl* 2017, **56**(40):12102-12106.

30. Ni K, Lan G, Veroneau SS, Duan X, Song Y, Lin W: **Nanoscale metal-organic frameworks for mitochondria-targeted radiotherapy-radiodynamic therapy**. *Nat Commun* 2018, **9**(1):4321.

31. Ni K, Lan G, Chan C, Duan X, Guo N, Veroneau SS, Weichselbaum RR, Lin W: **Ultrathin Metal-Organic-Layer Mediated Radiotherapy-Radiodynamic Therapy**. *Matter* 2019, **1**(5):1331-1353.

32. Lu K, He C, Guo N, Chan C, Ni K, Lan G, Tang H, Pelizzari C, Fu Y-X, Spiotto MT *et al*: **Low-dose X-ray radiotherapy–radiodynamic therapy via nanoscale metal–organic frameworks enhances checkpoint blockade immunotherapy**. *Nature Biomedical Engineering* 2018, **2**(8):600-610.

33. Kim MJ, Kim HJ, Park H, Tanida K, Kim S, Cheon JK, Lee KB: **Scintillation Properties of CsI:Na, Ba Crystal**. *IEEE Transactions on Nuclear Science* 2013, **60**(2):1049-1052.

34. Perotti C, Fukuda H, DiVenosa G, MacRobert AJ, Batlle A, Casas A: **Porphyrin synthesis from ALA derivatives for photodynamic therapy. In vitro and in vivo studies**. *Br J Cancer* 2004, **90**(8):1660-1665.

35. Koltai T: **Cancer: fundamentals behind pH targeting and the double-edged approach**. *Onco Targets Ther* 2016, **9**:6343-6360.

36. Otake M, Nishiwaki M, Kobayashi Y, Baba S, Kohno E, Kawasaki T, Fujise Y, Nakamura H: **Selective accumulation of ALA-induced PpIX and photodynamic effect in chemically induced hepatocellular carcinoma**. *Br J Cancer* 2003, **89**(4):730-736.

37. Hadjipanayis CG, Widhalm G, Stummer W: **What is the Surgical Benefit of Utilizing 5-Aminolevulinic Acid for Fluorescence-Guided Surgery of Malignant Gliomas?** *Neurosurgery* 2015, **77**(5):663-673.

38. Neumann LM, Beseoglu K, Slotty PJ, Senger B, Kamp MA, Hanggi D, Steiger HJ, Cornelius JF: **Efficacy of 5-aminolevulinic acid based photodynamic therapy in pituitary adenomas-experimental study on rat and human cell cultures**. *Photodiagnosis Photodyn Ther* 2016, **14**:77-83.

39. Mahmoudi K, Garvey KL, Bouras A, Cramer G, Stepp H, Jesu Raj JG, Bozec D, Busch TM, Hadjipanayis CG: **5-aminolevulinic acid photodynamic therapy for the treatment of high-grade gliomas**. *J Neurooncol* 2019, **141**(3):595-607.

40. Allison RR, Sibata CH: **Oncologic photodynamic therapy photosensitizers: a clinical review**. *Photodiagnosis Photodyn Ther* 2010, **7**(2):61-75.

41. Kessel D, Luguya R, Vicente MGH: **Localization and Photodynamic Efficacy of Two Cationic Porphyrins Varying in Charge Distribution¶**. *Photochemistry and Photobiology* 2003, **78**(5):431-435.

42. Kim J, Santos OA, Park J-H: **Selective photosensitizer delivery into plasma membrane for effective photodynamic therapy**. *Journal of Controlled Release* 2014, **191**:98-104.

43. Farzaneh A, Abdi MR, Saraee KRE, Mostajaboddavati M, Quaranta A: **Cesium-iodide-based nanocrystal for the detection of ionizing radiation**. *Optical Materials* 2016, **55**:22-26.

44. Kim JR, C.; Lee, Y.; Liu, J. P.; Sun, S.: **From Core/Shell Structured FePt/Fe3O4/MgO to Ferromagnetic FePt Nanoparticles**. *Chem Mater* 2008, **20**(23):7242-7245.

45. Leung YH, Ng AM, Xu X, Shen Z, Gethings LA, Wong MT, Chan CM, Guo MY, Ng YH, Djurisic AB *et al*: **Mechanisms of antibacterial activity of MgO: non-ROS mediated toxicity of MgO nanoparticles towards Escherichia coli**. *Small* 2014, **10**(6):1171-1183.

46. Krishnamoorthy K, Moon JY, Hyun HB, Cho SK, Kim S-J: **Mechanistic investigation on the toxicity of MgO nanoparticles toward cancer cells**. *Journal of Materials Chemistry* 2012, **22**(47):24610-24617.

47. Di DR, He ZZ, Sun ZQ, Liu J: **A new nano-cryosurgical modality for tumor treatment using biodegradable MgO nanoparticles**. *Nanomedicine* 2012, **8**(8):1233-1241.

48. Kumaran RS, Choi Y-K, Singh V, Song H-J, Song K-G, Kim KJ, Kim HJ: **In vitro cytotoxic evaluation of MgO nanoparticles and their effect on the expression of ROS genes**. *Int J Mol Sci* 2015, **16**(4):7551-7564.

49. Pugazhendhi A, Prabhu R, Muruganantham K, Shanmuganathan R, Natarajan S: **Anticancer, antimicrobial and photocatalytic activities of green synthesized magnesium oxide nanoparticles (MgONPs) using aqueous extract of Sargassum wightii**. *J Photochem Photobiol B* 2019, **190**:86-97.

50. A. H. Kayal YM, C. Jaccard, and I. Rossel: **Luminescence processes in CsI doped with Na+ and K+ ions**. *Solid State Commun* 1980, **35**(6):457-460.

51. Choi J, Kim G, Cho SB, Im H-J: **Radiosensitizing high-Z metal nanoparticles for enhanced radiotherapy of glioblastoma multiforme**. *Journal of Nanobiotechnology* 2020, **18**(1):122.

52. Bhatti JS, Bhatti GK, Reddy PH: **Mitochondrial dysfunction and oxidative stress in metabolic disorders — A step towards mitochondria based therapeutic strategies**. *Biochimica et Biophysica Acta (BBA) - Molecular Basis of Disease* 2017, **1863**(5):1066-1077.

53. Yoshioka E, Chelakkot VS, Licursi M, Rutihinda SG, Som J, Derwish L, King JJ, Pongnopparat T, Mearow K, Larijani M *et al*: **Enhancement of Cancer-Specific Protoporphyrin IX Fluorescence by Targeting Oncogenic Ras/MEK Pathway**. *Theranostics* 2018, **8**(8):2134-2146.

54. Zduniak K, Gdesz-Birula K, Wozniak M, Dus-Szachniewicz K, Ziolkowski P: **The Assessment of the Combined Treatment of 5-ALA Mediated Photodynamic Therapy and Thalidomide on 4T1 Breast Carcinoma and 2H11 Endothelial Cell Line**. *Molecules* 2020, **25**(21).

55. Alam MS, Getz M, Haldar K: **Chronic administration of an HDAC inhibitor treats both neurological and systemic Niemann-Pick type C disease in a mouse model**. *Science Translational Medicine* 2016, **8**(326):326ra323-326ra323.

56. Takahashi J, Misawa M, Murakami M, Mori T, Nomura K, Iwahashi H: **5-Aminolevulinic acid enhances cancer radiotherapy in a mouse tumor model**. *SpringerPlus* 2013, **2**(1):602.

57. Yamamoto J, Ogura SI, Shimajiri S, Nakano Y, Akiba D, Kitagawa T, Ueta K, Tanaka T, Nishizawa S: **5-Aminolevulinic acid-induced protoporphyrin IX with multi-dose ionizing irradiation enhances host antitumor response and strongly inhibits tumor growth in experimental glioma in vivo**. *Mol Med Rep* 2015, **11**(3):1813-1819.

58. Takahashi J, Murakami M, Mori T, Iwahashi H: **Verification of radiodynamic therapy by medical linear accelerator using a mouse melanoma tumor model**. *Scientific Reports* 2018, **8**(1):2728.

59. Gu X, Shen C, Li H, Goldys EM, Deng W: **X-ray induced photodynamic therapy (PDT) with a mitochondria-targeted liposome delivery system**. *J Nanobiotechnology* 2020, **18**(1):87.

60. Dinakaran D, Sengupta J, Pink D, Raturi A, Chen H, Usmani N, Kumar P, Lewis JD, Narain R, Moore RB: **PEG-PLGA nanospheres loaded with nanoscintillators and photosensitizers for radiation-activated photodynamic therapy**. *Acta Biomater* 2020, **117**:335-348.

61. Cree IA, Andreotti PE: **Measurement of cytotoxicity by ATP-based luminescence assay in primary cell cultures and cell lines**. *Toxicology in Vitro* 1997, **11**(5):553-556.

62. Imlay SMaJA: **Bacterial Porphyrin Extraction and Quantification by LC/MS/MS Analysis**. *Bio Protoc* 2015, **5**(19):e1616.

63. Setsukinai K, Urano Y, Kakinuma K, Majima HJ, Nagano T: **Development of novel fluorescence probes that can reliably detect reactive oxygen species and distinguish specific species**. *J Biol Chem* 2003, **278**(5):3170-3175.

64. Kim S, Fujitsuka M, Majima T: **Photochemistry of singlet oxygen sensor green**. *J Phys Chem B* 2013, **117**(45):13985-13992.

65. Yu Q, Sun J, Huang S, Chang H, Bai Q, Chen Y-X, Liang D: **Inward Budding and Endocytosis of Membranes Regulated by de Novo Designed Peptides**. *Langmuir* 2018, **34**(21):6183-6193.

66. Franken NAP, Rodermond HM, Stap J, Haveman J, van Bree C: **Clonogenic assay of cells in vitro**. *Nature Protocols* 2006, **1**(5):2315-2319.

CHAPTER 4:

1. Hu J, Tang Y, Elmenoufy AH, Xu H, Cheng Z, Yang X: **Nanocomposite-Based Photodynamic Therapy Strategies for Deep Tumor Treatment**. *Small* 2015, **11**(44):5860-5887.
2. Lucky SS, Soo KC, Zhang Y: **Nanoparticles in photodynamic therapy**. *Chem Rev* 2015, **115**(4):1990-2042.
3. Fan W, Huang P, Chen X: **Overcoming the Achilles' heel of photodynamic therapy**. *Chem Soc Rev* 2016, **45**(23):6488-6519.
4. Chen X, Song J, Chen X, Yang H: **X-ray-activated nanosystems for theranostic applications**. *Chem Soc Rev* 2019, **48**(11):3073-3101.
5. Belanova A, Chmykhalo V, Beseda D, Belousova M, Butova V, Soldatov A, Makarenko Y, Zolotukhin P: **A mini-review of X-ray photodynamic therapy (XPDT) nonoagent constituents' safety and relevant design considerations**. *Photochem Photobiol Sci* 2020, **19**(9):1134-1144.
6. Chen H, Sun X, Wang GD, Nagata K, Hao Z, Wang A, Li Z, Xie J, Shen B: **LiGa5O8:Cr-based theranostic nanoparticles for imaging-guided X-ray induced photodynamic therapy of deep-seated tumors**. *Mater Horiz* 2017, **4**(6):1092-1101.
7. Chen H, Wang GD, Chuang YJ, Zhen Z, Chen X, Biddinger P, Hao Z, Liu F, Shen B, Pan Z *et al*: **Nanoscintillator-mediated X-ray inducible photodynamic therapy for in vivo cancer treatment**. *Nano Lett* 2015, **15**(4):2249-2256.

8. Jiang F, Lee C, Zhang W, Jiang W, Cao Z, Chong HB, Yang W, Zhan S, Li J, Teng Y *et al*: **Radiodynamic therapy with CsI(na)@MgO nanoparticles and 5-aminolevulinic acid**. *J Nanobiotechnology* 2022, **20**(1):330.
9. Lee JY, Park JH, Kim SW: **Synthesis and evaluation of folate-immobilized198Au@SiO2nanocomposite materials for the diagnosis of folate-receptor-overexpressed tumor**. *Bulletin of the Korean Chemical Society* 2016, **37**(2):219-225.
10. Gomes-da-Silva LC, Zhao L, Bezu L, Zhou H, Sauvat A, Liu P, Durand S, Leduc M, Souquere S, Loos F *et al*: **Photodynamic therapy with redaporfin targets the endoplasmic reticulum and Golgi apparatus**. *EMBO J* 2018, **37**(13).
11. Kim S, Fujitsuka M, Majima T: **Photochemistry of singlet oxygen sensor green**. *J Phys Chem B* 2013, **117**(45):13985-13992.
12. Setsukinai K, Urano Y, Kakinuma K, Majima HJ, Nagano T: **Development of novel fluorescence probes that can reliably detect reactive oxygen species and distinguish specific species**. *J Biol Chem* 2003, **278**(5):3170-3175.
13. Imlay SMaJA: **Bacterial Porphyrin Extraction and Quantification by LC/MS/MS Analysis**. *Bio Protoc* 2015, **5**(19):e1616.
14. Yu Q, Sun J, Huang S, Chang H, Bai Q, Chen Y-X, Liang D: **Inward Budding and Endocytosis of Membranes Regulated by de Novo Designed Peptides**. *Langmuir* 2018, **34**(21):6183-6193.
15. Wu X, Zhu X, Chong P, Liu J, Andre LN, Ong KS, Brinson K, Jr., Mahdi AI, Li J, Fenno LE *et al*: **Sono-optogenetics facilitated by a circulation-delivered rechargeable light source for minimally invasive optogenetics**. *Proc Natl Acad Sci U S A* 2019.

APPENDICES

A supporting information for Chapter 3

Abbreviation list

ALT	Alanine Aminotransferase
ATP	Adenosine Triphosphate
BUN	Urea Nitrogen
CBC	Complete blood counts
DLS	Dynamic Light Scattering
DMEM	Dulbecco's Modified Eagle's Medium
EDS	Energy Dispersive Spectroscopy
ESI	Electrospray Ionization
FBS	*Fetal Bovine Serum*
ICP-MS	Inductively Coupled Plasma Mass Spectrometry
MRI	Magnetic Resonance Imaging
MTT	3-(4,5-Dimethylthiazolyl-2)-2,5-diphenyltetrazolium bromide
NPs	Nanoparticles
PBS	*Phosphate-Buffered Saline*
REF	*Radiation Enhancement Factor*
ROS	*Reactive Oxygen Species*

RPMI 1640	Roswell Park Memorial Institute Medium 1640
RT	Radiation
SEM	Scanning Electron Microscopy
SOD	Superoxide Dismutase
SOSG	Singlet Oxygen Sensor Green
STEM	Scanning Transmission Electron Microscopy
XPS	X-ray photoelectron spectroscopy

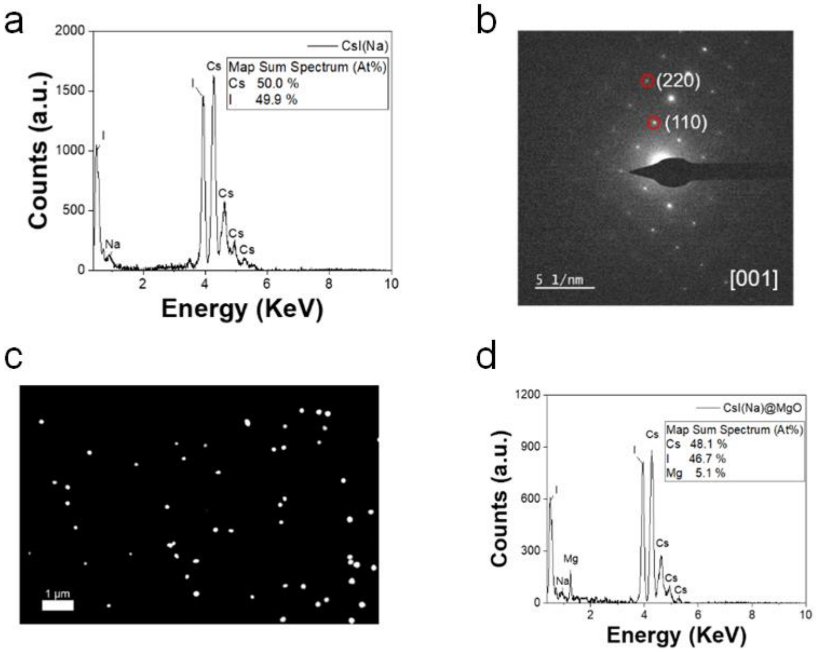

Figure S1. a) Elemental analysis of CsI(Na) nanoparticles by EDX. b) Selected area electron diffraction (SAED) of a single CsI(Na) nanoparticle under HRTEM. d) SEM image of CsI(Na)@MgO nanoparticles. Scale bars, 1 µm. e) EDX elemental analysis of CsI(Na)@MgO nanoparticles.

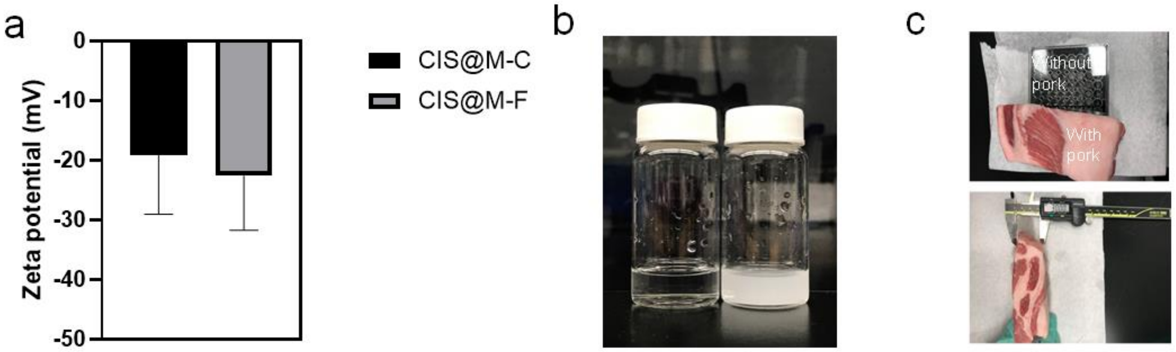

Figure S2. a) Z-potentials CIS@M-C and CIS@M-F nanoparticles, measured in D.I. water. b) Photos of CsI(Na) and CIS@M-F nanoparticles, taken after 24 hours of incubation in water. c) Setup of experiment to evaluate X-PDT activation. Solutions containing CIS@M-F, PpIX, and SOSG was irradiated with X-rays or LED light, with or without 3-cm pork placed between solutions and radiation sources. Experimental results are detailed in Figure 2d.

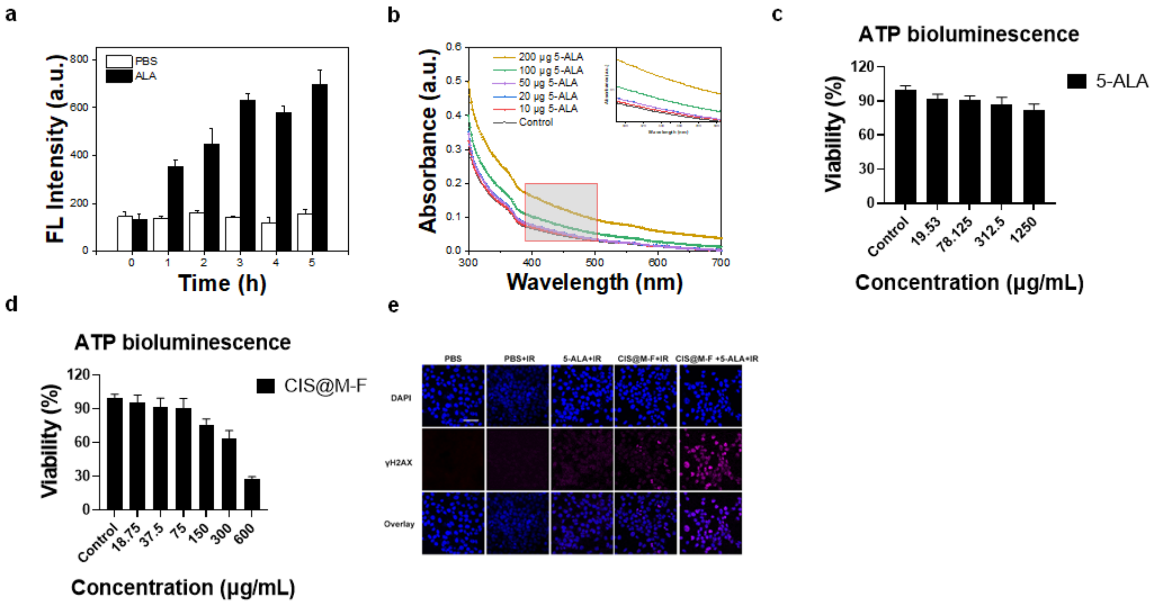

Figure S3. a) 5-ALA was converted to PpIX in cells, measured by measuring PpIX fluorescence. The signals were plateaued after ~ 3h. b) Characteristic PpIX absorbance was increased when cells were incubated with 5-ALA. The increase was 5-ALA-concentration dependent. c) Cell viability, measured with ATP bioluminescence assay at 24 h of incubation. 4T1 cells were incubated with 5-ALA up to 1250 µg/mL. d) Viability of 4T1 cells when incubated with CIS@M-F in the absence of ionizing radiation (IR), measured with ATP bioluminescence assay. e) Double-strand breaks, measured with rH2AX staining. 4T1 cells were treated with CIS@M-F+5-ALA+IR, CIS@M-F+IR, 5-ALA+IR, IR, and PBS. Positively stained foci per cells were quantified by ImageJ and the results were summarized in Figure 3g. Scale bar, 50 µm. Red, rH2AX; blue, DAPI.

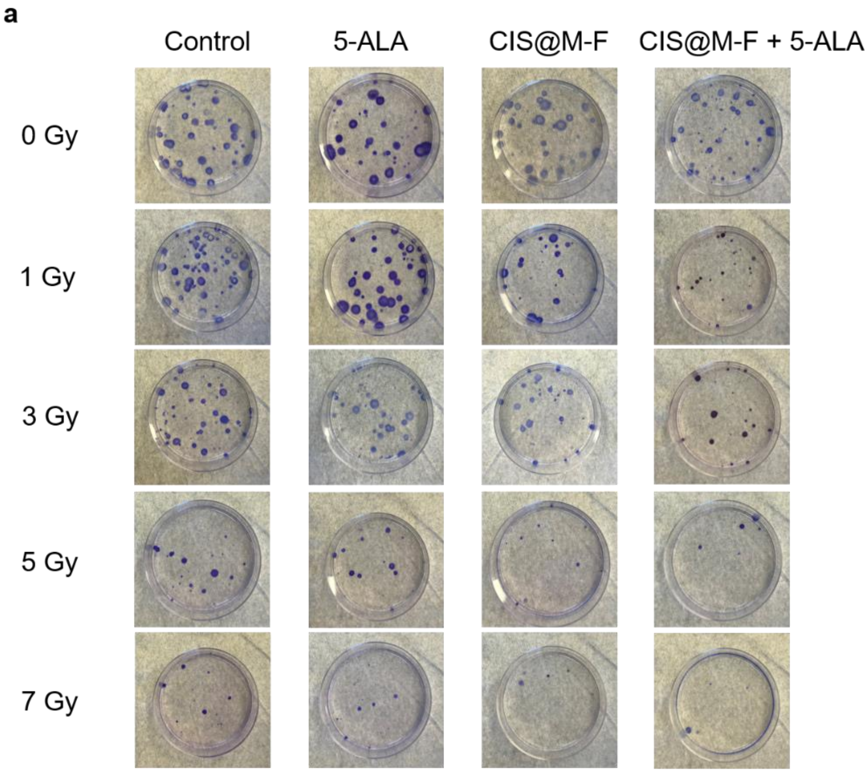

b

Summary of data fitting results

Group	*a*	*b*	*SF2*	*SF5*	D_{10}	DMR_{10}	*REF2*	*REF5*
PBS	0.128	0.0305	0.6852	0.2460	6.8402	/	/	/
5-ALA	0.1359	0.0311	0.6729	0.2329	6.6927	1.0220	1.0183	1.0562
CIS@M-F	0.1875	0.0504	0.5618	0.1111	5.1503	1.3281	1.2197	2.2142
CIS@M-F+ 5-ALA	0.1354	0.0858	0.5411	0.0595	4.4511	1.5367	1.2663	4.1345

Figure S4. a) Representative images of clonogenic assay results from different treatment groups. b) Summary of data fitting based on linear-quadratic equation. $S = \exp\text{-}(aD+bD^2)$, where S is the cell survival fraction, *D* is the radiation dose, and *a&b* are fitting coefficients. Radiation enhancement factors based on survival fraction relative to PBS (IR alone) at 2 Gy (REF2) and 5 Gy (REF5) as well as D_{10} (dose required to achieve 10% clonogenic survival) (DMF_{10}) were calculated and compared.

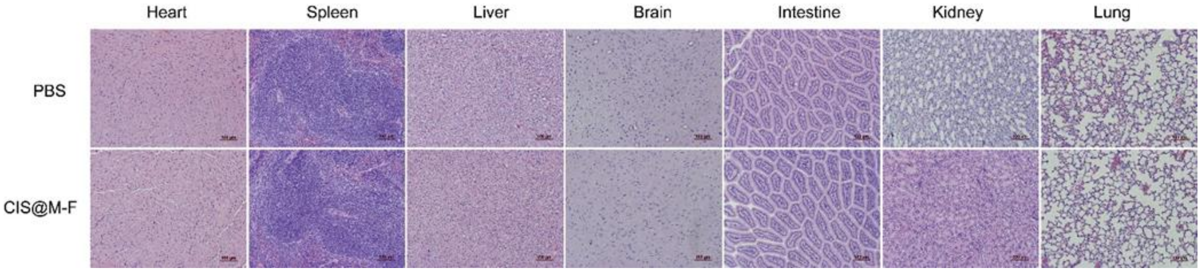

Figure S5. H&E staining of major organ tissues. Mice were i.v. injected with CIS@M-F (1.25 mg/kg) or carrier only (PBS) and euthanized after two weeks (n=5). Scale bars, 100 µm.